

Measurement of the charge ratio of cosmic-ray muons in Super-Kamiokande

素粒子物理学研究室 41502208 北川美西音

宇宙線ミュオンは、1次宇宙線と大気原子核の衝突反応の理解、中間子の生成比の見積もりおよび大気ニュートリノフラックスの理論計算の評価などにおいて重要な物理量となる。ミュオンは、1次宇宙線の組成の主成分を陽子が占めることから、 μ^+ がより多く生成されると考えられており、これまでの過去の実験から、300 GeV までのエネルギー範囲において電荷比の平均値は約 1.27 と得られている。一方で、TeV 以上の高エネルギー領域にかけては、1次宇宙線の組成と中間子成分の変化に応じて、電荷比は異なる振る舞いを取ることが予測されている。このため、地下深部にまで到達する高エネルギーミュオンの検出が可能な地下実験において、電荷比の精密測定が試みられている。

本研究では、スーパーカミオカンデ(SK)検出器を用いて 1.3 TeV のエネルギーをもつ宇宙線ミュオンについて電荷比の測定を行った。まず信号事象となる検出器内に静止したミュオンとその崩壊電子を適切に選別するための識別条件を検出器シミュレーションにより定めた。また、媒質中では μ^- が原子核による吸収を受けるため、見かけの平均寿命が μ^+ と比較して短くなる。そこで、 μ^\pm の水中での寿命の違いを利用して、 μ^\pm の計測数を見積もり、電荷比の算出を行った(図1)。本解析結果より、2008年から2018年にかけて取得されたSKの平均電荷比として、 $R(\mu^+/\mu^-) = 1.42 \pm 0.02$ (統計誤差)を得た(図2)。この結果は、300 GeV 以下の領域で測定された平均電荷比と比べて大きい。このことは、 π/K 中間子による寄与を仮定した理論予測において、TeV 領域におけるミュオン生成が π 中間子のみだけでなく、K 中間子からの崩壊にも依存していることを示している。

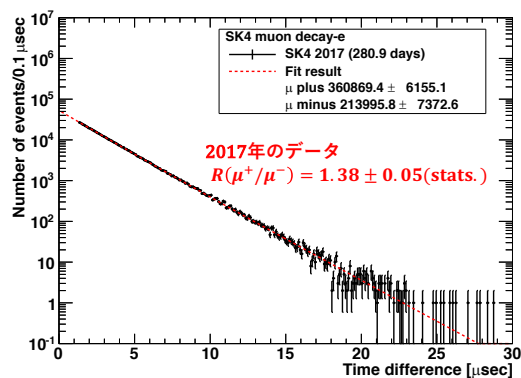


図1：SKで取得された $\mu-e$ 崩壊事象の時間情報 (2017年のデータ)

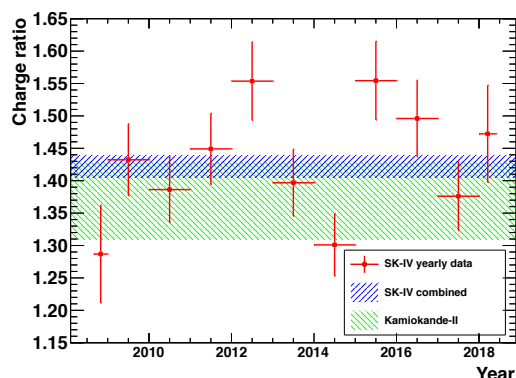


図2：2008年から2018年までに測定された電荷比。帯で示されている領域は平均値。

[業績一覧]

- ・日本物理学会(2回)：2021年3月15日(口頭発表)、2021年9月14日(口頭発表)
- ・新学術「ニュートリノで拓く素粒子と宇宙」研究会：2020年12月21日(ポスター発表)
- ・新学術「地下宇宙」研究会(2回)：2021年5月20日(ポスター発表)、2021年11月26日(口頭発表)
- ・International Cosmic Ray Conference 2021：2021年7月14日(ポスター発表)
- ・Proceedings of the 37th International Cosmic Ray Conference 2021 (出版)

Measurement of the charge ratio of cosmic-ray muons in Super-Kamiokande

Hussain Kitagawa

March 2022

Graduate School of Natural Science and Technology
(Master's Course)

Okayama University

Abstract

Cosmic-rays are the nuclei originating from outside the Earth, incident on the high altitude atmosphere. Since their discovery of cosmic-rays in 1910s, their characteristics have been studied from various aspects of astrophysics and particle physics: the original source and mechanism of their acceleration in the galaxy, components of the incoming cosmic-rays, and the relation between hadronic interaction and secondary productions in the atmosphere. Cosmic-rays can be classified into two categories: primary and secondary cosmic-rays. Secondary cosmic-rays are produced via the interactions of primary cosmic particles with air nuclei at the frontier of the atmosphere. The interaction products, pions, and kaons composing the showers of secondary cosmic-rays mostly decay into penetrating components, muons, and neutrinos which reaching under the Earth's surface. These observable particles carry the history of the cascade production of secondaries directly and enable probing the mechanism of secondary production. The muon charge ratio, defined as the ratio of the number of positive to negative charge atmospheric muons, is one of the important parameters to understand the hadronic interactions. It reflects the production ratio of charged pions and kaons and composition of cosmic primaries. Moreover, since neutrinos are produced in association with muons, the behavior of the muon charge ratio strongly relates to the energy distributions of atmospheric neutrinos. Thus, the muon charge ratio is necessary for the studies of secondary production and an improved calculation of the atmospheric neutrino fluxes. The muon charge ratio has been widely measured in several experiments on surface and underground in diverse energy ranges. In the previous measurements by CMS [1] and OPERA [2] below and above 1 TeV/c, respectively, the charge ratio was approximately constant at $R(\mu^+/\mu^-) \approx 1.27$ in the momentum range of 10 – 300 GeV/c and increased above this range [3], [4]. In this thesis, the measurement of the muon charge ratio with the minimum surface muon energy of 1.3 TeV in Super-Kamiokande detector is presented. Super-Kamiokande is a large water Cherenkov detector located in the Kamioka mine, Gifu Prefecture, Japan at a depth of 1,000 m (2,700 m of water equivalent (m.w.e.)). The muon charge increased from a TeV energy region and the precise measurement helped investigate the effect of kaon contribution.

At first, the production of cosmic-ray muons and the muon charge ratio are introduced in Chapter 1. Chapter 2 provides the fundamental information of Super-Kamiokande detector with its detection principle via Cherenkov radiation and data acquisition system. The method of event reconstruction for muons and decay electrons used in the analysis is explained in Chapter 3. Chapter 4 describes the simulation of muons and decay electrons including detector structure for a detailed understanding of the detector response and for the determination of the selection criteria. The evaluation and optimization of selection cuts for the control sample and the distribution of selected muon decay events are shown in Chapter 5. Chapter 6 reports the measurement of the charge ratio and the discussion of results. Finally the summary is provided in Chapter 7.

Keywords: Cosmic-ray muons; Muon decay; Charge ratio

Acknowledgement

I would first like to express my gratitude and appreciation for my research supervisor Koshio-san for his enormous support. He allowed me to join the Super-Kamiokande group and made my research life a wonderful time. He actively provided me the opportunity to join the meetings on-site and connected me with other researchers to proceed with my research project smoothly. Without his precious support, it was impossible to conduct my research. Further, I would like to acknowledge my co-supervisor, Nakano-san from B4, for his valuable guidance throughout my research. He provided me with the methods and tips to lead me in the right direction. His suggestions and feedback brought my thoughts to a higher level. I would also like to appreciate inviting me to the restaurant after the conference. In addition, I would like to appreciate the support from the members of Kobe University. During my stay at Kobe, I was given a valuable opinion about the simulation from Kurashige-san as a developer. He taught me the details of the simulation tools and the surrounding physics for my further understanding. I would also like to express my gratitude to an OB of the particle group at Kobe University, Shiozawa-san. My research base consists of his tremendous works, and without this support, the research has never been accomplished. I would also thank all the members of Kobe university who helped with my research. Moreover, I would like to thank the laboratory members. The discussions with Hino-san of specially appointed researcher, Harada-san of D2, Sakai-san of D1, and conversation with Nakanishi-san of M1, Tano-kun of B4, Tada-kun of B4, Shiraishi-kun of B4, and supports from Yamamoto-san of a secretary were very helpful and made my research life fulfilling. Finally, I would like to thank my family for their kind support.

Table of Contents

Abstract	i
Acknowledgment	ii
Table of Contents	iii
List of Figures	v
List of Tables	viii
1 Introduction	1
1.1 Cosmic-ray muons	1
1.2 Primary and secondary cosmic-rays	1
1.2.1 Primary interaction in the atmosphere	2
1.2.2 Production of secondary particles	3
1.2.3 Production of atmospheric muons	4
1.3 Muon spectrum	5
1.4 Muon charge ratio	6
1.5 Fraction of atmospheric neutrinos	8
1.6 Previous cosmic-ray muon charge ratio measurements	9
2 Super-Kamiokande detector	12
2.1 Overview of Super-Kamiokande detector	12
2.2 Detector structure	13
2.2.1 Inner detector and outer detector	13
2.2.2 20-inch Photo Multiplier Tube (PMT)	13
2.2.3 Helmholtz coils	18
2.3 Detection principle	19
2.4 Water and air circulation system	20
2.4.1 Water purification system	20
2.4.2 Air purification system	22
2.5 Data acquisition system in SK-IV	23
2.5.1 QBEE	23
2.5.2 Software trigger	24
3 Event reconstruction	26
3.1 Reconstruction of muon	26
3.1.1 Cleaning cuts	26
3.1.2 Entry point	27

3.1.3	Direction reconstruction	27
3.1.4	Event classification	29
3.2	Reconstruction of decay electron	31
3.2.1	Vertex reconstruction	31
3.2.2	Direction reconstruction	32
3.2.3	Energy reconstruction	33
4	Muon and decay electron simulation	37
4.1	SK detector simulation	37
4.2	Muon simulation	37
4.2.1	Generating muons	38
4.3	Decay electron simulation	39
5	Event selection	45
5.1	Data set of control samples	45
5.2	Selection criteria	46
5.2.1	Selection for stopping muon	47
5.2.2	Selection for decay electron	48
5.3	Selected samples	51
5.3.1	Stopping muon candidates	51
5.3.2	Decay electron candidates	55
6	Results and discussion	62
6.1	Calculation of charge ratio	62
6.2	Results	64
6.3	Discussion	64
7	Summary	69

List of Figures

1.1	Overview of cosmic-ray production.	2
1.2	Energy spectrum of cosmic-rays. The equivalent lab energies of particle accelerator experiments are indicated on the energy axis [5].	3
1.3	Comparison between the calculation of high muon energy flux and the measured data. In the high energy region ($E_\mu \gg \epsilon \simeq 1$ GeV), the effects of decay and energy loss are negligible ($E_\mu \approx E_{\text{org}}$). However, muon energy loss and decay become important below 200 GeV [5].	7
1.4	Fraction of atmospheric muons and muon neutrinos from pions and kaons decay. Solid lines represent for vertical and dashed lines for the zenith angle 60° [5].	9
1.5	The previous measurements of the muon charge ratio as a function of the vertical muon momentum with a fit of πK model (see Chapter 6) [1].	10
2.1	Schematic view of the SK detector [11].	12
2.2	Schematic view of the PMT support structure [11].	14
2.3	Topology of the muon decay event and neutrino event in SK tank.	15
2.4	Construction of a PMT (The PMT shown above is the type of Head-on) [14].	15
2.5	20-inch ID PMT [11].	16
2.6	Quantum efficiency of the ID PMT as a function of wavelength [11].	17
2.7	Distribution of 1 p.e. pulse height of ID PMT with 410 nm wavelength light [11].	17
2.8	Distribution of relative transit time of ID PMT with 410 nm wavelength light [11].	18
2.9	Schematic view of acrylic and a FRP cases [15].	18
2.10	Schematic view of Helmholtz coils surrounding the SK tank [15].	19
2.11	Formation of Cherenkov radiation.	19
2.12	Schematic view of the water purification system [15].	22
2.13	Schematic view of the air circulation system [11].	23
2.14	Block diagram of the QTC and its peripheral devices [19].	23
2.15	Timing chart for the QTC operation. The gradation of color indicates the integrated charge of PMT signals [19].	24
3.1	Four types of cosmic-ray muon events observed at the SK detector.	27
3.2	Distribution of two parameters, GOF and F_{cone} used in Muboy in assessing quality of the fit.	30
3.3	The histogram of dE/dX distribution for the track length determination of Stopping muons [21]. The stopping point is determined at 25 m.	31
3.4	Probability density function of the residual time $t_{\text{res},i}$ obtained from LINAC calibration. The peaks around 40 nsec and 110 nsec are the PMT late-pulses [23].	32
3.5	Vertex resolution as a function of true electron kinetic energy in SK-IV [23].	33
3.6	Energy dependence of the angular likelihood function used in direction reconstruction [15].	34

3.7	The θ_i and ϕ_i coordinates for the i -th hit PMT [15].	36
3.8	The distribution of photo-cathode coverage function $S(\theta, \phi)$: for PMTs on the barrel of the tank (left) and for PMTs on top and bottom of the tank (right) [24].	36
4.1	Mountain Ikenoyama topographical map in 50 m grid. The color represents the magnitude of the altitude and the black point is the location of SK detector [29].	38
4.2	Schematic of vertical cylindrical detector of SK with coordinate system. θ is defined to be the zenith angle and ϕ is the azimuthal angle. The slant depth χ denotes the traverse distance by muon in the rock between entering position of the mountain at the specific altitude (m) to the center position of the detector located at the certain depth underground, 330 m from sea level [30].	39
4.3	Cosmic muon energy spectrum at three underground experiment site [26]. The average muon energy at SK is $E_\mu = 271 \pm 2$ GeV. Muon energy spectrum for $E_\mu \leq 20$ GeV is almost flat.	40
4.4	Muon flux as a function of zenith and azimuthal angle at SK depth and location calculated with MUSIC.	41
4.5	Energy distribution of injected muons (left) and its survival probability defined as the ratio of injected muons to stopping muons per 0.5 GeV bin (right). The minimum muon energy is set at least 0.1 GeV at the generated point of frame of ID to travel inward the ID tank.	41
4.6	Generated muon energy and the Z coordinate of its reconstructed decay electrons in MC.	42
4.7	Zenith angle distribution of generated muons in MC calculated from [31]. The angular integration covers the entire hemisphere. Blue line and red line represent injected and reconstructed muons, respectively.	42
4.8	The true decay curve of stopped muons observed in MC. The fitting range is red solid line and the expected distribution after fitting the function is red dashed line.	43
4.9	The kinetic energy distribution of decay electrons from positive stopping muons in MC. The true energy distribution is red solid line and reconstructed energy distribution is black solid line. Events are required to be positioned more than 200 cm away from the ID wall in the SK detector (Fiducial volume cut).	43
4.10	Vertex distribution of reconstructed decay electrons in MC. Here, the fiducial volume cut is applied.	44
5.1	Typical ring pattern of a stopping muon in the SK detector (ID and OD). The gradation of the color in each point represents the amount of charge observed in a PMT.	46
5.2	Typical ring pattern of a decay electron in the SK detector (ID). The gradation of the color in each point represents the amount of charge observed in a PMT.	46
5.3	The flow chart of μ -e decay event selection for SK-IV data analysis.	47
5.4	Total charge of stopping muons in the control sample.	48
5.5	Zenith angle distribution of stopping muons in the control sample. θ is defined as the zenith angle, where $\cos \theta = +1$ correspond to vertically downward direction and $\cos \theta = -1$ to vertically upward direction. Almost all stopping muons are coming from the top side of the SK tank toward the bottom.	49
5.6	Vertex distribution of reconstructed decay electrons in the data. Muon reduction cuts, fiducial volume cut, and time difference cut for decay electrons are applied.	51

5.7	Distributions of the quality of fitting parameters used for decay electrons in the data (black line) and MC (red line). Muon reduction cuts, fiducial volume cut, and time difference cut are applied.	52
5.8	Distributions of reconstructed energy (left) and N_{50} (right) of decay electrons in the data (black line) and MC (red line). Muon reduction cuts, fiducial volume cut, and time difference cut are applied.	53
5.9	Distribution of distance between reconstructed stopped position of stopping muon and vertex of decay electrons in data (black line) and MC (red line). Muon and decay electron reduction cuts are applied.	53
5.10	The fraction of muon events per 10 cm distance bin to the total events (left) and its detecting efficiency (right) as function of distance in MC. The reduction cuts described in above for both muons and decay electrons are applied.	54
5.11	Schematic view of the prompt signal and delayed signal in the time window.	54
5.12	Distribution of decay electron energy and muon lifetime in the data after applying fiducial volume cut.	55
5.13	Enter position of stopping muon in the SK tank for X-Y (left) and R-Z (right) coordinates in the data.	56
5.14	Intensity of stopping muons arriving at SK detector as a function of azimuthal and zenith angle in the data. $\phi = 0^\circ$ and $\phi = 90^\circ$ corresponds to east and north, respectively.	57
5.15	Azimuthal and zenith angle distribution of stopping muons in the data.	57
5.16	Distribution of Muboy goodness for stopping muon in the data (black line) and MC (red line). Almost all muon events are distributed around 0.6.	58
5.17	Distribution of track length for stopping muons in the data.	58
5.18	The relationship between track length and total deposit charge (left) and the distribution of total charge divided by track length (right) for stopping muons in the data. The constant of proportionality is approximately 25 p.e per unit cm.	59
5.19	Vertex distribution of selected reconstructed decay electrons in the data.	60
5.20	The decay curve of stopped muons observed in sample data. The fitting range is red solid line and the expected distribution after fitting the function is red dashed line.	61
6.1	Schematic of the muonic atom. A negative muon takes an atomic orbit (K shell) and creates an excited nucleus. The negative muon follows either process, free muon decay in orbit of nuclear muon capture.	62
6.2	The decay curve of stopped muons observed each year from 2008 to 2018. The solid red line was obtained by fitting a function Eq. (6.5). The effective live time and fitting results (number of positive and negative muons with the charge ratio, $\chi^2/d.o.f$) are listed in the legend.	66
6.3	Fitting results of decay curve with χ^2 (red) probability, $d.o.f$ (green), $(\chi^2/d.o.f) \times 100$ (blue) (left) and the event rate of decay electron [event/day] (right) obtained from positive (red) and negative (blue) stopped muons in SK-IV period.	67
6.4	Yearly time variation of the charge ratio of 1.3 TeV cosmic-ray muons from 2008 to 2018 together with the result from the Kamiokande-II. The blue band area shows the average of muon charge ratio in SK-IV period and green band is the result from Kamiokande-II [10].	68

List of Tables

2.1	Experimental phases of SK. The live times are the duration of the observation after removing bad/calibration runs.	13
2.2	The property of 20-inch PMT.	16
2.3	Energy threshold of Cherenkov radiation for various particles in pure water. . .	20
2.4	Summary of trigger threshold of hit PMTs within a 200 nsec window (N_{200}) in SK-IV and its time width.	25
3.1	Number of hit PMTs (N_{hit}) and the corresponding limit on the PMT charge of all selected ID PMTs in Muboy fit.	28
3.2	Lower limits on the number of nearest neighbors (N_{near}) corresponding to the number of PMTs selected after the first cleaning cut.	28
6.1	The results of N_+ , N_- and the charge ratio $R(\mu^+/\mu^-)$. In this study, only statistical uncertainty is considered.	67

Chapter 1

Introduction

1.1 Cosmic-ray muons

Cosmic-rays are relativistic high-energy particles entering the Earth's atmosphere, with some reaching the Earth's surface. Cosmic-rays can be divided into primary cosmic-ray and secondary cosmic-ray. Primary cosmic-rays have an energy region expanding from a few MeV to 10^{20} eV, composed of various ionized nuclei, such as protons (90%) and alpha particles (9%). Primary cosmic-rays produce several particles through various reactions between atmospheric nuclei while propagating the atmosphere. The particles generated in this process are called secondary cosmic-rays. These are mostly produced via hadron interactions generating hadrons, such as pions and kaons in most cases. Conversely, some secondary particles decay into cosmic-ray muons and neutrinos. The overview of cosmic-ray production can be seen in Figure 1.1. Regarding the production of muons, kaons, and pions decay into as described into the following process:

$$\begin{aligned}\pi^\pm &\rightarrow \mu^\pm + \nu_\mu(\bar{\nu}_\mu) \quad (\sim 100\%), \\ K^\pm &\rightarrow \mu^\pm + \nu_\mu(\bar{\nu}_\mu) \quad (\sim 63.5\%).\end{aligned}\tag{1.1}$$

Here, parent pions and kaons mostly decay as following process via the weak interaction:

$$\mu^\pm \rightarrow e^\pm + \nu_e(\bar{\nu}_e) + \bar{\nu}_\mu(\nu_\mu).\tag{1.2}$$

However, cosmic-ray muons are less likely to interact with matter, and their relativistic effects extend their lifetime, allowing them to reach deep underground. In the Earth's atmosphere, the muon decay length becomes larger than its typical production height (~ 15 km) above $E_\mu \sim 2.5$ GeV.

1.2 Primary and secondary cosmic-rays

The primary cosmic-rays have been measured in several experiments over the energy range from a few GeV to above 10^{20} eV. The differential energy spectrum of the cosmic-ray can be expressed as:

$$\frac{dN}{dE} \propto N_0 E^{-\alpha} \quad [1/\text{m}^2 \text{ s sr GeV}],\tag{1.3}$$

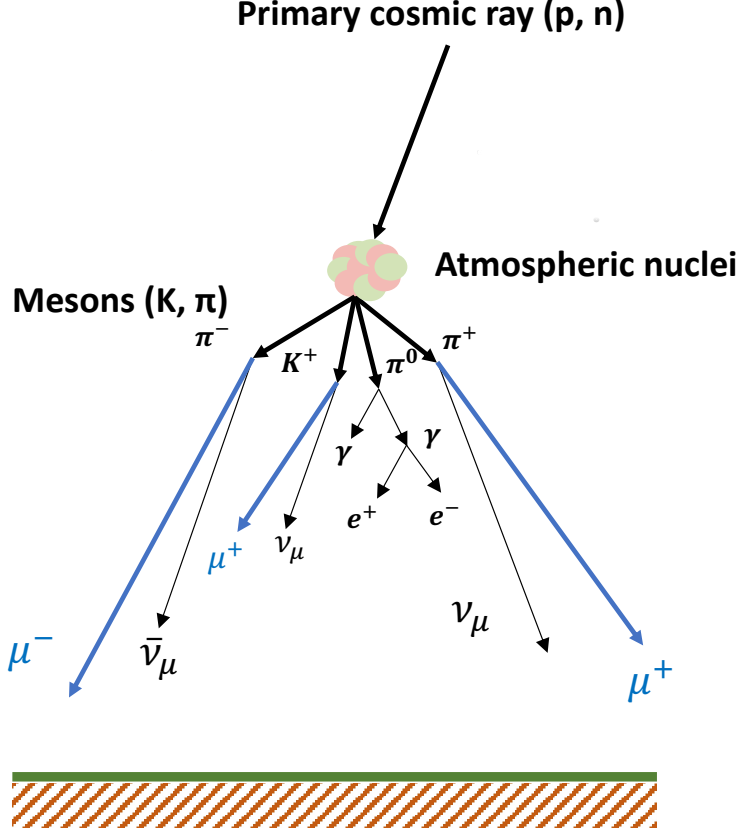


Figure 1.1: Overview of cosmic-ray production.

where N is the number of nucleons, N_0 is the constant, E is total energy of nucleon, α is the differential spectral index set as $\alpha \equiv \gamma + 1$, and γ is the integral spectral index. Figure 1.2 shows the energy spectrum of primary cosmic-ray of various particles obtained by both the direct measurements above the atmosphere and indirect measurements from the air shower experiments. Here, the parameter α changes according to the energy between 10 GeV and 10^{15} eV and set as 2.7. The determination of spectral index γ is significant in examining the components of cosmic primaries, and further understanding the interaction mechanism of high energy particles in the atmosphere.

1.2.1 Primary interaction in the atmosphere

The diffusion equation of particles in the atmosphere is developed to demonstrate the air shower production depending on the type of particles. The diffusion equation of the primary particles (nucleon) in the atmosphere can be described as follows:

$$\frac{dN_N(E, X)}{dX} = -\frac{N_N(E, X)}{\lambda_N(E)} + \int_E^\infty F_{NN}(E, E') \frac{N_N(E', X)}{\lambda_N(E')} \frac{dE'}{E}, \quad (1.4)$$

where $N_N(E, X)dE$ is the number of nucleons at a slant depth X in the atmosphere with the energy range, $E \sim E + dE$, $\lambda_N(E)$ is the mean free path of nucleons in atmosphere, and $F_{NN}(E, E')$ is the cross section for nucleon-nucleon interaction between an incident nucleon of energy E' and outgoing nucleon of energy E . Here, $F_{NN}(E, E')$ is defined as:

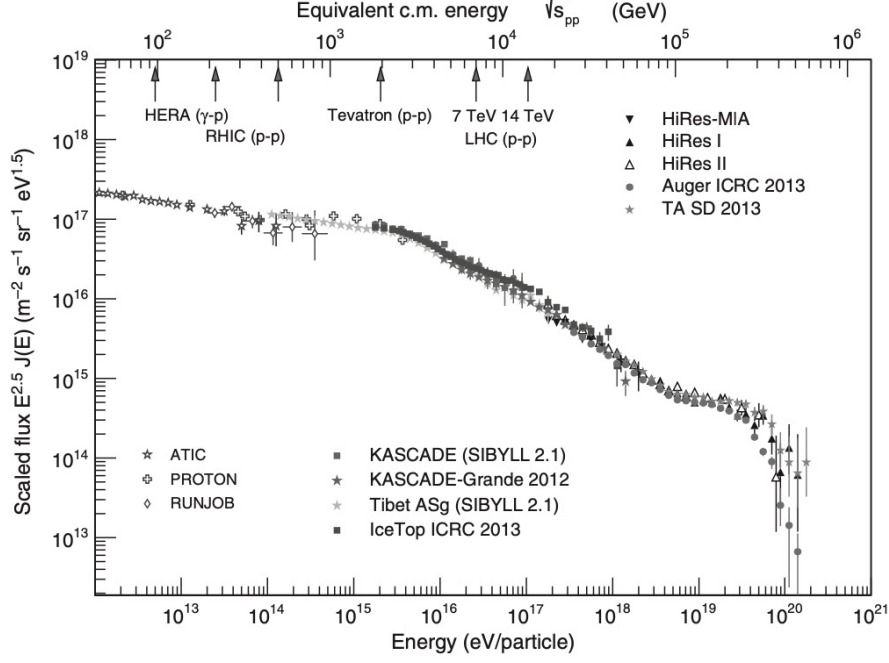


Figure 1.2: Energy spectrum of cosmic-rays. The equivalent lab energies of particle accelerator experiments are indicated on the energy axis [5].

$$F_{NN}(E, E') = \frac{E}{\sigma_{NN}^{\text{inel}}(E')} \frac{d\sigma_{NN}(E, E')}{dE}, \quad (1.5)$$

where $\sigma_{NN}^{\text{inel}}$ is the total inelastic nucleon-nucleon cross section, $d\sigma_{NN}(E, E')$ is the cross section for a nucleon of energy E' to produce a nucleon with energy E in nucleon-nucleon interaction. The solution of Eq. (1.4) is obtained by applying Eq. (1.3) as the boundary condition. For nucleons, the solution is given as:

$$N(E, X) = C \exp(-X/\Lambda) E^{-\gamma+1}, \quad (1.6)$$

where C is a constant, and Λ is the attenuation length (g/cm^2) of nucleon.

1.2.2 Production of secondary particles

The cascade of various hadrons can be expressed as the set of coupled diffusions in principle. Analytic solutions for the diffusion equations provide the detail and specific information of particle flux and energies of secondary particles.

Considering only pions and kaons as the secondary particles, the diffusion equation of pions can be expressed as the sum of two components, π^+ and π^- as follows:

$$\begin{aligned} \frac{dN_\pi(E, X)}{dX} = & - \left(\frac{1}{\lambda_\pi} + \frac{1}{d_\pi} \right) N_\pi(E, X) + \int_0^1 \frac{N_\pi(E/x_L, X) F_{\pi\pi}(E_\pi, E_\pi/x_L) dx_L}{\lambda_\pi(E/x_L) x_L^2} \\ & + \int_0^1 \frac{N_N(E/x_L, X) F_{N\pi}(E_\pi, E_\pi/x_L) dx_L}{\lambda_N(E/x_L) x_L^2} \end{aligned} \quad (1.7)$$

where x_L is E/E' , λ_π is the interaction length of pions in air, and d_π is the decay mean free path of pions defined as:

$$\frac{1}{d_\pi} = \frac{m_\pi c^2 h_0}{Ec\tau_\pi X \cos\theta} \equiv \frac{\epsilon_\pi}{EX \cos\theta}. \quad (1.8)$$

Here, m_π and τ_π is the mass and lifetime of a pion, respectively, h_0 is the scale height (≈ 6.5 km), and c is the speed of light. The first term of Eq. (1.7) represents the decrease in pions via interaction and decay in the atmosphere, the second term represents the regeneration of pions and the third term indicates the production of pions via nucleon-nucleon interaction.

For $E \gg \epsilon_\pi$, the contribution of Eq. (1.8) can be neglected. Then, the solution of Eq. (1.7) is obtained by applying the boundary condition $N_\pi(E, 0) = 0$ as follows:

$$N_\pi(E, X) = N_N(E, 0) \frac{Z_{N\pi}}{1 - Z_{NN}} \frac{\Lambda_\pi}{\Lambda_\pi - \Lambda_N} (\exp(-X/\Lambda_\pi) - \exp(-X/\Lambda_N)) \quad (1.9)$$

where, the attenuation lengths is given as:

$$\Lambda_\pi \equiv \frac{\lambda_\pi}{1 - Z_{\pi\pi}}, \quad (1.10)$$

$$\Lambda_N \equiv \frac{\lambda_N}{1 - Z_{NN}}.$$

The pion flux in Eq. (1.9) reaches the maximum at $X \sim 140$ g/cm² (~ 15 km) and then, decreases according to the attenuation length [5]. Here, Z_{NN} is the spectrum-weighted moment for a nucleon to produce another nucleon defined as:

$$Z_{NN} \equiv \int_0^1 (x_L)^{\gamma-1} F_{NN}(x_L) dx_L. \quad (1.11)$$

For $\gamma = 1$, Z -moment represents the average ratio of the energy between the incident and outgoing particles in a nucleon-nucleon interaction. Due to the steep primary cosmic-ray spectrum, for $\gamma > 1$, the contribution of x_L to the Z -moment becomes small ($x_L \rightarrow 0$). However, if x_L is large enough, the outgoing particle carries the most energy of incident particle. In this case, the fluxes only depend on the particles generated in the forward region of the interaction frame.

1.2.3 Production of atmospheric muons

Muons are produced in the atmosphere at a high altitude and carry the original information of early shower production. A relatively long time of 2.2 μ sec and a small cross section of the medium render muons detectable at the Earth's surface. Muons are produced by the decay of unstable secondary particles, including pions and kaons, and charmed particles. The main decay processes producing muons are shown in Eq. (1.1). In addition to the decay modes of Eq. (1.1), high energy muons can be produced by the decay of charmed mesons (D^\pm, D^0). Here, for unstable particles, the two major processes, namely nuclear interactions, and decay processes, become competing while propagating through the atmosphere. These processes rely on the particle lifetime and the cross section of the atmosphere depending on its density. Charmed particles have a small production cross section in the nucleon-nucleon interaction, which becomes important in over 10 TeV energy region due to the relatively short lifetime of charmed mesons and hadrons. Hence, as the secondary particles, pions and kaons can mainly

be considered as the primary particles to produce muons. The energy limit of the muon and neutrino from two-body decay in the lab frame is given as:

$$\begin{aligned} E \frac{m_\mu^2}{M^2} &\leq E_\mu \leq E, & (\text{muons}) \\ 0 \leq E_\nu &\leq E \left(1 - \frac{m_\mu^2}{M^2}\right), & (\text{neutrinos}) \end{aligned} \quad (1.12)$$

where M is the mass of a parent meson, and E is the energy of a decaying meson in the lab frame. For the numerical calculation of the $\pi^\pm \rightarrow \mu^\pm + \nu_\mu(\bar{\nu}_\mu)$ decay process, comparing the masses between the parent pions and muons, the latter has a sufficiently large mass, carrying most energy. Therefore, the energy fraction of decay products to the pion are given, as $\langle E_\mu \rangle / E_\pi = 0.79$ and $\langle E_\nu \rangle / E_\pi = 0.21$, respectively, indicating that the contribution of pions to neutrino is constrained to that of muons. However, the corresponding kaon decay, numbers are given as $\langle E_\mu \rangle / E_K = 0.52$ and $\langle E_\nu \rangle / E_K = 0.48$, respectively. Since the mass of kaon is much larger than that of muon, the contribution of kaons to neutrinos becomes significant in the high energy region (TeV and above) and further understanding of kaon production becomes important for the precise calculation of atmospheric neutrino fluxes.

Here, the muon production spectrum from the parent meson i (pions or kaons) is given as follows:

$$\mathcal{P}_\mu(E, X) = \sum_i \int_{E_{min}}^{E_{max}} \frac{dN_i(E, E')}{dE} \mathcal{D}_i(E', X) dE', \quad (1.13)$$

where $dN_i(E, E')/dE$ is the muon spectrum produced by particles i with energy E' , E_{min} , and E_{max} are the minimum and maximum energies of parent mesons producing muons, $\mathcal{D}_i(E', X)$ is the spectrum of the parent mesons with energy E' at the slant depth X . Assuming the parent mesons are pions, the function \mathcal{D}_π is given as follows:

$$\mathcal{D}_\pi(E, X) = \frac{\epsilon_\pi}{EX \cos \theta} \Pi(E, X). \quad (1.14)$$

The production spectrum of muons from both components, pions and kaons, is obtained by taking two forms of Eq. (1.13) as follows:

$$\begin{aligned} \mathcal{P}_\mu(E, X) &= \frac{\epsilon_\pi}{X \cos \theta (1 - r_\pi)} \int_{E_\mu}^{E_\mu/r_\pi} \frac{N_\pi(E, X) dE}{E} \frac{dE}{E} \\ &+ \frac{0.635\epsilon_K}{X \cos \theta (1 - r_K)} \int_{E_\mu}^{E_\mu/r_K} \frac{N_K(E, X) dE}{E} \frac{dE}{E}. \end{aligned} \quad (1.15)$$

where $r_{\pi, K} \equiv m_\mu^2/M_{\pi, K}^2$, and $M_{\pi, K}$ is the mass of either parent meson, pions or kaons.

1.3 Muon spectrum

The muon energy spectrum at the slant depth X_0 is obtained by calculating the effects of energy loss and decay while propagating in the atmosphere. According to Eq. (1.8), the decay rate of muons is given as:

$$\frac{dN_\mu}{dX} = \frac{\epsilon_\mu}{EX \cos \theta} N_\mu(E, X), \quad (1.16)$$

where X is the slant depth along the travel direction of the muon with energy E , and θ is the zenith angle. The muon energy loss in the atmosphere is given as $dE/dX = \alpha_{\text{atm}} \approx -2 \text{ MeV/g/cm}^2$. Hence, the muon energy E_μ at the vertical atmospheric depth X_0 can be expressed as:

$$E_\mu = E_{\text{org}} - \alpha_{\text{atm}}(X_0/\cos \theta - X), \quad (1.17)$$

where E_{org} is the muon energy at the slant depth X . The survival probability P of muon with energy E_μ and zenith angle θ at the observation level X_0 from the original location at the slant depth X is calculated by integrating Eq. (1.16) as follows:

$$P(E_\mu, \theta, X, X_0) = \left[\frac{X \cos \theta}{X_0} \frac{E_\mu}{E_\mu + \alpha_{\text{atm}}(X_0/\cos \theta - X)} \right]^{\epsilon_\mu/(E_\mu \cos \theta + \alpha_{\text{atm}} X_0)} \quad (1.18)$$

Muon intensity at the observation depth in the energy region for $E_\mu < \epsilon_\pi$, is given as:

$$I_\mu(E_\mu) = \int_0^{X_0/\cos \theta} \mathcal{P}_\mu(E_{\text{org}}, X) \times P(E_\mu, \theta, X, X_0) dX. \quad (1.19)$$

Numerical approximation values for the muon energy spectrum is provided as:

$$\frac{dN_\mu}{dE_\mu} \approx \frac{0.14 E_\mu^{-2.7}}{\text{cm}^2 \text{ sec sr GeV}} \left\{ \frac{1}{1 + \frac{1.11 E_\mu}{\epsilon_\pi(\theta)}} + \frac{0.054}{1 + \frac{1.11 E_\mu}{\epsilon_K(\theta)}} \right\}, \quad (1.20)$$

where $\epsilon_\pi(\theta) = 115 \text{ GeV}/\cos \theta$, and $\epsilon_K(\theta) = 850 \text{ GeV}/\cos \theta$. Here, the contribution from charm particle and heavier particles are not considered though their contributions are significantly high in the very high energy region. The measured muon energy flux at the sea level together with the approximation of high energy muon flux from the calculations are shown in Figure 1.3.

1.4 Muon charge ratio

The muon charge ratio is the ratio of the positive to negative charge atmospheric muons. The measurement of muon charge ratio can provide a detailed information on the high energy hadronic interaction in the atmosphere and components of cosmic primaries. The muon charge directly reflects mechanisms of the production of multiple hadrons, such pions and kaons in the atmosphere and contribute to the determination of spectral index γ in the high energy region. However, since the data regarding the production of multiple hadrons in the accelerator are limited to the high energy region, the theoretical understanding of the hadronic interaction is still insufficient. For these reasons, the muon charge ratio at sea level has been studied and the measurements have been performed in wide energy ranges. For the theoretical understanding of the muon charge ratio, a simplified model assuming the primary spectrum only consisting of protons is considered [6]. In the model, the pion production wherein all particles decaying into muons is considered (except kaon). Further illustration of the production of secondary particles is further discussed in [6].

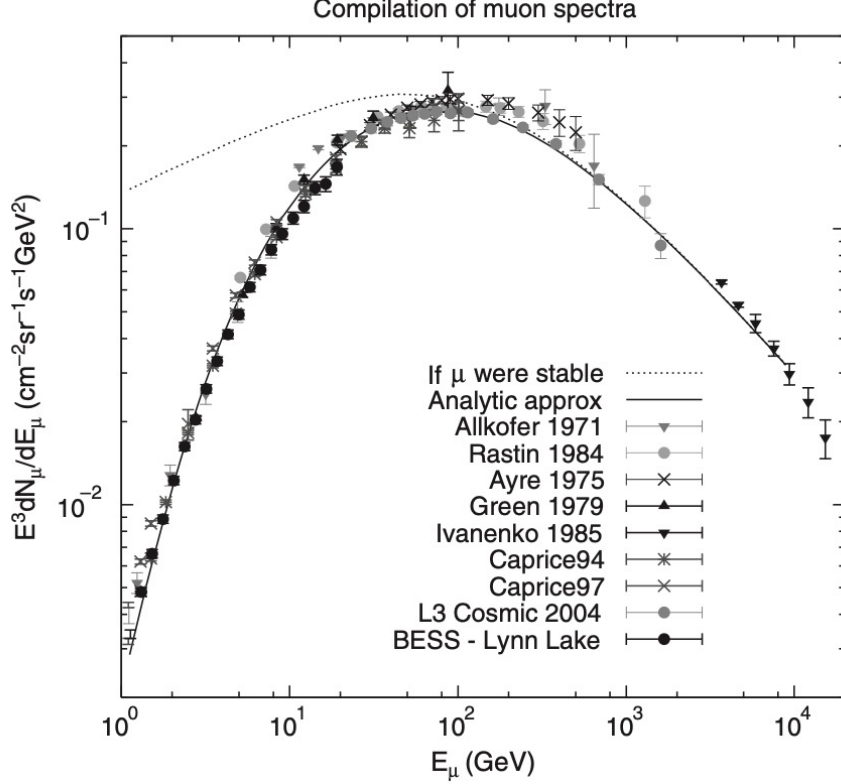


Figure 1.3: Comparison between the calculation of high muon energy flux and the measured data. In the high energy region ($E_\mu \gg \epsilon \simeq 1$ GeV), the effects of decay and energy loss are negligible ($E_\mu \approx E_{\text{org}}$). However, muon energy loss and decay become important below 200 GeV [5].

The cross sections of pions in a proton-proton interaction using Eq. (1.5) can be expressed as follows:

$$F_{p\pi^\pm}(E_\pi, E_p) = \frac{E_\pi}{\sigma_{pp}^{\text{inel}}} \frac{d\sigma_{p\pi^\pm}(E_\pi, E_p)}{dE_\pi}, \quad (1.21)$$

where E_p and E_π are the energies of the primary proton and secondary pion in the laboratory frame, and $\sigma_{pp}^{\text{inel}}$ is the total inelastic proton-proton cross section. Applying the hypothesis of the energy spectrum of Eq. (1.3) for primary particles, the pion energy spectrum can be expressed as:

$$\Pi^\pm(E_\pi) = \frac{dN_\pi(E_\pi)}{dE_\pi} = \frac{(\text{const})}{E_\pi} \int_{E_\pi}^{\infty} E^{-(\gamma+1)} F_{p\pi^\pm}(E_\pi, E_p) dE. \quad (1.22)$$

Defining $x_L = E_\pi/E$ and applying the same analogy as the spectrum-weighted moments from Eq. (1.11), Eq. (1.22) can be simplified expressed as:

$$\Pi^\pm(E_\pi) = (\text{const}) E_\pi^{-(\gamma+1)} Z_{p\pi^\pm}, \quad (1.23)$$

where $Z_{p\pi^\pm}$ is defined as:

$$Z_{p\pi^\pm} = \int_0^1 (x_L)^{\gamma-1} F_{p\pi^\pm}(x_L) dx_L. \quad (1.24)$$

Consequently, the muon charge ratio R_μ can be obtained as follows:

$$R_\mu \equiv \frac{\Pi^+(E_\pi)}{\Pi^-(E_\pi)} = \frac{Z_{p\pi^+}}{Z_{p\pi^-}}. \quad (1.25)$$

The remarkable features in this model are described as follows:

- Only pions contribute to the muon production. R_μ is independent of the muon energy.
- $R_\mu > 1$: As the primary particles consist mainly of protons, π^+ are more likely to be produced than π^- .
- R_μ depends on the γ of the primary spectrum.
- R_μ depends only on the projectile particle, not the target. Forward moving fragments with $x > 0$ contribute to $Z_{p\pi^+}$, and $F_{p\pi^+}(x > 0)$ relies on the projectile particle.

The numerical estimate for the charge ratio is derived by including the proton and neutron components as cosmic primaries.

Considering only muons produced from the decay of pions, the muon charge ratio can be expressed as follows:

$$R_\mu = \frac{1 + \delta_0 \mathcal{A}\mathcal{B}}{1 - \delta_0 \mathcal{A}\mathcal{B}} = \frac{f_{\pi^+}}{1 - f_{\pi^+}}, \quad (1.26)$$

where $\delta_0 \equiv (p_0 - n_0)/(p_0 + n_0)$ is the fraction of proton excess to the total particles (proton and nucleon) at the top of the atmosphere, and \mathcal{A} and \mathcal{B} are, described as:

$$\begin{aligned} \mathcal{A} &\equiv \frac{(Z_{p\pi^+} - Z_{p\pi^-})}{(Z_{p\pi^+} + Z_{p\pi^-})}, \\ \mathcal{B} &\equiv \frac{(1 - Z_{pp} - Z_{pn})}{(1 - Z_{pp} + Z_{pn})}, \end{aligned} \quad (1.27)$$

respectively, and $f_{\pi^+} = (1 + \delta_0 \mathcal{A}\mathcal{B})/2$ is the fraction parameter of positive muons to the decay of charged pions. The contribution from K^\pm to the muon charge ratio must also be considered. More K^+ is generated than K^- in the process, $p + air \rightarrow \Lambda + K^+ + \text{anything}$, which is difficult for K^- production. K^- can only be produced with an additional baryon and a strange particle creating a difference in the Z -moment between the pions ($Z_{p\pi^+} = Z_{n\pi^-}$) and kaons ($Z_{pK^+} \gg Z_{nK^-} \approx Z_{pK^-}$). The behavior of the charge ratio depends on the relative production ratio of kaons to pions. The contribution of kaons gradually increases as compared to that of pions at the critical energy range for pions, $E_\mu > \epsilon_\pi / \cos\theta$. Thus, the kaon production can affect the muon charge ratio especially at a higher energy range.

1.5 Fraction of atmospheric neutrinos

The improved contribution of kaon to the atmospheric neutrino production becomes considerably important as the energy increases. As described in the previous section, the fractional kaon production becomes significant above $\mathcal{O}(10^2)$ GeV to a few TeV energy range corresponding to $\epsilon_\pi < E \cos\theta < \epsilon_K$. Neutrinos from kaon decay carry almost half the energy of kaons, and this fraction is much large than that of pions, as mentioned in Section 1.2.3. Figure 1.4 shows the fraction of muons and neutrinos from the pion and kaon decays, respectively.

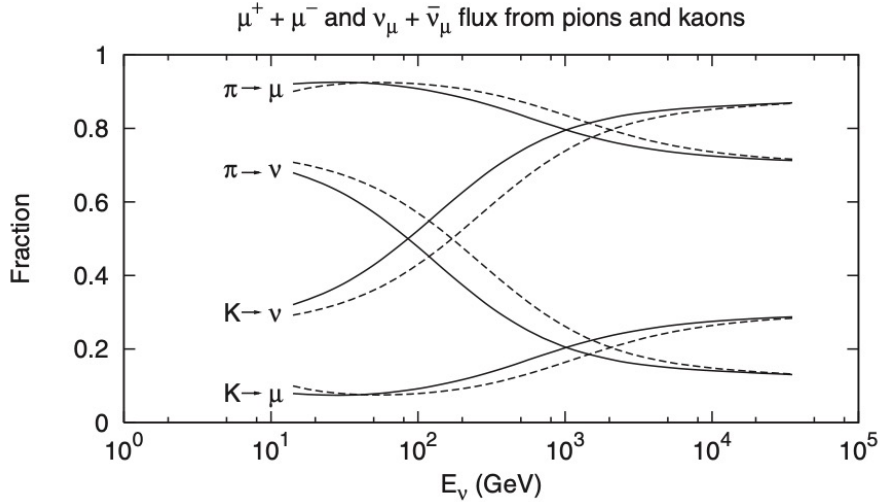


Figure 1.4: Fraction of atmospheric muons and muon neutrinos from pions and kaons decay. Solid lines represent for vertical and dashed lines for the zenith angle 60° [5].

1.6 Previous cosmic-ray muon charge ratio measurements

The measurements of the muon charge ratio have been performed in various experiments, as shown in Figure 1.5. The previous results of the charge ratio are obtained in the wide energy range from GeV to TeV. From previous measurements by Compact Muon Solenoid (CMS), L3+C below 1 TeV/c and Utah, MINOS, OPERA above 1 TeV/c, the charge ratio is approximately constant at $R(\mu^+/\mu^-) \approx 1.27$ in the momentum range of 10 – 300 GeV/c and increases in the higher momentum region. The increase in the charge ratio in the TeV energy region is considered a contribution from kaon decay to muon production, as explained in previous sections. Here, the overview of the past experiments is expressed below:

- **CMS experiment** [1]

CMS is one of the detectors installed at the Large Hadron Collider at CERN. The main physics target is searching for new signal in proton–proton collisions; however, it is extensively used to measure cosmic-ray muons. At the detector center, the magnetic field is parallel to the central axis (along the beam direction) of the solenoid. The muon momentum is reconstructed by measuring the muon trajectory curvature. CMS collected data in two cosmic-ray runs in 2006 and 2008, and performed most precise measurement of the charge ratio in the momentum region below 0.5 TeV/c.

- **L3 + C experiment** [7]

The precise muon magnetic spectrometer of the L3 detector is located at the LEP collider at CERN. The L3 inner detector is surrounded by the scintillator array, magnet, and drift chamber. After passing through the rock overburden, muons are measured by the scintillator and then, the direction is bended while traveling the drift chamber. The track position is measured in the drift chamber, and its momentum is obtained by determining its track radius. The absolute muon flux between 20 and 3,000 GeV is measured using the data collected between 1999 and 2000 for zenith angles ranging from 0° to 58° .

- **Utah experiment** [8]

The Utah cosmic-ray muon detector is located underground the Masatch Mountains at

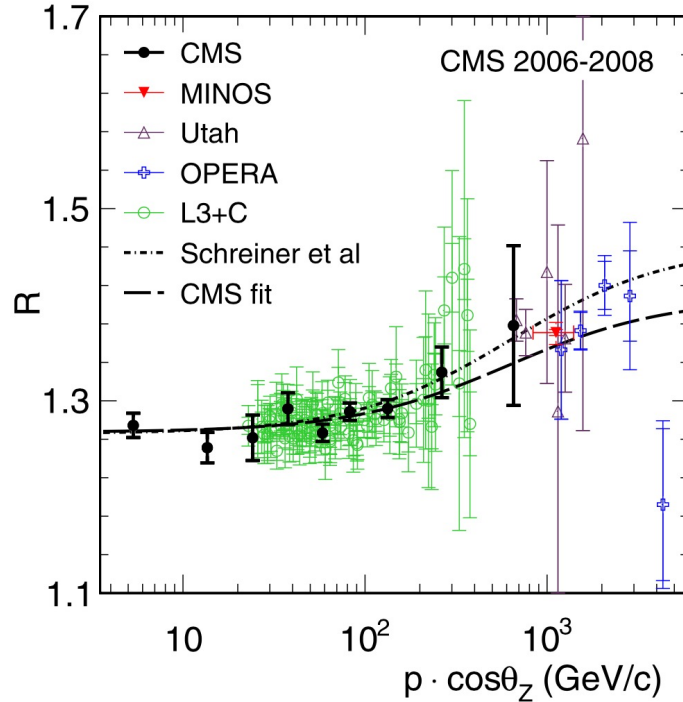


Figure 1.5: The previous measurements of the muon charge ratio as a function of the vertical muon momentum with a fit of πK model (see Chapter 6) [1].

Park City, Utah. The detector consists of cylindrical spark counter arrays filled with argon and ethylene, and water Cherenkov counter triggering the incoming muons and vertical ion magnets with a magnetic field about 16 kG. The muon trajectory is determined from the discharge of a cylindrical spark counter. Muons were collected for 765 days with energies between about 1 and 7.5 TeV at the zenith angle from 40° to 80° .

- **MINOS experiment** [9]

The MINOS far detector is a steel-scintillator and tracking calorimeter located at a depth of 2070 m.w.e. in the Soudan Underground Laboratory northern Minnesota, originally designed for the study of neutrino oscillations with the NuMI beam (Fermilab). Muon momentum is measured by magnetizing the steel with a toroidal field (about 1.3 T) along the detector's beam direction. MINOS recorded data between August 1, 2003 and February 28, 2006 with surface muon energies from 1 to 7 TeV.

- **OPERA experiment** [2]

The OPERA is a hybrid experiment with electronic detectors and nuclear emulsions, located underground at the Gran Sasso Laboratory in Italy at an average depth of 3,800 m.w.e. A dipolar iron magnet is instrumented with resistive plate chambers, and its magnetic field vertically transverses along the beam axis. The charge and momentum are determined via a similar method in other experiments using its magnetic spectrometer. The muon data corresponding to live time of 113.4 days during 2008 were collected for the measurement of the charge ratio with the energy range of about 890 GeV to 7 TeV as a function of vertical surface energy.

- **Kamiokande-II experiment** [10]

The Kamiokande-II (KAMIOKA Nucleon Decay Experiment) is a water Cherenkov detector located 1,000 m underground (2,700 m.w.e) in the Kamioka mine and is the pre-

decessor of the Super-Kamiokande experiment. It was designed to discover the proton decays and extensively used as it is for a neutrino detector. The operation period started in 1984 and ended in 1995. The muon charge ratio was measured for 978 effective days from January 1987 to April 1990 with the sea-level momentum of 1.2 TeV/ c and found to be $1.37 \pm 0.06(\text{stat}) \pm 0.01(\text{syst})$.

Chapter 2

Super-Kamiokande detector

2.1 Overview of Super-Kamiokande detector

Super-Kamiokande (SK) is the water Cherenkov detector located 1,000 m underground (2,700 m.w.e) in the Kamioka mine in Japan [11]. The detector consists of a cylindrical stainless steel tank. The tank contains 50 kilotons of ultra pure water. Since the detector is located deep underground, cosmic ray muons with energy over 1.3 TeV can penetrate the surrounding rocks (2,700 m.w.e) and reach the detector. The fourth phase of the SK experiment (SK-IV) began in September 2008 with the new electronics and data acquisition systems [12] (details are given in Section 2.5). The upgrade of electronic systems has enlarged the time window of event trigger and contributed to the high detection efficiency of the delayed signal of primary event. Experimental phases of SK are summarized in Table 2.1.

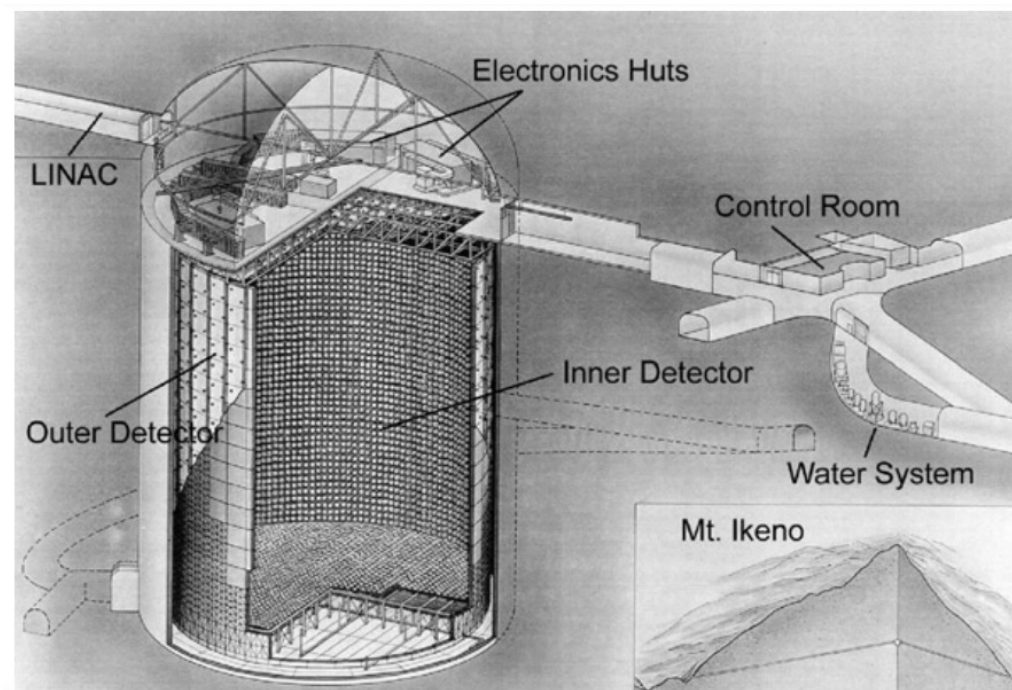


Figure 2.1: Schematic view of the SK detector [11].

Table 2.1: Experimental phases of SK. The live times are the duration of the observation after removing bad/calibration runs.

Phase	SK-I	SK-II	SK-III	SK-IV	SK-V	SK-VI ¹
Start	April 1996	October 2002	July 2006	September 2008	January 2019	July 2020
End	July 2001	October 2005	August 2008	May 2018	July 2020	Running
Live time [days]	1496	791	548	2970	379	-
ID PMTs	11,146	5,182	11,129	11,129	11,129	11,129
OD PMTs	1,885	1,885	1,885	1,885	1,885	1,885
PMT coverage [%]	40	19	40	40	40	40

2.2 Detector structure

2.2.1 Inner detector and outer detector

The structure of the SK detector consists of two regions, the inner detector (ID) and the outer detector (OD) as shown in Figure 2.1. Between the ID and OD, there is a stainless steel support structure about 60 cm wide to accommodate the PMTs, as shown in Figure 2.2. The ID consists of a cylindrical stainless steel tank, 33.8 m in diameter and 36.2 m in height. The ID is filled with 32.5 kton of ultra pure water and installed with 11,129 20-inch ID PMTs facing inward from the wall surface (inside the super module). In the SK-IV phase, 20-inch ID PMTs cover 40% of the surface area of the ID tank. The space between the ID PMTs is covered with a black sheet to reduce the unnecessary photon reflection.

The ID tank is surrounded by the OD tank with a thickness of 2.05 m on the upper and lower sides and 2.2 m on the lateral side. Approximately 17.5 kton of ultra pure water is contained in the OD tank and 1,885 8-inch PMTs are installed outwards on the tank wall (outside the super module). The OD wall is covered with white reflective sheet called the Tyvek sheet, used to prevent light from entering the ID tank. The main purpose of the OD is to identify the cosmic ray muons and to prevent the low energy gamma rays and neutrons, produced in the surrounding rocks from entering the ID.

The typical neutrino events react with the nuclei in the ID to generate charged particles emitting Cherenkov light without ringing OD. Conversely, charged particles, such as cosmic ray muons entering the SK, emit Cherenkov light while traveling through the water, which is detectable in both OD and ID. Therefore, neutrino and cosmic ray muon events can be distinguished by applying the signal information of OD and ID, as shown in Figure 2.3.

2.2.2 20-inch Photo Multiplier Tube (PMT)

Principle of PMT

To detect the Cherenkov light in water, a highly sensitive optical sensor is required. A PMT is an optical sensor using the mechanism of photoelectric effect to amplify weak light and converting it into an electrical current (Figure 2.4). The operation principle of PMT is described as follows:

- Photons in a specific wavelength region passing through the PMT's glass surface emit a number of electrons according to their energies on photocathode due to the photoelectric

¹Gadolinium sulfate dissolved in the ultra pure water [13].

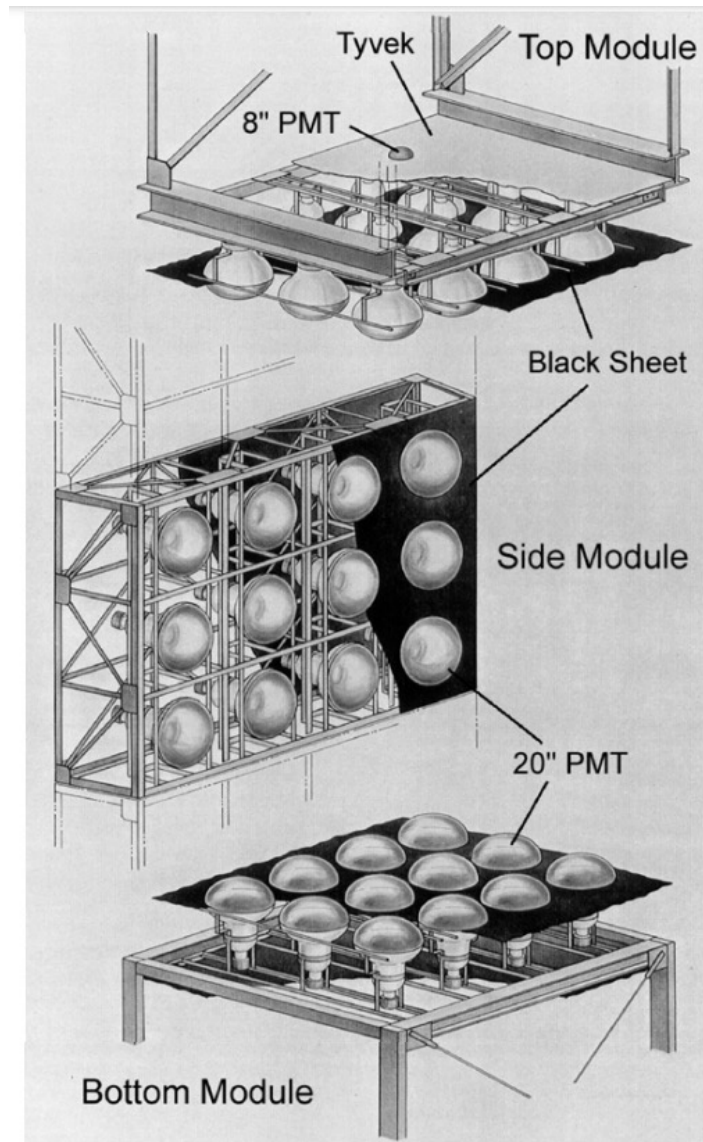


Figure 2.2: Schematic view of the PMT support structure [11].

effect.

- Photoelectrons are accelerated and converged by the focusing electrode and later amplified by the dynodes to produce multiple secondary electrons. Here, the inside of PMT is in a vacuum to improve the collection efficiency of photoelectrons and prevent internal discharge.
- Photoelectrons are accelerated by the electric field in the electron multiplier, and amplified by the subsequent dynode to create additional secondary electrons.
- The amplified secondary electrons are removed as a signal from the anode.

20-inch PMT

The 20-inch PMT used in the ID tank of SK is a type of Hamamatsu R3600, which is the type of spherical PMT and about 50 cm in diameter, as shown in Figure 2.5. The property of 20-inch PMT is listed in Table 2.2. The photocathode of the PMT is made of bialkali (Sb-K-Cs) and

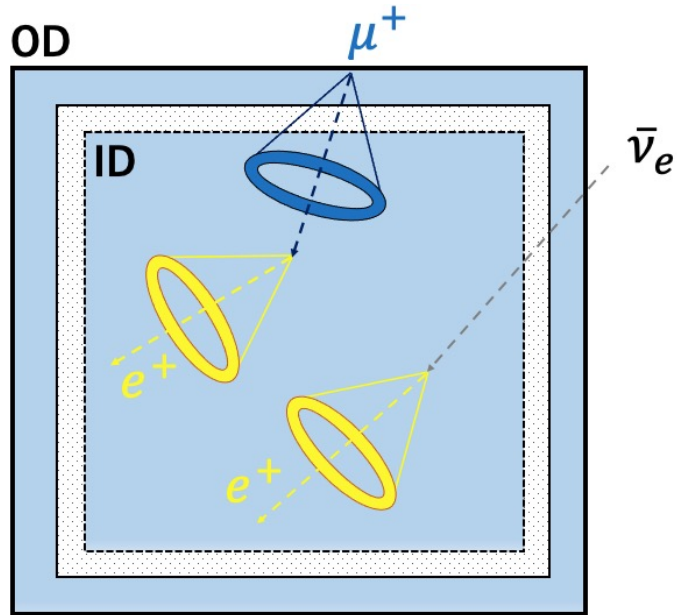


Figure 2.3: Topology of the muon decay event and neutrino event in SK tank.

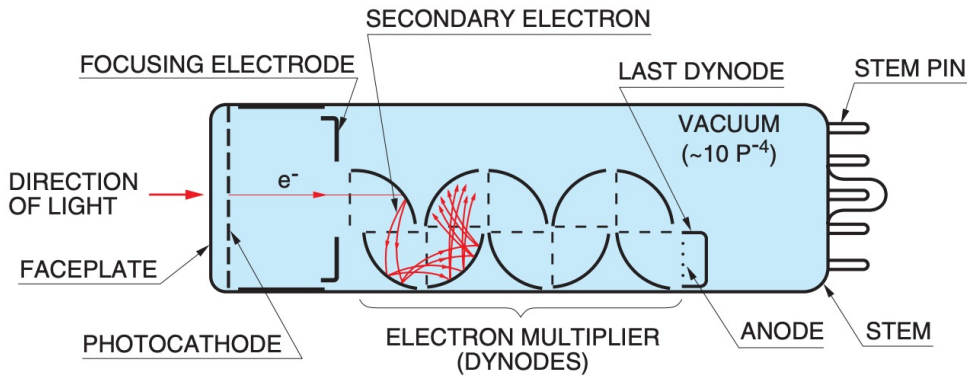


Figure 2.4: Construction of a PMT (The PMT shown above is the type of Head-on) [14].

its sensitive wavelength region spans from 280 to 660 nm. The wavelength dependence of the quantum efficiency is the most sensitive around 360 nm, as shown in Figure 2.6. Figure 2.7 shows that the transit time distributed about 2.2 nsec (1σ resolution) for single photoelectron (p.e.) and the one 1 p.e. distribution of the ID PMT with a wavelength of 410 nm light is shown in Figure 2.8.

Table 2.2: The property of 20-inch PMT.

Product Name	Hamamatsu R3600
Photocathode Area	50 cm diameter
Photocathode Material	Bialkali(Sb-K-Cs)
Collection Efficiency	70%
Dynode	11 Stage Venetian Bind Type
Quantum Efficiency	21% (360 nm)
Gain	10^7 (1700 - 2000 V)
Dark Noise Rate	3 kHz
Timing Resolution	2.2 nsec(1σ)
Drift Time	100 nsec
Weight	13 kg
Pressure Tolerance	6 kg/cm^2

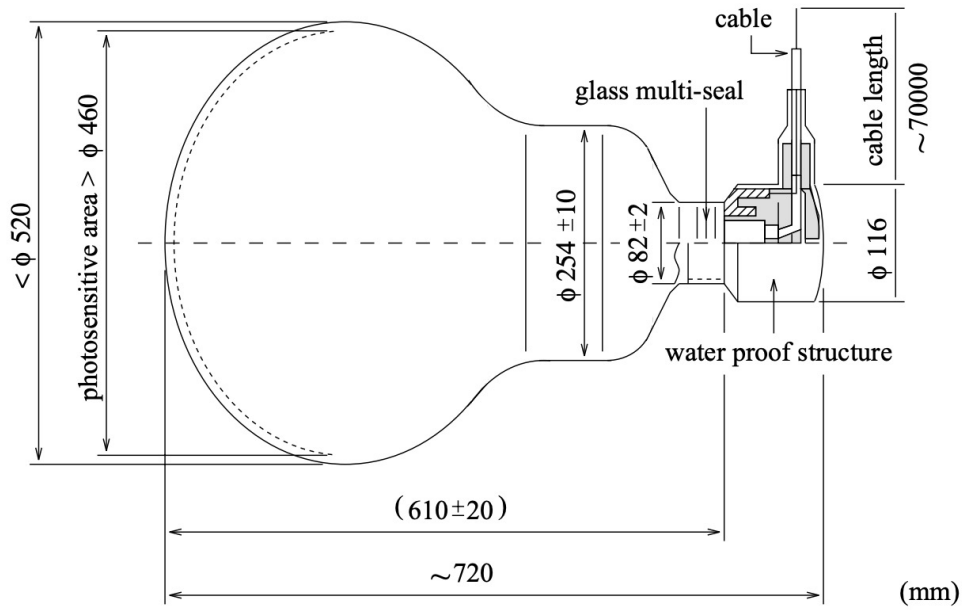


Figure 2.5: 20-inch ID PMT [11].

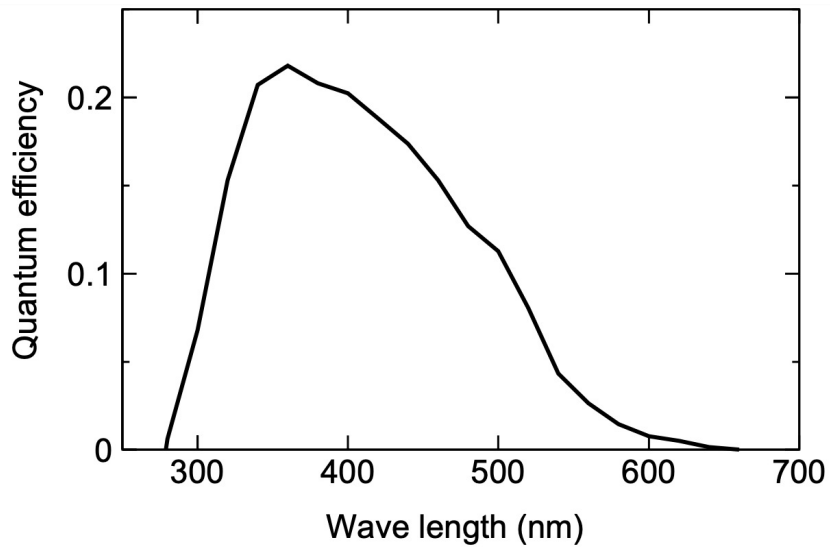


Figure 2.6: Quantum efficiency of the ID PMT as a function of wavelength [11].

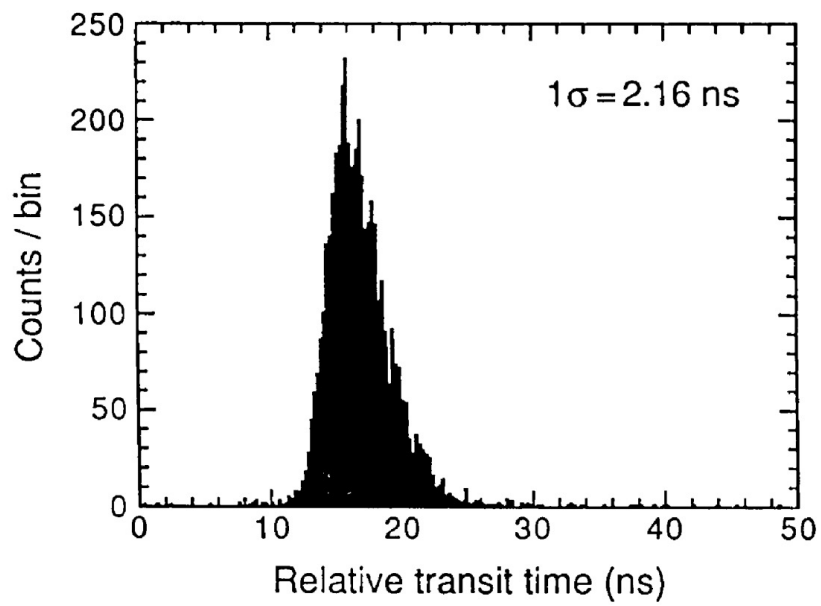


Figure 2.7: Distribution of 1 p.e. pulse height of ID PMT with 410 nm wavelength light [11].

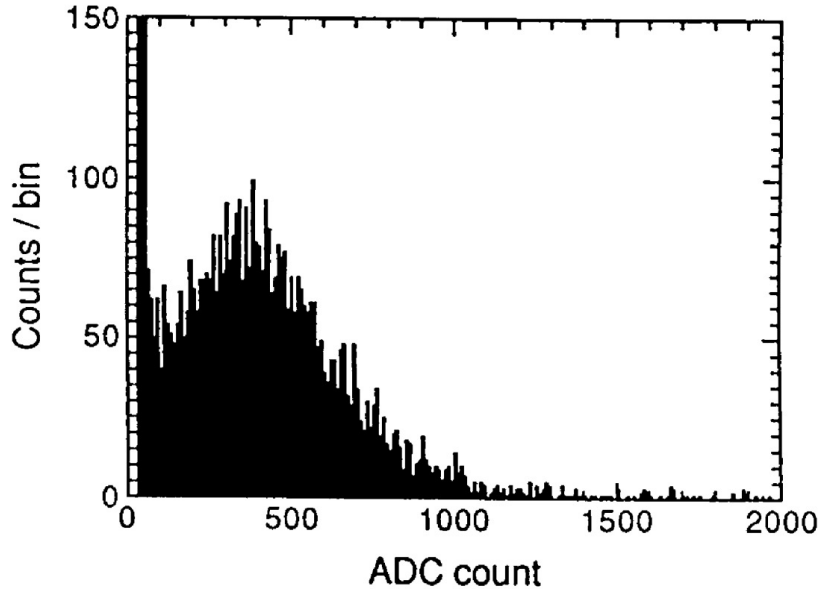


Figure 2.8: Distribution of relative transit time of ID PMT with 410 nm wavelength light [11].

Acrylic and a FRP (Fiber Reinforced Plastic) cases

After the serious accident in 2001, SK has installed a PMT case to protect PMTs from the shock wave caused by the explosion of PMTs. The surrounding part of the PMT surface is covered with a highly transparent acrylic case, and the other is covered with the Fiber Reinforced Plastics (FRP), as shown in Figure 2.9.



Figure 2.9: Schematic view of acrylic and a FRP cases [15].

2.2.3 Helmholtz coils

The photoelectrons generated inside the PMT are affected by the geomagnetic field, possibly reducing the collection efficiency. Twenty-six sets of Helmholtz coils are installed around the water tank to reduce the effects of the geomagnetic field, as shown in Figure 2.10. The original magnetic field was about 450 mG and 32 mG pre and postelectric current application,

respectively [16].

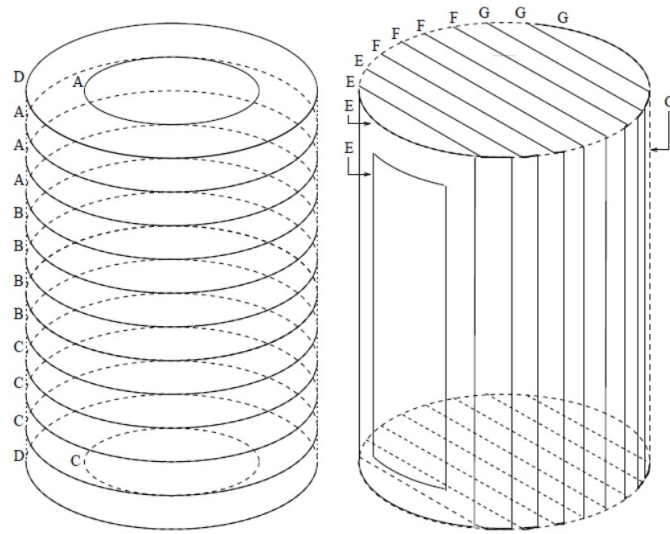


Figure 2.10: Schematic view of Helmholtz coils surrounding the SK tank [15].

2.3 Detection principle

In the SK detector, the Cherenkov light emitted by the charged particles in water is detected by each PMT. The Cherenkov light is emitted by the charged particles moving faster than the speed of light in a medium. The schematic view of Cherenkov radiation is shown in Figure 2.11. The Cherenkov light is emitted in a conical shape at an angle θ_C satisfying the following equation relative to the traveling direction of the charged particle:

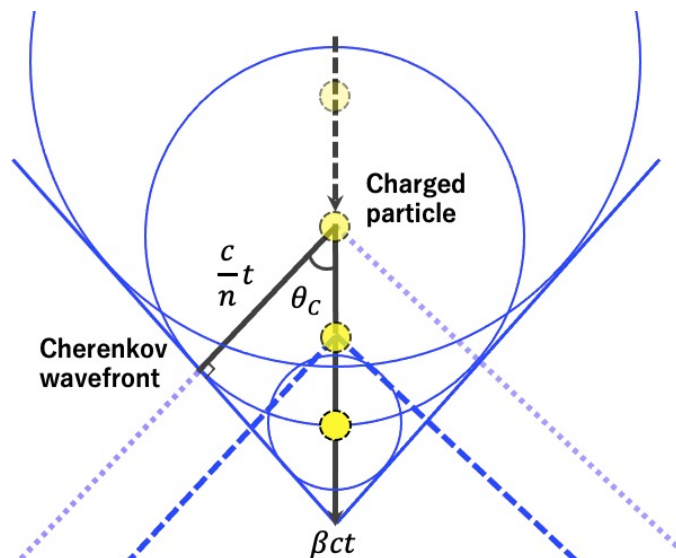


Figure 2.11: Formation of Cherenkov radiation.

$$\cos \theta_C = \frac{1}{\beta n}, \quad (2.1)$$

where n is the refractive index of the medium, and β is the fraction of the velocity ($= v$) of a particle to the speed of light ($= c$) in a vacuum (e.g., $\beta = v/c$). Since the refractive index of pure water is $n = 1.34$, when a charged particle runs at a speed close to the speed of light ($\beta \simeq 1$), the Cherenkov angle becomes $\theta_C \simeq 42^\circ$. A charged particle emits light along its movement direction until its speed drops below the speed of light, with the light projected on the wall as a ring is referred to as the Cherenkov ring. The energy threshold of Cherenkov radiation is given as the following equation:

$$E_{\text{thr}} = \frac{mc^2}{\sqrt{1 - \beta^2}} = \frac{mc^2}{\sqrt{1 - \left(\frac{1}{n}\right)^2}}, \quad (2.2)$$

Here, at the threshold of Cherenkov radiation ($\cos \theta_C \leq 1$), $\beta = 1/n$. The charged particle with the energy satisfying $E_{\text{thr}} \leq E$ can emit the Cherenkov light. The threshold varies according to the mass of charged particles, as shown in Table 2.3 as for pure water ($n = 1.34$).

Table 2.3: Energy threshold of Cherenkov radiation for various particles in pure water.

Particle	Rest Mass [MeV/c ²]	Energy Threshold [MeV]
e^\pm	0.5110	0.7675
μ^\pm	105.7	158.7
π^\pm	139.6	209.7
K^\pm	493.7	741.7
p^\pm	938.3	1410

The number of photons dN emitted as Cherenkov light while a particle travels in a medium with a refractive index n at a velocity β for a small distance dx is given by the following equation:

$$\frac{d^2N}{dx d\lambda} = \frac{2\pi\alpha Z^2}{\lambda^2} \left(1 - \frac{1}{n^2\beta^2}\right) \quad (2.3)$$

where λ is the wavelength of photon, α is fine-structure constant, and Z is charge. The number of Cherenkov photons emitted from electron per unit cm in the wavelength range, $\lambda = 300 \text{ nm} \sim 600 \text{ nm}$ can be obtained by taking the integration of Eq. (2.3) as follow:

$$N = \int_0^{1 \text{ cm}} dx \int_{300 \text{ nm}}^{600 \text{ nm}} d\lambda \frac{2\pi\alpha}{\lambda^2} \left(1 - \frac{1}{n^2\beta^2}\right) \simeq 340. \quad (2.4)$$

2.4 Water and air circulation system

2.4.1 Water purification system

The ultra pure water of the SK detector is generated by purifying the groundwater in the Kamioka mine. However, groundwater contains several impurities including small dust, metal ions, bacteria, and radioactive sources. These impurities scatter or absorb Cherenkov light and affect light transmission in water. In addition, radioactive sources dissolved in water create

background events for observations. According to the reasons above, water purification is essential to remove impurities, which reduces the accuracy of the physics measurement. To maintain high purity, water is constantly circulated inside the detector at a rate of 60 tons/h in the SK-IV. The water is retrieved from the top of the tank and poured from the bottom after the purification, as shown in Figure 2.12. The process of water purification system in SK-IV is explained as below:

- 1 μm mesh filter
Removes the dust larger than 1 μm and the radioactive contaminations in water.
- Heat exchanger
The water temperature increases due to the heated pump used in water circulation and PMTs. The heated water increases the dark rate of PMTs, bacteria in water, and convection in tank. It is required to suppress the water convection to prevent radon mixed from the wall from spreading to the whole area inside the tank. The water temperature is adjusted to about 13°C.
- Ion exchanger
Removes ions in water, including Ni^{2+} , Ca^{2+} , Fe^{2+} , Co^{2+} , Cl^- and so on.
- UV sterilizer
Radiates ultraviolet (UV) light to water to kill bacteria.
- Radon less air dissolving system
Dissolves Rn free air in water to increase the radon gas removal efficiency.
- Reverse osmosis filter
Removes the contaminants in the water.
- Cartridge polisher
Removes the ions dissolved in water with 99% efficiency.
- Ultra filter
Removes dust particles larger than 10 nm.
- Membrane degasifier
Removes radon and oxygen dissolved in water.

The radon concentration in the ultra pure water after purification is reduced to 1 mBq/m³ or less with the water transparency of about 100 m [17].

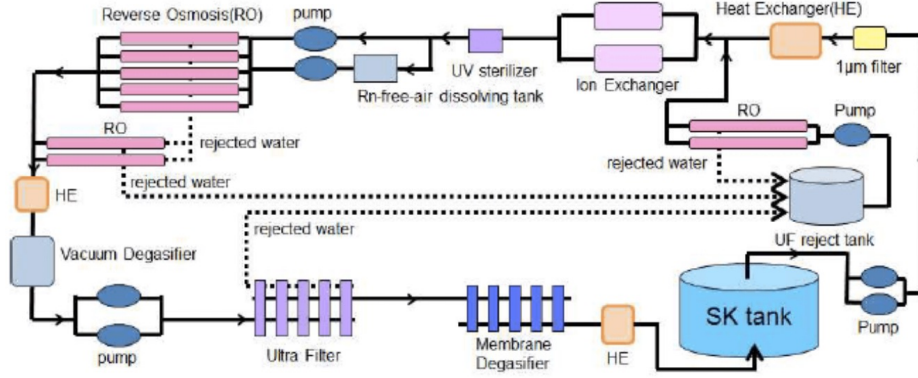


Figure 2.12: Schematic view of the water purification system [15].

2.4.2 Air purification system

Rn produced by Uranium exists around the Kamioka mine and these radioactive sources are contained in the surrounding rock of the SK detector. In the MeV energy regions, the background events from Rn are dominant; hence, it is necessary to reduce the Rn concentration in both water and air. In the SK tank, there is some distance between the water surface in the tank and the top side of the detector. The purified air (Rn free air) is passed into the tank to prevent Rn from dissolving into the water. The schematic view of the air purification system is shown in Figure 2.13, with the process described below:

- Compressor
Compresses the air around 7.5 – 8 atm.
- Air filter
Removes dust particles in the compressed air. 0.3, 0.1, and 0.01 μm filters are set, and 0.1 and 0.01 μm filters are used after the process in the carbon column section.
- Air drier
Removes water from the air to improve the Rn removal efficiency.
- Carbon column
Removes Rn in the air by using the carbon column which can absorb Rn.
- Cooled carbon column
Lowers the temperature of carbon column to -40°C (changed to -60°C during SK-IV period) to increase the Rn removal efficiency [18].

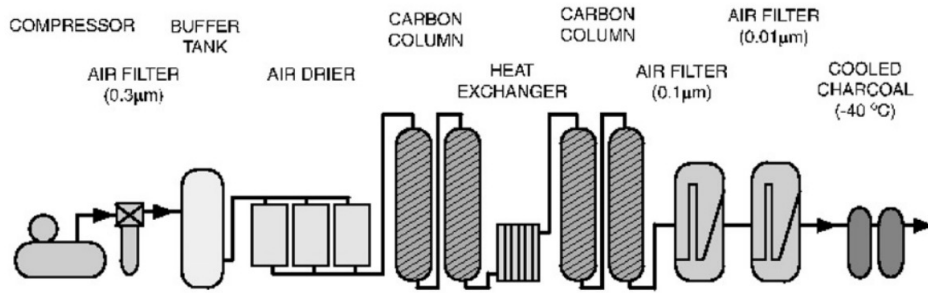


Figure 2.13: Schematic view of the air circulation system [11].

2.5 Data acquisition system in SK-IV

A data taking with a new electronics module (QBEE) started from September 2008. The data acquisition process in SK-IV is discussed below.

2.5.1 QBEE

Since the SK-IV phase, data has been collected by a new front-end electronics module, QBEE (Charge-to-Time-Converter-Based Electronics with Ethernet). The analog signal from the PMT is sent to the electronics hat at the top of the tank via a 70 m cable and digitized by the front-end electronics module. Hit timing information and the integrated signal charge are sorted in chronological order in the computer and processed as an event by applying software trigger, and later stored on the disk. In QBEE, the analog signal is converted into a square wave by the charge-to-time-converter (QTC) and then, its signal is digitized by time-to-digital converter (TDC). Here, each QBEE has height QTCs, and each QTC processes three PMTs (a QBEE processes 24 PMT signals). A block diagram of QTC and its peripheral devices is shown in Figure 2.14.

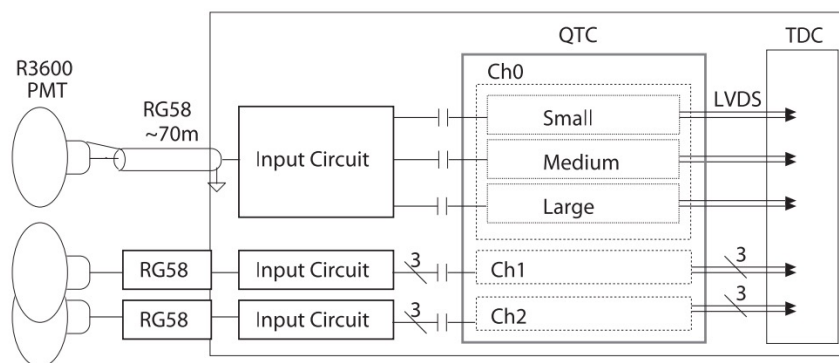


Figure 2.14: Block diagram of the QTC and its peripheral devices [19].

QTC has three gain range channels, Small, Medium, and Large and the ranges are determined depending on the detected charge with the relative gain ratio, 1: 1/7: 1/49. The charge range spans from 0.2 to 2,500 pC. The PMT signal is treated follows steps: The flag (HIT) is issued when the signal exceeds the certain discriminator threshold. If the HIT is issued, three gates

are open in the order of charge gate, discharge gate, and VETO gate. The process time for a signal requires approximately 900 nsec. The signal and timing chart of QTC is shown in Figure 2.15. Here, the rising edge of the square wave is the hit timing, and the pulse width corresponds to the amount of charge.

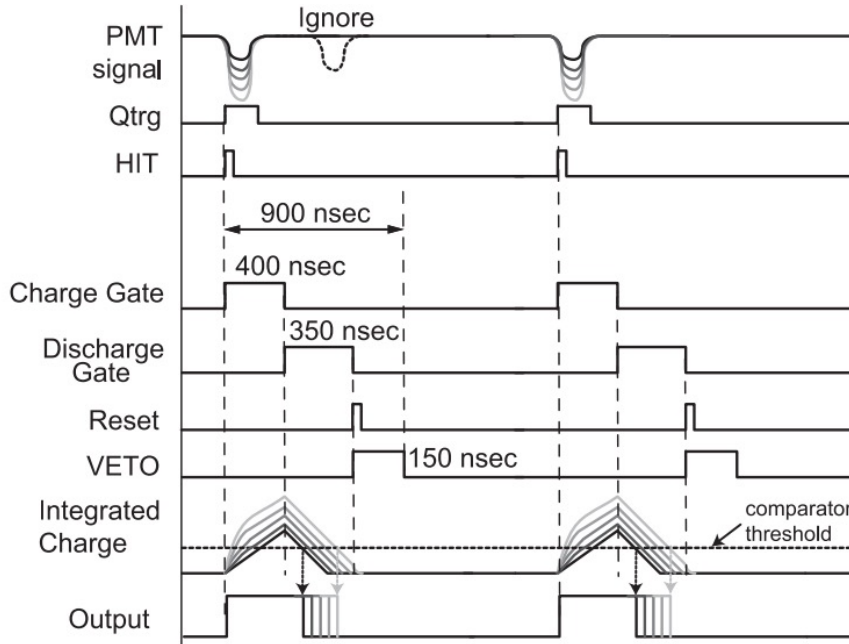


Figure 2.15: Timing chart for the QTC operation. The gradation of color indicates the integrated charge of PMT signals [19].

2.5.2 Software trigger

Since the signals are treated with high speed digital processing, all PMT hit information are collected in a merger PC. Several triggers are set for an event selection depending on the number of hit PMTs. The number of PMT hits in a time width of 200 nsec defined as N_{200} , is used, which is triggered when a signal exceeds a certain threshold. Table 2.4 summarizes the types of software triggers set in the SK-IV phase with the N_{200} threshold for the trigger conditions, and time width. In the energy region of SLE trigger, the time width is set to 1.5 μ sec owing to the high rate resulting from the radioactive background events. Super High Energy (SHE) and After-Window (AFT) triggers were newly added for the analysis of supernova relic neutrino search. The AFT trigger is issued and all hits information within the 500 μ sec time window is recorded if N_{200} exceeds the SHE trigger threshold.

Table 2.4: Summary of trigger threshold of hit PMTs within a 200 nsec window (N_{200}) in SK-IV and its time width.

Trigger Type	N_{200} Threshold [hits/200 nsec]	Time Width [μ sec]
Super Low Energy (SLE)	34 \rightarrow 31 (After May 2015)	$[-0.5, +1.0]$
Low Energy (LE)	47	$[-5, +35]$
High Energy (HE)	50	$[-5, +35]$
Super Low Energy (SHE)	70 \rightarrow 58 (After September 2011)	$[-5, +35]$
AFT	58	$[+35, 535]$
Outer Detector (OD)	22 in OD	$[-5, +35]$

Chapter 3

Event reconstruction

In the SK experiment, an event reconstruction varies according to its physical target and analysis. Especially for the muon decay analysis, muon events are reconstructed using the specific fitter working differently from that of the decay electrons. In this chapter, the reconstruction methods for muon and decay electron events are explained, respectively.

3.1 Reconstruction of muon

Cosmic-ray muons observed at SK are classified into six categories: No-fit, Single through-going muon, Stopping muon, Multiple muon-1, Multiple muon-2, or Corner-clipping muon. Figure 3.1 shows the four types of classified muon events as an example. Each of the muon events in Figure 3.1 are defined as, (I) Single through-going muons: events penetrating the ID, (II) Stopping muons: events stopping inside the ID, (III) Multiple muons: events with several tracks, and (IV) Corner-clipping muons: events with a short track length, scraping the edges of the ID.

The event reconstruction for muon events is performed by the so-called Muboy fitter using several algorithms to identify as per the muon types. Muboy determines if the event has a single track or multiples tracks in the ID at the first guess, and then, sees if it stopped in the ID or not.

Muboy was originally developed by R. Svoboda to fit muon events producing spallation products and a source of background for the low energy solar neutrino analysis. The Muboy fitter is applied for both actual and simulated data. Here, the overview and main feature of the Muboy fitter is discussed and more details can be found in [20], [21].

3.1.1 Cleaning cuts

At first, the cleaning cut is applied for PMT selection. The selection criteria require the PMT's charge to be greater than a certain threshold. This threshold is determined based on the number of hit PMTs (N_{hit}) per event. The charge thresholds for the first cleaning cuts are listed in Table 3.1.

After the first cleaning cut is applied, Muboy counts the number of nearest neighbors of each hit PMT within 10 nsec (N_{near}). Then, Muboy defines its second cleaning cut and selects only those hit PMTs with N_{near} larger than a certain threshold depending on the number of PMTs after the first cleaning cut, as shown in Table 3.2.

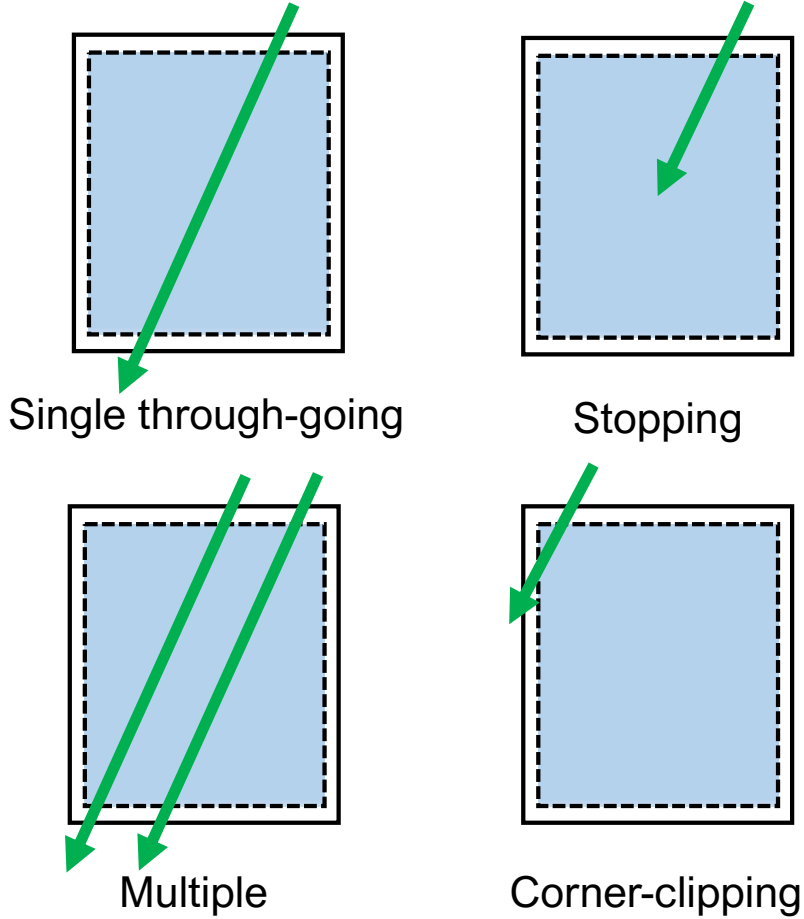


Figure 3.1: Four types of cosmic-ray muon events observed at the SK detector.

3.1.2 Entry point

The entry point estimation is performed by selecting the earliest PMT with has at least three nearest neighbors hit within 10 nsec. If no PMT meets the criterion, the required conditions for the number of nearest neighbors are reduced by one. The entry point is the coordinate of the earliest ID PMT and the entry time is the timing of the earliest PMT hit. The expected exit point is the center of nine selected PMTs among all remaining PMTs containing the maximum charge. The direction of the muon track is given by the vector from its entry point to the exit point. Then, Muboy applies further causality cuts to reduce hits produced by multiple muons and scattered light.

3.1.3 Direction reconstruction

If a single muon, with known entry point and time, enters the ID, the timing of hit PMTs cannot get a hit earlier than the travel time of muon in water (T_{early}). However, if there are multiple muons then there can be early hits than T_{early} . The total number of hit PMTs (N_{early}) with hit times less than T_{early} are counted as N_{early} . Here, T_{early} is defined as follows:

$$T_{\text{early}} = T_{\text{entry}} + \frac{D}{v_1}, \quad (3.1)$$

where T_{entry} is the hit time of the entry point PMT, D is the distance between the entry points

Table 3.1: Number of hit PMTs (N_{hit}) and the corresponding limit on the PMT charge of all selected ID PMTs in Muboy fit.

N_{hit}	Threshold charge of selected ID PMT
> 10000	3.0 p.e.
8000 - 10000	2.5 p.e.
< 8000	2.0 p.e.

Table 3.2: Lower limits on the number of nearest neighbors (N_{near}) corresponding to the number of PMTs selected after the first cleaning cut.

N_{hit} after first cut	N_{near} cut
> 7500	5
5000 - 7500	4
2500 - 5000	3
500 - 2500	2
< 500	1

and the hit PMT, and v_1 is the muon speed, set as 34.0 cm/nsec. Multiple muons can hit PMTs less than v_1 and can be recognized by counting N_{early} . If $N_{\text{early}} > 45$, then the event is classified as a multiple muon-category-1 (Multiple muon-1) and all events of this category are treated separately to estimate their entry points and directions. In contrast, the PMT hit produced by the direct light of photons originated from a muon, cannot be hit later than the travel time of light in water. Here, T_{later} is defined as:

$$T_{\text{later}} = T_{\text{entry}} + \frac{D}{v_2}, \quad (3.2)$$

where v_2 is the speed of light in water, set as 18.0 cm/nsec. The remaining hit PMTs with hit times are between T_{early} (obtained from Eq. (3.1)) and T_{later} are used for direction fitting. The muon entry point and its direction toward the hit PMTs are in the Cherenkov cone, if each hit PMT satisfies at least one of the following two conditions:

- $\vec{d} \cdot \vec{r} > 0.74$
where \vec{d} is a unit vector from the entry point to hit PMT and \vec{r} is the muon track direction.
- Distance between the entry point and the hit PMT is less than 2 m.

Once the hit PMTs in the Cherenkov cone are selected, Muboy estimates the direction and recalculates it until the goodness of fit (GOF) parameter is maximized. The GOF parameter is defined as:

$$\text{GOF}(f_{\text{cone}}) = \sum_{i=1}^N g(\delta t_i), \quad (3.3)$$

where f_{cone} is the number fraction of hit PMTs in the Cherenkov cone, $\delta t_i (= T_{\text{expected}} - t_i)$ is the time residual, t_i is the measured time of i -th PMT, and T_{expected} is the expected time at

which the PMT should be hit from a given muon track and direction. The function $\text{GOF}(f_{\text{cone}})$ takes the following form:

$$\begin{aligned} f_{\text{cone}} < 0.75 & : \text{GOF}(f_{\text{cone}}) = f_{\text{cone}} \frac{0.9}{C_{\text{cut}}}, \\ f_{\text{cone}} > 0.75 & : \text{GOF}(f_{\text{cone}}) = \frac{0.1f_{\text{cone}} + 0.9 - C_{\text{cut}}}{1 - C_{\text{cut}}}, \end{aligned} \quad (3.4)$$

where $C_{\text{cut}} = 0.74$. The function $g(\delta t_i)$ is defined as follows:

$$\begin{aligned} \delta t_i < 0 \text{ or } q_i > 30 \text{ p.e.} & : g(\delta t_i) = \exp \left[-\frac{(\delta t_i - t_{\text{mean}}(q_i))^2}{2\sigma^2} \right], \\ \delta t_i > 0 & : g(\delta t_i) = \exp \left[-\frac{\delta t_i}{\lambda} \right], \end{aligned} \quad (3.5)$$

where,

$$\begin{aligned} \sigma & = 1.690 + 2.514 \exp \left[-\frac{q_i}{2.453} \right] [\text{nsec}], \\ \lambda & = 1.254 + 14.863 \exp \left[-\frac{q_i}{2.316} \right] [\text{nsec}]. \end{aligned} \quad (3.6)$$

The estimation of direction is iterated around the first guess direction while keeping the entry point and time fixed until $\text{GOF}(f_{\text{cone}})$ is maximized. Once the best fit direction is determined, a second iteration is performed for all events. At this point, if the track direction is changed, the entry time is also allowed to change. The entry time is calculated with hit PMTs occurring within a 26.7 nsec time window around the track. Then, the $\text{GOF}(f_{\text{cone}})$ is again calculated with C_{cut} in Eq. (3.4), replaced by $C_{\text{cut}} = 0.65$. After the second maximization, the number of early hit PMTs under the condition, $\delta t_i - t_{\text{mean}}(q_i) > 250$ are counted, when larger than 35. These muons are categorized as Multiple muon-2. Any other remaining event is classified as a through-going muon. Additionally, Muboy calculates another goodness parameter for upward-going muon reduction produced by the high-energy atmospheric neutrinos by interacting with the surrounding rock of the detector. The goodness is defined as:

$$F_{\text{cone}} = \frac{\sum q_i}{\sum Q_i}, \quad (3.7)$$

where $\sum q_i$ is the sum of all detected charges remaining after the cleaning cuts explained above and $\sum Q_i$ is sum of all detected charges in the Cherenkov ring. The distribution of both $\text{GOF}(f_{\text{cone}})$ and F_{cone} can be found in Figure 3.2.

3.1.4 Event classification

For the categorization of muon events, all Single through-going muons with a track length shorter than 7 m and the total number of hit PMTs less than 2,000 are examined for the possibility to be Corner-clipping muons. Corner-clipping muon events scrape the edges of the ID and have relatively short track lengths. If an entry point is near the top corner and satisfies the following condition,

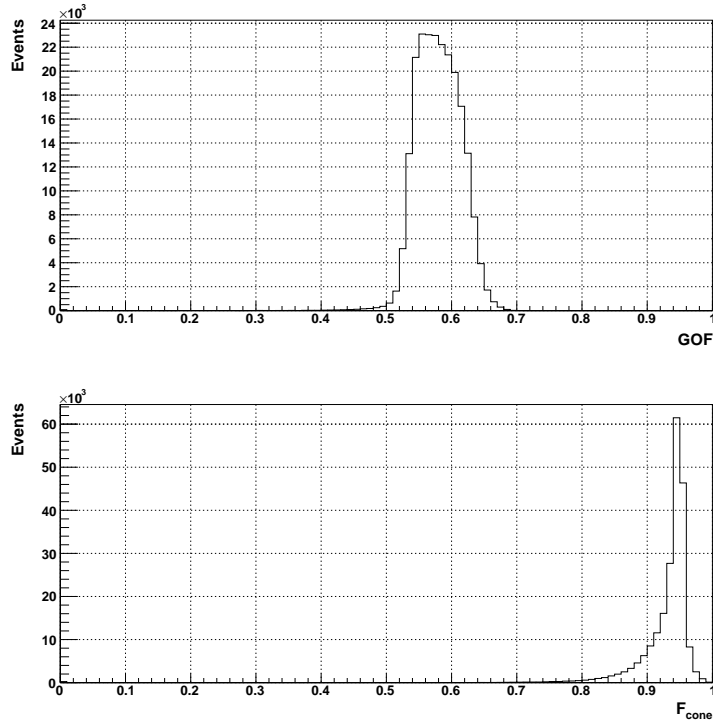


Figure 3.2: Distribution of two parameters, GOF and F_{cone} used in Muboy in assessing quality of the fit.

$$\frac{X_{\text{entry}} \cos \theta_x + Y_{\text{entry}} \cos \theta_y}{\sqrt{X_{\text{entry}}^2 + Y_{\text{entry}}^2}} > 0.05, \quad (3.8)$$

the event is classified as a Corner-clipping muon. Here, $X_{\text{entry}}, Y_{\text{entry}}$ are the coordinates of the entry position of a muon. Conversely, if the muon enters near the bottom corner and the distance between the entry and exit points is less than 4 m, then this event is also classified as a Corner-clipping muon.

Then, Muoby then examines the remaining events as to whether they are Stopping muon events or not. To identify the Stopping muon events, the number of photo-electrons produced within 2 m (Q_{ID}) from the exit point in the ID and within 4 m from the exit point in the OD (Q_{OD}), are counted. An event is classified as a Stopping muon, if it satisfies at least one of the following requirements:

- $Q_{\text{ID}} < 200$ p.e.
- $Q_{\text{ID}} < 400$ p.e. and $Q_{\text{OD}} < 30$ p.e.
- $Q_{\text{OD}} > 30$ p.e. and $Q_{\text{ID}} < 150$ p.e.
- No OD data and $Q_{\text{ID}} < 150$ p.e.

Muoby proceeds to calculate the track length of the Stopping muon. The track length is determined by considering the observed energy loss via Cherenkov light emission per unit track

length, dE/dX , corresponding to the amount of detected light per unit track length. Figure. 3.3 shows an example of the dE/dX distribution in 0.5 m bins together with the stopping point. The stopping point is when dE/dX becomes less than 40% of the average value of the first 1.5 m (Figure 3.3) and the muon track length becomes greater than the peak position of the dE/dX histogram.

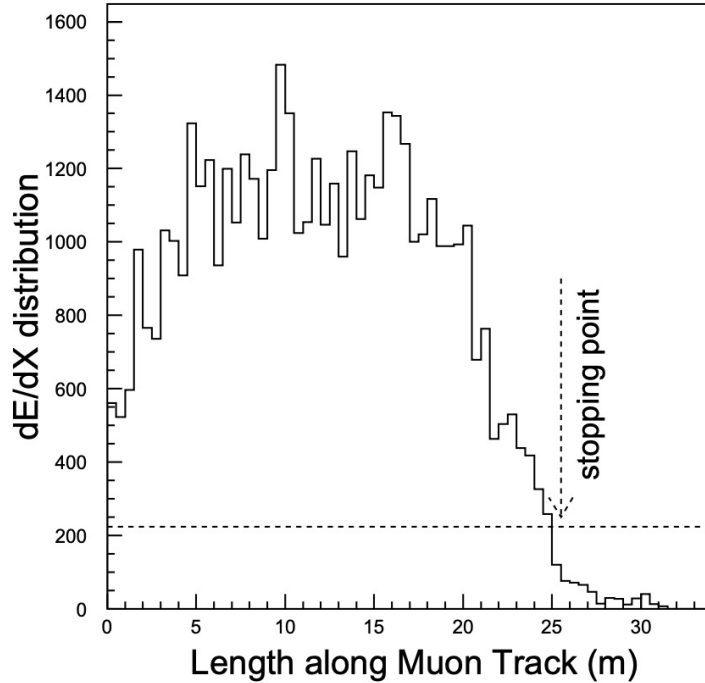


Figure 3.3: The histogram of dE/dX distribution for the track length determination of Stopping muons [21]. The stopping point is determined at 25 m.

3.2 Reconstruction of decay electron

Low energy events with the total energy below 100 MeV are reconstructed using the hit pattern of PMTs (direction), the timing information (vertex), and the number of hit PMTs (energy). The method of vertex, direction and energy determination are explained as below.

3.2.1 Vertex reconstruction

In the low energy region, the charged particles with the energy of 20 MeV travel only 10 cm in water. Therefore, the track length is negligible and can be assumed as the occurrence point of the event. To reconstruct the vertex position, the timing information of each hit PMT is used. The reconstruction of the vertex position is performed by the maximum likelihood fit of the timing information using an algorithm, called BONSAI (Branch Optimization Navigating Successive Annealing Iterations) [22]. The residual time of each PMT hit is defined as:

$$t_{\text{res},i} = t_i - t_{\text{tof}} - t_0, \quad (3.9)$$

where, t_i is the hit time of the i -th PMT, the t_{tof} is the time of flight between the vertex position (x, y, z) to the hit PMT, and t_0 is the generated time of the charged particle. Using the residual time information, the likelihood function is defined as:

$$\mathcal{L}(\vec{x}, t_0) = \sum_{i=1}^{N_{\text{hit}}} \log \{P(t_{\text{res}, i})\}, \quad (3.10)$$

where \vec{x} is a candidate vertex position and $P(t_{\text{res}, i})$ is the probability density function of the residual time calibrated by the LINAC calibration device, as shown in Figure 3.4. The likelihood function $\mathcal{L}(\vec{x}, t_0)$ is calculated at each point while changing \vec{x} in the ID, and the position where the value becomes the maximum is determined as the vertex position of that event. The number of Cherenkov photons emitted by a charged particle differs according to its energy, resulting in the difference in the number of hit PMTs. Therefore, the accuracy of vertex reconstruction depends on the energy of the charged particle. Figure 3.5 shows the energy dependence of the vertex resolution obtained by the LINAC calibration. Here, the resolution of the reconstructed vertex position is defined as the reconstructed events in the region about 68% (1σ) of the distribution of the distance between the true and the reconstructed vertex positions.

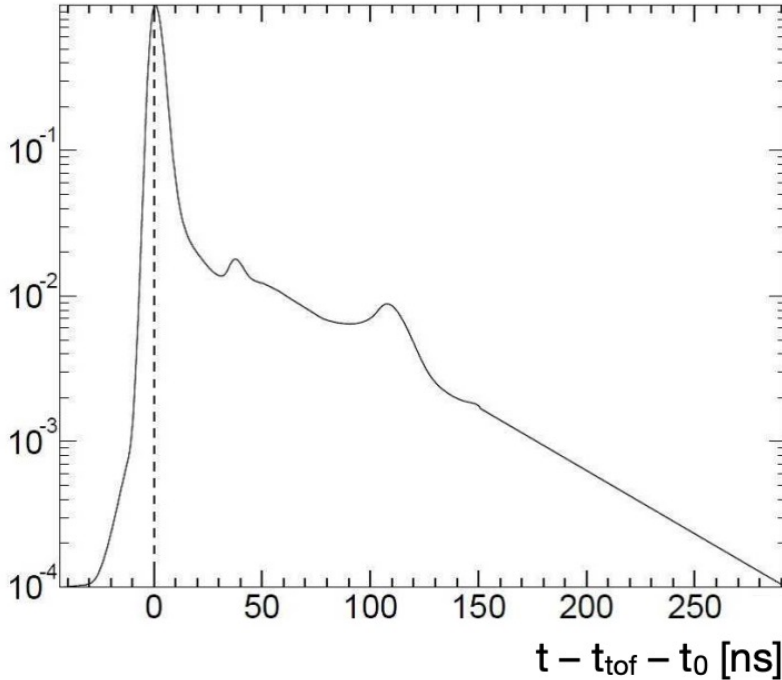


Figure 3.4: Probability density function of the residual time $t_{\text{res}, i}$ obtained from LINAC calibration. The peaks around 40 nsec and 110 nsec are the PMT late-pulses [23].

3.2.2 Direction reconstruction

The Cherenkov light ring pattern is used to reconstruct the direction. The direction is determined by maximizing the likelihood of the following function:

$$\mathcal{L}(\vec{d}) = \sum_{i=1}^{N_{20}} \log \{f(\cos \theta_i, E)\} \times \frac{\cos \theta_i}{a(\theta_i)}, \quad (3.11)$$

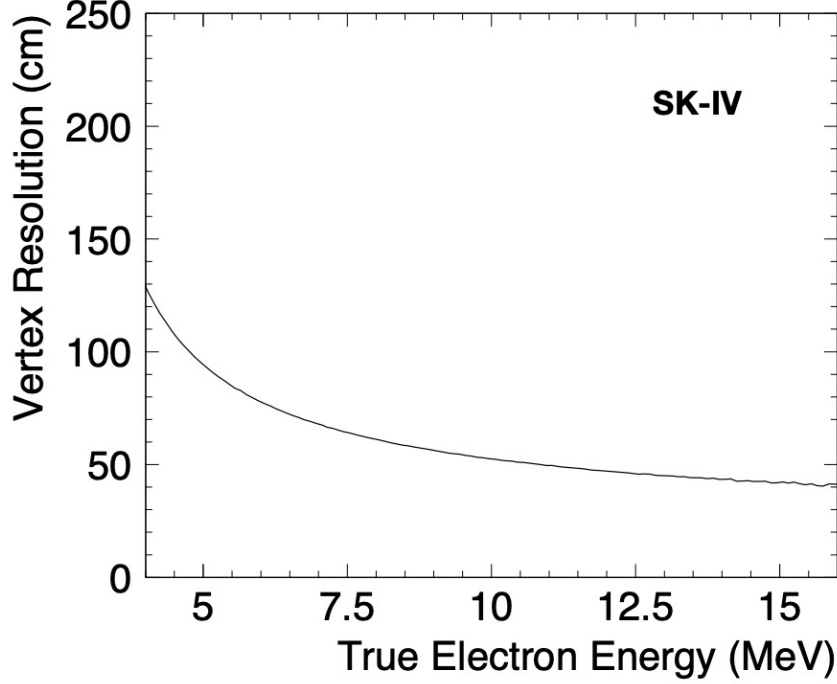


Figure 3.5: Vertex resolution as a function of true electron kinetic energy in SK-IV [23].

where \vec{d} is the traveling direction of the charged particle, and N_{20} is the number of PMTs detecting light within 20 nsec around the time of the event. The distribution of the angular likelihood function is given in Figure 3.6. $f(\cos\theta_i, E)$ is a distribution function of the angle θ_i formed between the traveling direction of the charged particle and the observed traveling direction of photons. $\cos\theta_i/a(\theta_i)$ is a correction term related to the solid angle. Here, θ_i represents the incidence angle of photons to the PMT, defined in Figure 3.7. $a(\theta_i)$ is a function of the sensitive area of PMT, which depends on the incidence angle θ_i .

3.2.3 Energy reconstruction

In the low energy region, events with the total energy below 100 MeV emit a few Cherenkov photons compared with the high energy events; hence, each PMT can only detect a single photon on average. The charge resolution for 1 p.e. in a PMT is small and can be affected by gain. The number of PMT hits is used for energy reconstruction instead of using detected charge. However, due to the attenuation effect of Cherenkov light in water and background noises originated from PMTs, the effective number of hit PMTs, N_{eff} is used. Here, N_{eff} is calculated from the number of hit PMTs within the 50 nsec time window (N_{50}) with some corrections. N_{eff} is defined as follows:

$$N_{\text{eff}} \equiv \sum_i^{N_{50}} \left[(X_i - \epsilon_{\text{tail}}^i - \epsilon_{\text{dark}}^i) \times \frac{N_{\text{all}}}{N_{\text{alive}}} \times \frac{S(0,0)}{S(\theta_i, \phi_i)} \times \exp\left(\frac{r_i}{L_{\text{eff}}^i}\right) \times \frac{1}{QE_i(1 + C \times G_i(t))} \right]. \quad (3.12)$$

The definition of each parameter used in Eq. (3.12) are as follows.

- X_i : Occupancy

When an event occurs near the edge of the fiducial volume and Cherenkov light is emitted

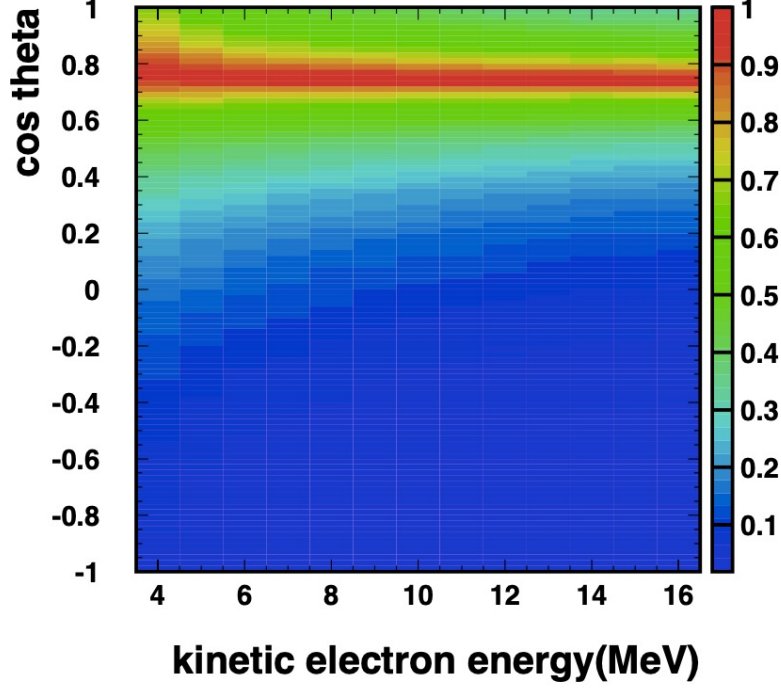


Figure 3.6: Energy dependence of the angular likelihood function used in direction reconstruction [15].

toward the ID wall, multiple photo-electrons are detected in a single PMT. Thus, the effect of the multiple photo-electrons for each hit PMT must be considered. The expected number of photo-electrons detected in a PMT is estimated by considering the occupancy correction defined as follows:

$$X_i = \begin{cases} \frac{\log \frac{1}{1-x_i}}{x_i} & (x_i < 1), \\ 3.0 & (x_i = 1), \end{cases} \quad (3.13)$$

where x_i is the fraction expressed as n_i/N_i . Here, N_i is the number of PMTs around the i -th hit PMT and n_i is the number of hit PMTs among N_i .

- ϵ_{tail}^i : Late hits
The Cherenkov light reflected by the PMTs or black sheet could enter a PMT outside the time window 50 nsec. To correct these late signals, the correction factor given below, is applied:

$$\epsilon_{\text{tail}}^i = \frac{N_{100} - N_{50} - N_{\text{alive}} \times R_{\text{dark}} \times 50 \text{ nsec}}{N_{50}}. \quad (3.14)$$

Here, N_{100} is the number of hit PMTs in the 100 nsec time window, N_{alive} is the number of operating PMTs, and R_{dark} is the average dark rate ([hits/nsec]) of all PMTs in each data run.

- ϵ_{dark}^i : Dark noise
As irrelevant events to the physics analysis, PMT detects the so-called dark noise, such as

thermalized electron events or Cherenkov light emitted by radioactive isotopes contained in PMT's glass. In the low energy region, the expected observed photoelectrons in each PMT is assumed as ~ 1 p.e./PMT; thus, the photoelectrons caused from dark noise events are non negligible and these hits must be subtracted from the total hits. The rate of dark noise fluctuates with time and must be corrected according to the operating period. The correction factor of dark noise is defined as follows:

$$\epsilon_{\text{dark}}^i = \frac{N_{\text{alive}} \times R_{\text{dark}} \times 50 \text{ nsec} \times R_{\text{dark}}^i}{N_{50} \times \sum_i \frac{R_{\text{dark}}^i}{N_{50}}}. \quad (3.15)$$

- $N_{\text{all}}/N_{\text{alive}}$: Dead PMTs
Considering defective PMTs in the ID, the correction scaling factor is applied. N_{all} is the total number of the PMTs (11,129 in SK-IV) and N_{alive} is the number of alive PMTs.
- $S(\theta_i, \phi_i)$: Photo-cathode coverage
The detection efficiency varies according to the incident angle to the PMT. Therefore, the effective photo-cathode area of the i -th PMT must be considered. $S(\theta_i, \phi_i)$ is defined as the correction function, where θ_i is the incident angle to the i -th PMT and ϕ_i is the azimuthal angle, as shown in Figure 3.7. The distribution of $S(\theta_i, \phi_i)$ is shown in Figure 3.8.
- $\exp(r_i/L_{\text{eff}}^i)$: Water transparency
Cherenkov light is attenuated by the factor $\exp(-r_i/L_{\text{eff}}^i)$ because of scattering and absorption of photons in water. Here, r_i is the distance from the reconstructed vertex to the position of i -th PMT and L_{eff}^i is the effective water transparency in pure water measured by using decay electrons from cosmic-ray muons.
- $1/(QE_i(1 + C \times G_i(t)))$: Correction of quantum efficiency
Quantum efficiency varies with each PMT; thus, the correction must be considered. Here, QE_i is the quantum efficiency for i -th PMT, $G_i(t)$ is the gain of a PMT, and C is the coefficient set as 0.226 for SK-IV phase.

Considering corrections above, N_{eff} is determined and the energy of the charged particles is reconstructed. The relationship between N_{eff} and the reconstructed energy (MeV) is given by the following equation obtained by the LINAC calibration, and the result of MC simulation.

$$E_{\text{rec}} = \begin{cases} \sum_{i=0}^5 a_i (N_{\text{eff}})^i & (N_{\text{eff}} < 234.1), \\ 30.0 + 0.131 \times (N_{\text{eff}} - 234.1) & (N_{\text{eff}} \geq 234.1), \end{cases} \quad (3.16)$$

where $a_0 = 7.59 \times 10^{-1}$, $a_1 = 1.26 \times 10^{-1}$, $a_2 = -1.99 \times 10^{-4}$, $a_3 = 2.24 \times 10^{-6}$, $a_4 = -9.38 \times 10^{-9}$ and $a_5 = 1.39 \times 10^{-11}$, respectively.

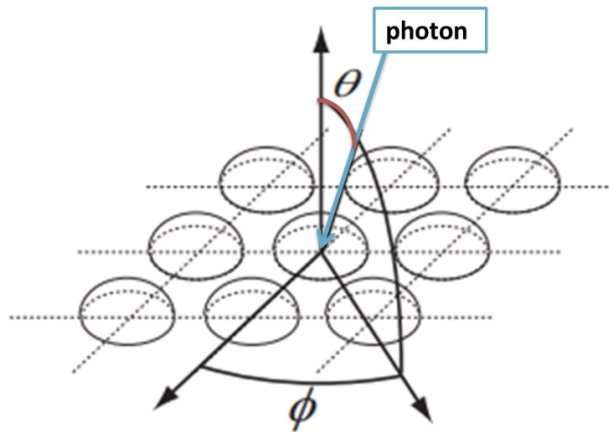


Figure 3.7: The θ_i and ϕ_i coordinates for the i -th hit PMT [15].

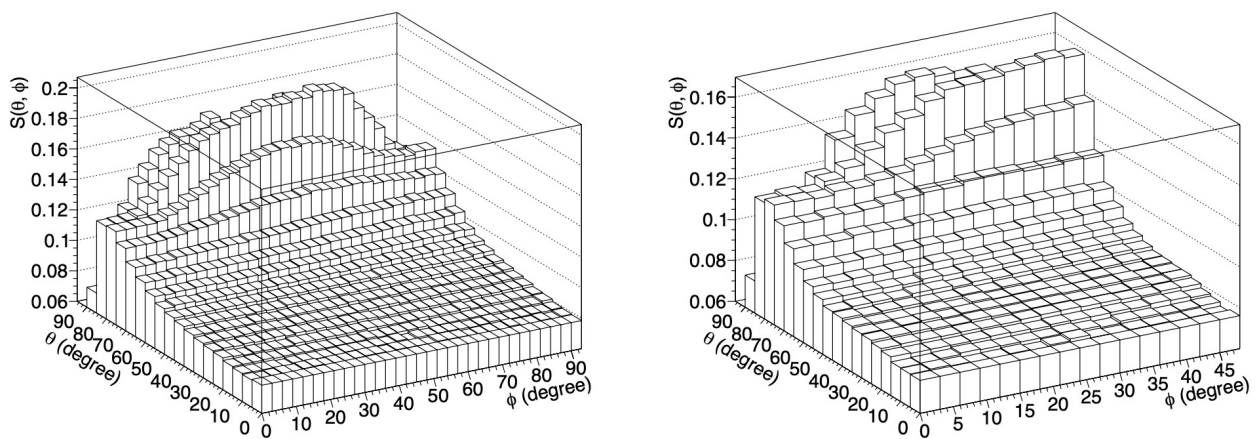


Figure 3.8: The distribution of photo-cathode coverage function $S(\theta, \phi)$: for PMTs on the barrel of the tank (left) and for PMTs on top and bottom of the tank (right) [24].

Chapter 4

Muon and decay electron simulation

To optimize the selection criteria for the data collection of muon decay events, a dedicated simulation has been developed. The process and the scheme of the detector simulation for stopping muon and decay electron is discussed as follows.

4.1 SK detector simulation

To understand the detector's response to the muon and decay electron process, the SK detector simulation based on GEANT3 tool-kit [25] was used, called SKDETSIM [16]. This simulation provides common physics reactions, including decay process, energy loss, scattering and attenuation of Cherenkov photon in water, and the electronic systems response. Thus, to optimize the selection criteria for cosmic-ray muons observed in the detector, the whole muon decay process was simulated by using this tool.

4.2 Muon simulation

To generate muons properly, the muon simulation code called MUSIC (Muon Simulation Code) was used. MUSIC is the three-dimensional simulation of the muon propagation through a slant depth X of a matter, which depends on the topographical location and the thickness of the surrounding rocks. Figure 4.1 shows the location and altitude of the surrounding mountains of the SK detector. The slant depth is calculated from the muon entering point at the mountain surface with the specific altitude and its incoming direction toward the detector, as shown in Figure 4.2. The simulation provides the average muon energy, flux, and rate by calculating the muon energy loss, angular deviation, and lateral displacement considering muon interactions with matters, including ionization, pair production, Bremsstrahlung, and inelastic scattering. The simulation has been performed for several underground experiments, including numerous testings with the comparison of simulated results against the experimental data. The energy spectrum and the muon flux at the SK depth are shown in Figure 4.3 and Figure 4.4, respectively. The average muon energy at SK is approximately 271 GeV [26]. The muon flux at SK is $1.48 \times 10^{-7} \text{ cm}^{-2} \text{ s}^{-1}$ and its rate inside the tank is 2.4 Hz [26]. As shown in Figure 4.4, the muon flux varies according to its incoming direction and low flux are reflects the thickness of the rocks. The precise calculations and complete descriptions can be found in [27], [28], [26].

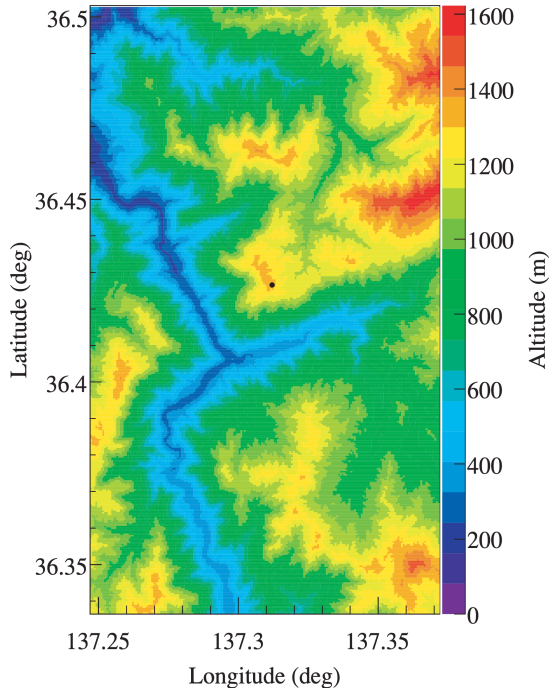


Figure 4.1: Mountain Ikenoyama topographical map in 50 m grid. The color represents the magnitude of the altitude and the black point is the location of SK detector [29].

4.2.1 Generating muons

To simulate the muon decay events considering the SK topological structure, the generated energy range must be adjusted based on muon energy on the ground level. Furthermore, the zenith dependence of injected muons reproduces the actual experimental data. The muon generation with MUSIC considering the zenith dependence at SK depth has been studied and the calculations are in good agreement with the data [31]. The procedure of muon injection is performed as the following steps:

- Energy range

The generated muon energies are adjusted to a certain range to simulate stopping muons. From Figure 4.3, the energy spectrum in $E_\mu < 20$ GeV is almost flat, equivalent to the energy range of stopping muons. Figure 4.5 (left) shows the injected muon energy distribution in the simulation. To estimate the number of stopping muons producing decay electrons in the ID in simulation, its survival probability was examined. The survival probability is calculated as the number of stopping muon events accompanying decay electrons divided by the total injected muons. Figure 4.5 (right) shows the survival probability for stopping muons and most muons with energies greater than 15 GeV are through-going muons penetrating the ID without decaying. Figure 4.6 explains that muons with a higher (lower) energy are more likely to decay in the bottom (top) side of the ID tank. Thus, the upper limitation of muon energy of 20 GeV is sufficient to only obtain stopping muons.

- Zenith angle dependence

The zenith angle distribution of generated muons in MC simulation is shown in Figure 4.7 obtained from the calculation of Ref. [31].

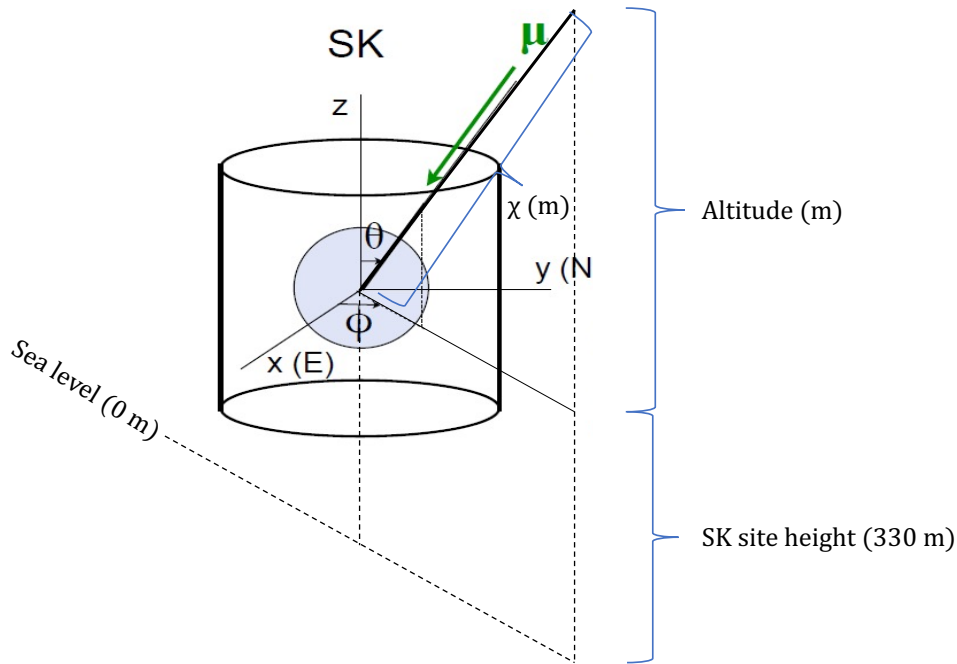


Figure 4.2: Schematic of vertical cylindrical detector of SK with coordinate system. θ is defined to be the zenith angle and ϕ is the azimuthal angle. The slant depth χ denotes the traverse distance by muon in the rock between entering position of the mountain at the specific altitude (m) to the center position of the detector located at the certain depth underground, 330 m from sea level [30].

4.3 Decay electron simulation

The stopping muon arriving at the ID in the SK tank typically decays in three bodies accompanied with electrons and two neutrinos, as shown in Eq. (1.2). The decay electron from the muon can be detected as a clear signal and an independent event, also useful in evaluating the stability of the energy scale in the energy region below 100 MeV. The muon lifetime τ_μ is explained by the V-A (vector-axial vector) theory of weak interaction and known to be approximately 2.197 μsec [32]. Figure 4.8 shows the distribution of the decay time of stopping muons in the simulation (without SK detector simulation). The lifetime of muon samples in the simulation can be measured by fitting the decay curve function to the histogram defined as:

$$N(t \sim (t + \Delta t)) = N_0 \left\{ 1 - \exp\left(-\frac{\Delta t}{\tau}\right) \right\} \exp\left(-\frac{t}{\tau}\right), \quad (4.1)$$

where N_0 is the number of observed muon events, Δt is the binning width in the histogram set as 100 nsec, and τ is the lifetime of muon. In the function, N_0 and τ are the free parameters to be fitted. The derivation of Eq. (4.1) is given in Chapter 6. The energy distribution of a decay electron generated from a muon in a rest frame can be written as follows:

$$\frac{dN}{dE} = \frac{m_\mu^2 E G^2}{4\pi^3} \left(1 - \frac{4E}{3m_\mu} \right), \quad (4.2)$$

where G is Fermi coupling constant, and m_μ is the mass of muons. According to the conservations of energy and momentum in the rest frame of a muon, the decay electron can

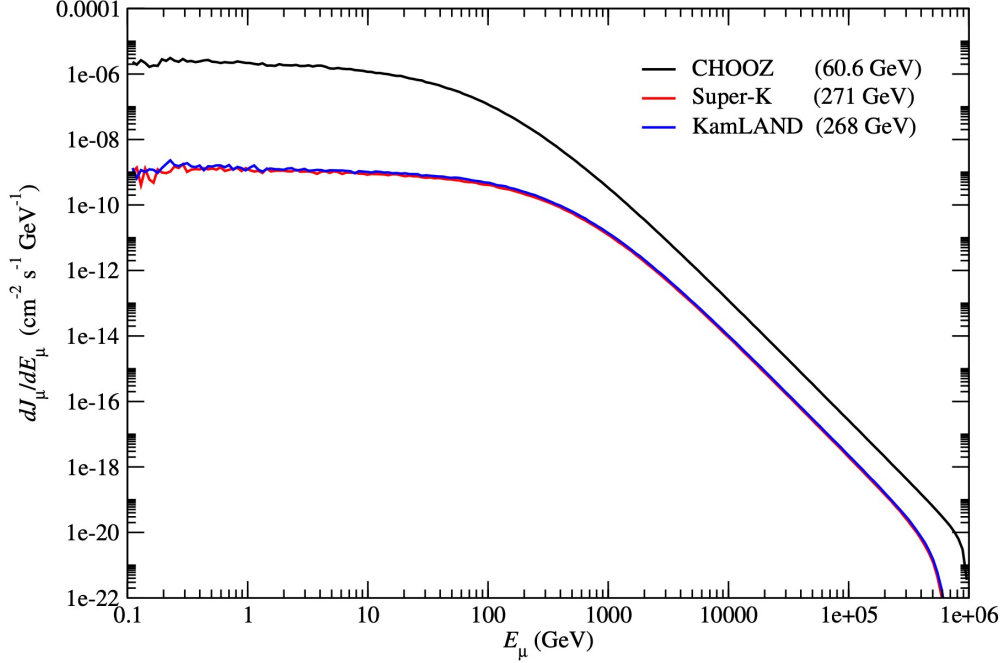


Figure 4.3: Cosmic muon energy spectrum at three underground experiment site [26]. The average muon energy at SK is $E_\mu = 271 \pm 2$ GeV. Muon energy spectrum for $E_\mu \leq 20$ GeV is almost flat.

carry $E_{\max} \simeq m_\mu/2 \sim 52$ MeV at the maximum. Figure 4.9 shows the energy distribution of decay electron from positive muon together with the reconstructed energy in the SK. The reconstructed energy distribution of decay electrons reaches up to about 70 MeV due to the detector's energy resolution. The reconstructed vertex distributions of decay electrons in the simulation are also obtained, as shown in Figure 4.10. The generated electron events are uniformly distributed in the horizontal (X and Y) and vertical (Z) coordinates respectively.

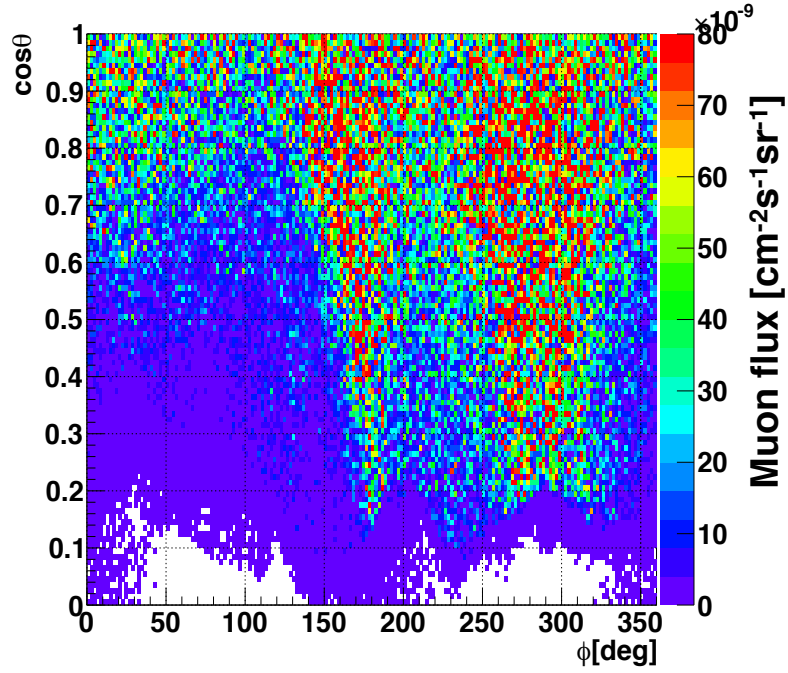


Figure 4.4: Muon flux as a function of zenith and azimuthal angle at SK depth and location calculated with MUSIC.

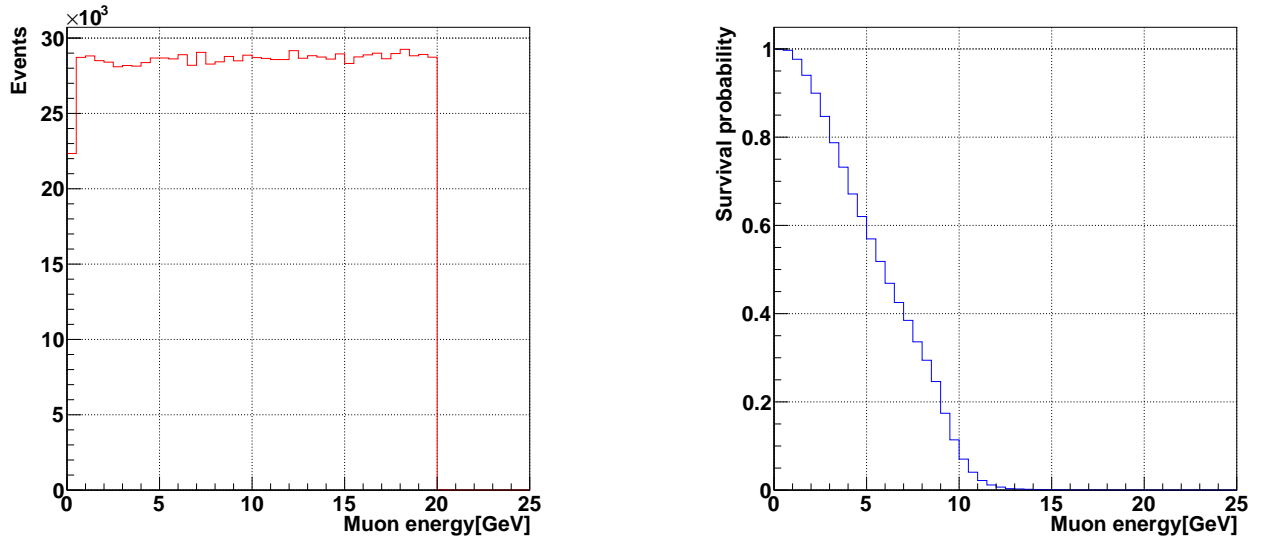


Figure 4.5: Energy distribution of injected muons (left) and its survival probability defined as the ratio of injected muons to stopping muons per 0.5 GeV bin (right). The minimum muon energy is set at least 0.1 GeV at the generated point of frame of ID to travel inward the ID tank.

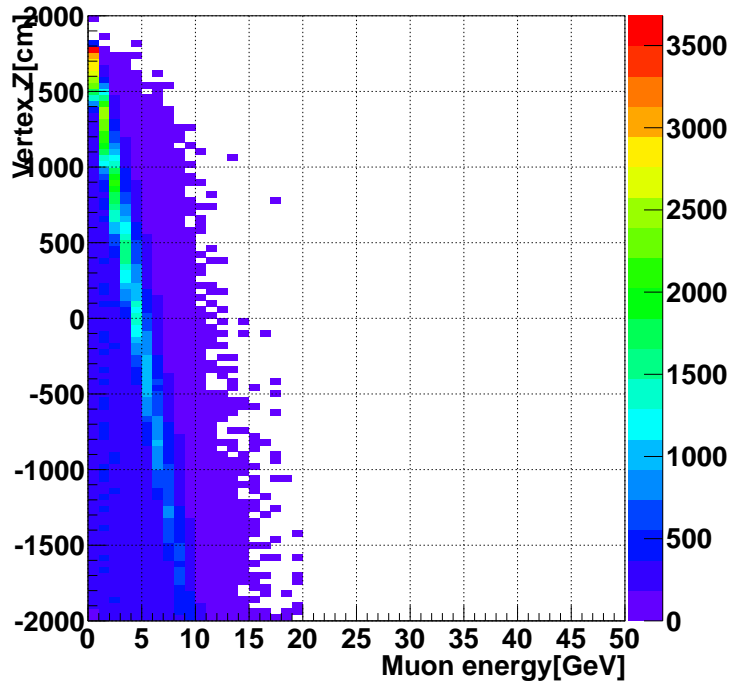


Figure 4.6: Generated muon energy and the Z coordinate of its reconstructed decay electrons in MC.

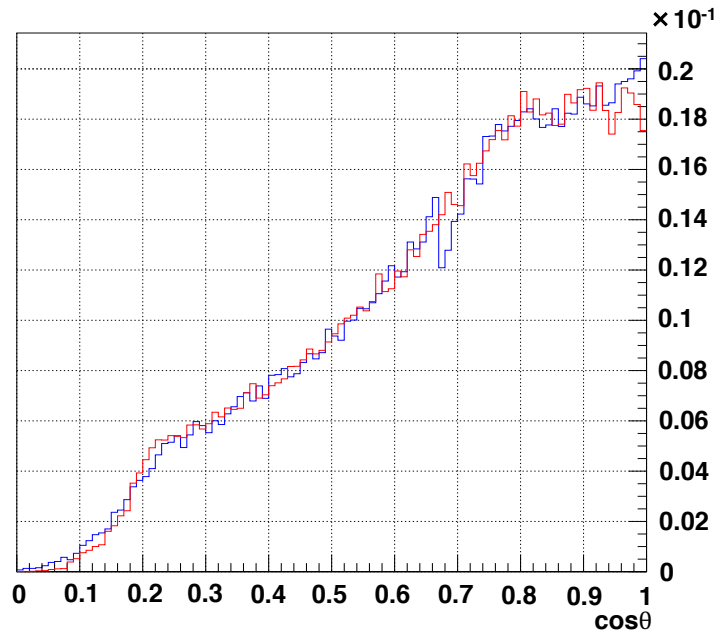


Figure 4.7: Zenith angle distribution of generated muons in MC calculated from [31]. The angular integration covers the entire hemisphere. Blue line and red line represent injected and reconstructed muons, respectively.

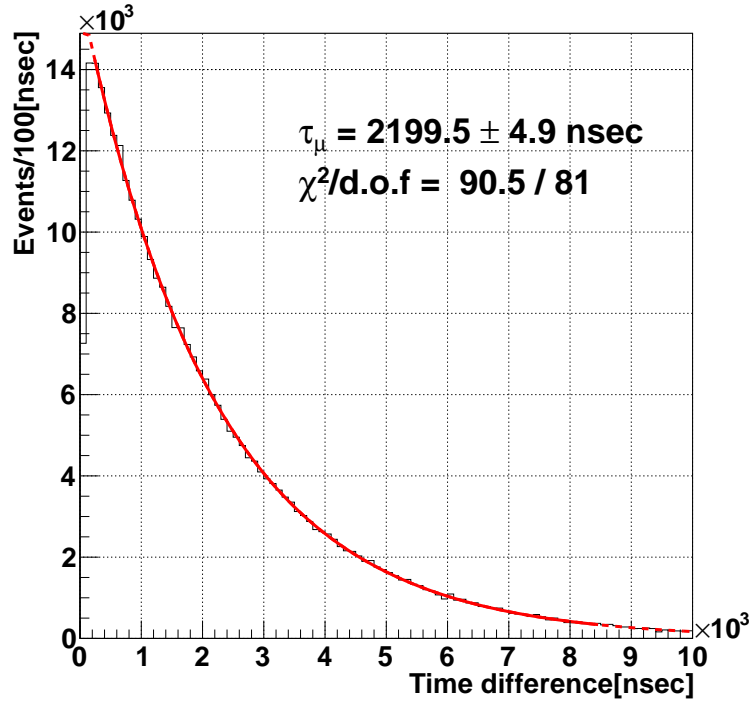


Figure 4.8: The true decay curve of stopped muons observed in MC. The fitting range is red solid line and the expected distribution after fitting the function is red dashed line.

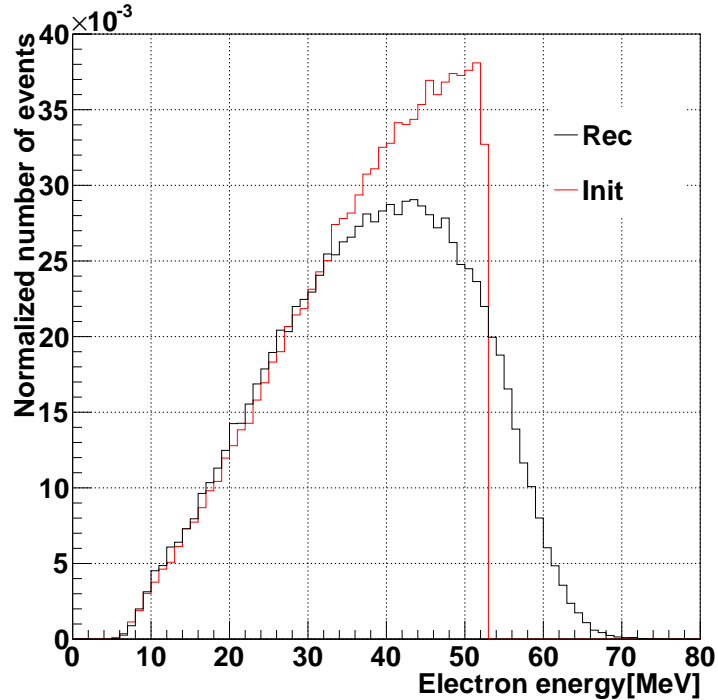
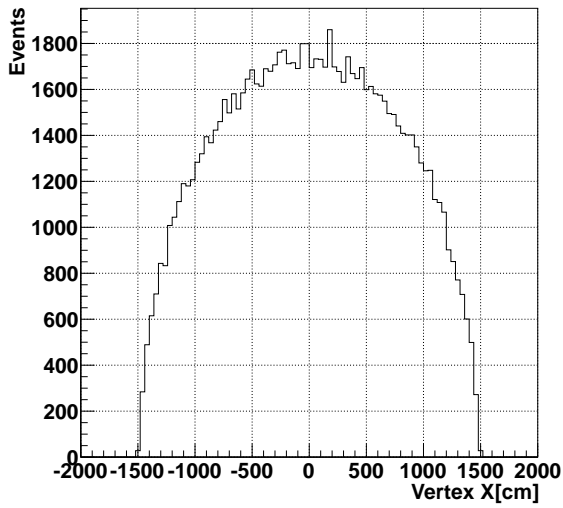
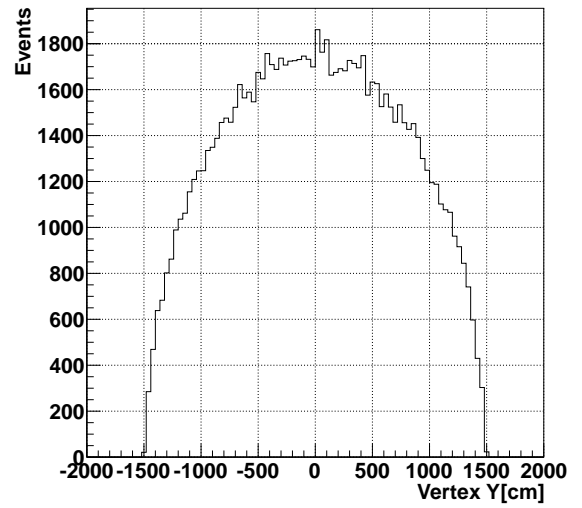


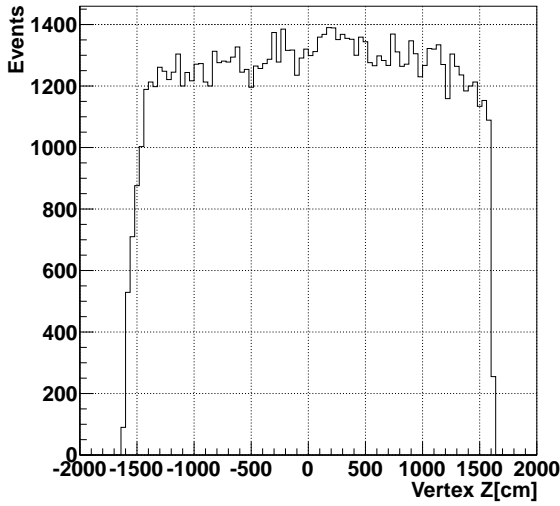
Figure 4.9: The kinetic energy distribution of decay electrons from positive stopping muons in MC. The true energy distribution is red solid line and reconstructed energy distribution is black solid line. Events are required to be positioned more than 200 cm away from the ID wall in the SK detector (Fiducial volume cut).



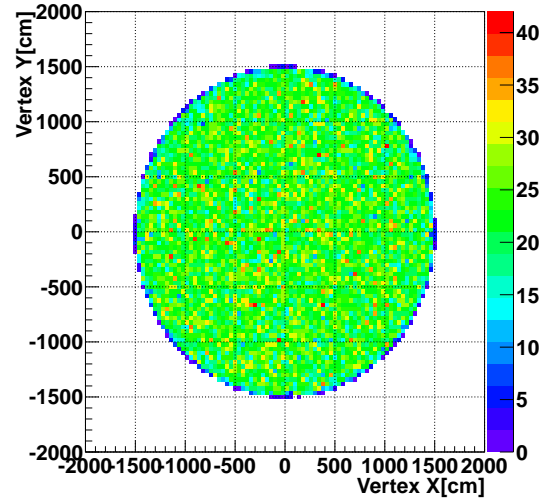
(a) X coordinate



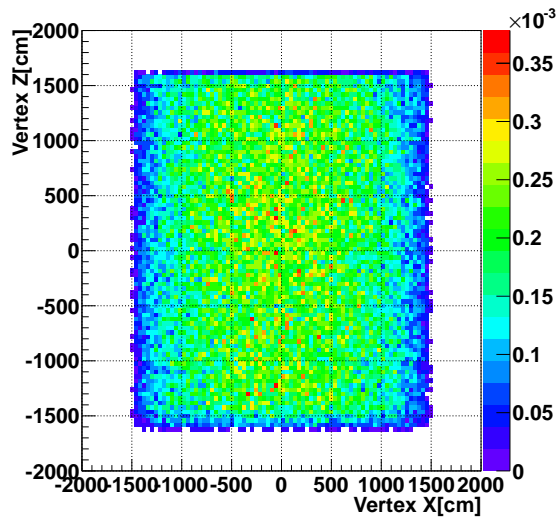
(b) Y coordinate



(c) Z coordinate



(d) X-Y coordinate



(e) X-Z coordinate

Figure 4.10: Vertex distribution of reconstructed decay electrons in MC. Here, the fiducial volume cut is applied.

Chapter 5

Event selection

Muon charge ratio is measured by using the time information obtained from stopped muons (referred to as the stopping muon) in the ID tank and its decay electron events. The measured rates of the cosmic-ray muons in the mine are around 2 Hz and approximately 3.56% [24] of their events consist of stopping muon. To distinguish the muon decay signal events from the observed data efficiently, the evaluation of the event reconstruction and optimization of selection criteria are needed. In this chapter, the selection procedure of the muon decay candidates in the data using the optimized variables driven by the MC is described. The results of the detector simulation with stopping muons and its decay electrons described in Chapter 4 are used to determine the selection criteria. Finally, the selected stopping muon and decay electron candidates obtained from the data are shown.

5.1 Data set of control samples

Since obtaining the data from April 1st 1996, the observations have been performed in several phase depending on the detector conditions. In the experimental phase from SK-I to SK-III, the analog timing module (ATM) was used for the data acquisition. In the ATM system, the charge leak of the capacity was occurring due to the large pulse height events; time information of the decay electron event was affected by the prompt muon event whose charge is large. In the SK-V phase, the calibration data is not enough compared with that of SK-IV, and the uncertainty in the energy determination is twice larger than that of the SK-IV. Therefore, for the charge ratio measurement, the data analysis was focused on SK-IV data taking period as shown in Table 2.1. The 3 month data (82.4 live time), from November 2017 to January 2018, was used as a control sample for the evaluation of the reconstruction and the determination of the selection criteria.

The topological schematic of a stopping muon and its decay electron event observed in the SK detector are shown in Figure 5.1 and Figure 5.2, respectively. The Cherenkov ring patterns of stopping muons are much clearer than those of decay electrons due to the difference in the number of emitted photons while traveling.

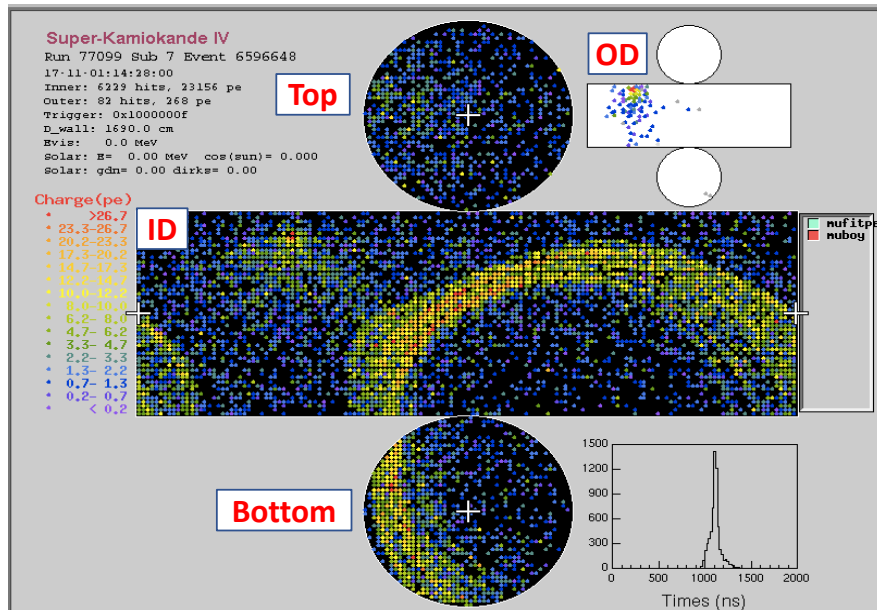


Figure 5.1: Typical ring pattern of a stopping muon in the SK detector (ID and OD). The gradation of the color in each point represents the amount of charge observed in a PMT.

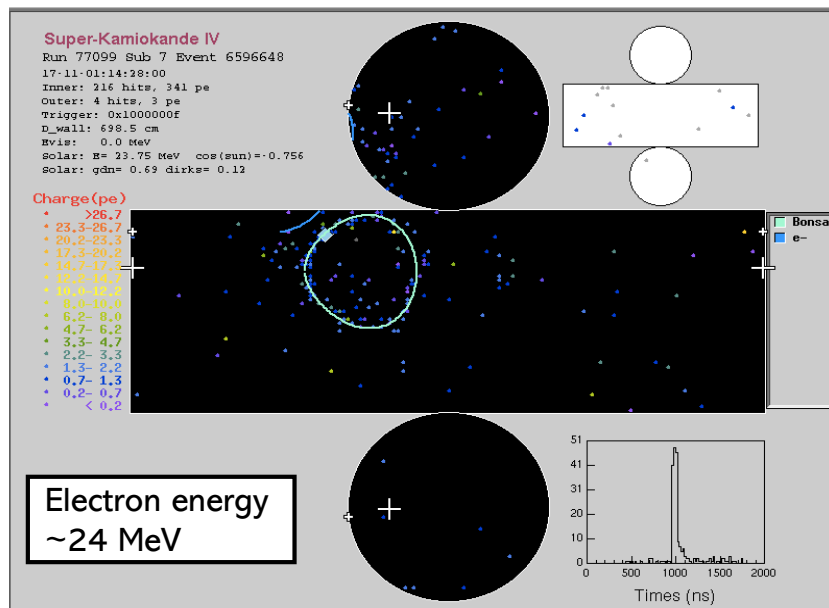


Figure 5.2: Typical ring pattern of a decay electron in the SK detector (ID). The gradation of the color in each point represents the amount of charge observed in a PMT.

5.2 Selection criteria

The data selection of stopping muons and decay electrons are processed in the order shown in the flow chart of Figure 5.3. As a first step, the stopping muons are selected among the recorded data based on their timing and topology described in Section 3.1 in Stopping muon selection. After selecting stopping muon samples, the decay electrons are searched within several microseconds after the entering time of stopping muons in Decay electron selection. Decay electron candidates are selected based on its vertex, energy, and fitting quality by evaluating

with the variables obtained in the MC simulation. The selection criteria for each section are discussed as below.

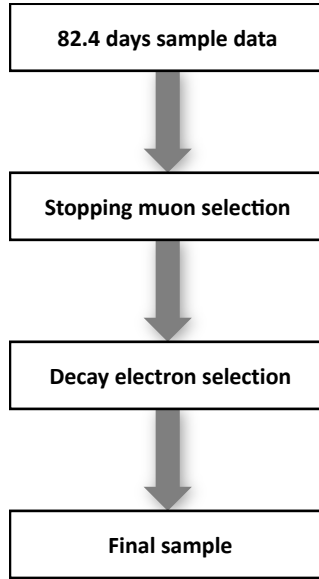


Figure 5.3: The flow chart of μ -e decay event selection for SK-IV data analysis.

5.2.1 Selection for stopping muon

Among the cosmic-ray muon events observed in the data, a Single topping muons are used in this analysis accompanied by the with decay electrons. To select the stopping muon candidates, several selection criteria are applied to the raw data as follows:

- **Muon status**

Muon events observed in the SK tank are classified in six categories by using a muon fitter according to its track property, as described in Chapter 3: (0) No-fit, (2) Single through-going muon, (3) Stopping muon, (4) Multiple muon-1, (5) Multiple muon-2, (6) Corner-clipping muons. In this analysis, a muon event categorized as (3) Stopping muon are considered.

- **Total Q cut**

In the low energy region, background contamination originated from charged particles or γ rays emitted from the radioactive sources existing in the SK detector and surrounding rocks could affect the data analysis [17]. Figure 5.4 shows the distribution of total deposit charge¹ of stopping muon candidates in the data. To reduce irrelevant background events from the data, events with the total charge ≤ 1500 are rejected.

- **Direction cut**

Almost all stopping muon events observed at the SK detector are cosmic-ray muons generated directly in the atmosphere. However, there is a possibility that upward-going muon induced from neutrino interactions can be detected and regarded as background events of the cosmic-ray muons [33]. Since an incidence angle of cosmic-ray muons is downward toward the SK detector, upward-going muons can be distinguished from downward-going

¹Total sum of p.e. charge in an event observed by ID PMTs.

muons by applying the direction cut. The incidence direction of stopping muons is calculated from its track by using a muon fitter. Figure 5.5 shows the zenith angle distribution of stopping muons, before and after the direction cut. From the zenith angle distribution of cosmic-ray muons as shown in Figure 4.7, events satisfy the upward-going direction region, $\cos \theta < 0$ are rejected in this analysis.

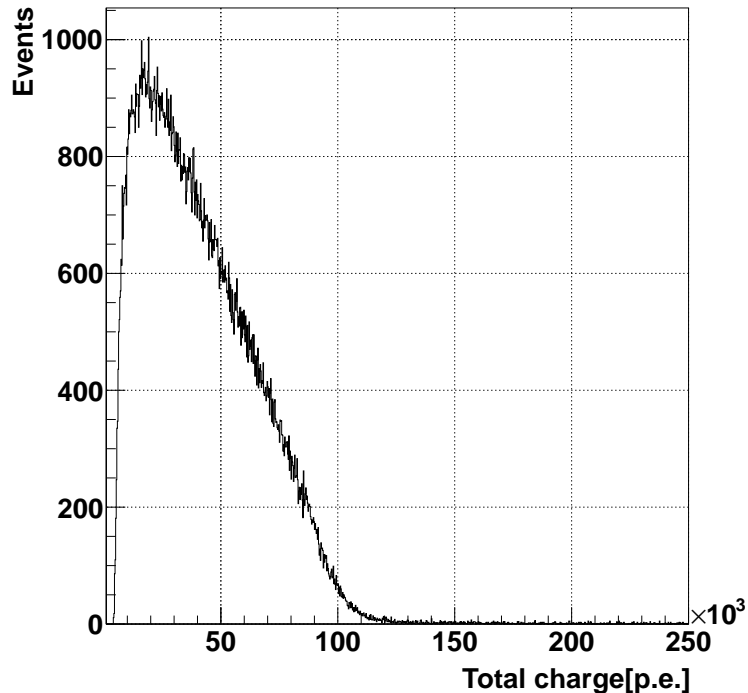


Figure 5.4: Total charge of stopping muons in the control sample.

5.2.2 Selection for decay electron

From the information of prompt muon events, decay electron candidates are selected by applying several reduction cuts as follows:

- **Fiducial volume cut**

Low energy events originated from external γ -rays from the radiation source in the structure of the SK detector and surrounding rocks are the major backgrounds for decay electron analysis (~ 10 MeV). These events can be reduced by requiring the vertex position of decay electron 200 cm inwards from the ID wall. Figure 5.6 shows the reconstructed vertex of decay electrons in X-Y, and X-Z coordinates. Events reconstructed in the range, $R = \sqrt{X^2 + Y^2} < 1490$ cm and, $|Z| < 1610$ cm in the cylindrical coordinate system are used in the analysis.

- **Ovaq cut**

To assess the qualities of the vertex reconstruction, *Goodness* is defined. The parameter *Goodness* is defined as:

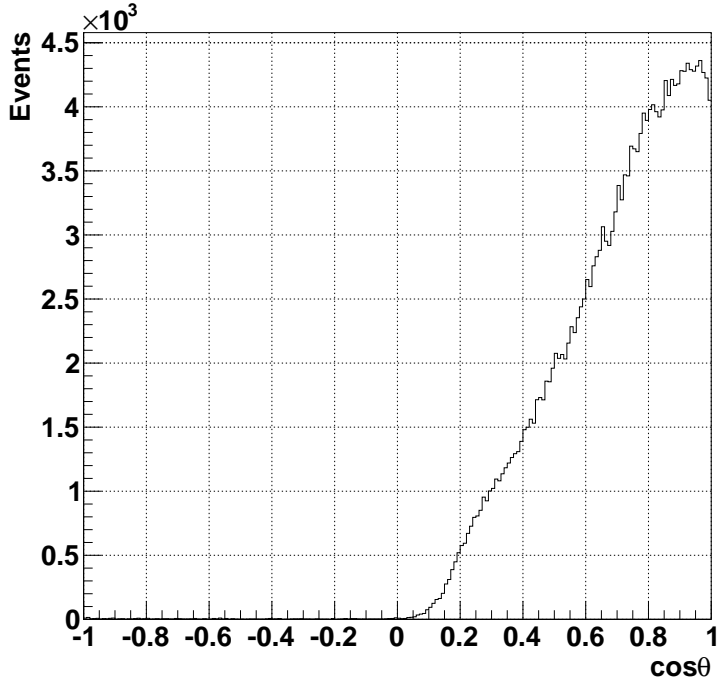


Figure 5.5: Zenith angle distribution of stopping muons in the control sample. θ is defined as the zenith angle, where $\cos \theta = +1$ correspond to vertically downward direction and $\cos \theta = -1$ to vertically upward direction. Almost all stopping muons are coming from the top side of the SK tank toward the bottom.

$$Goodness = \frac{\sum_i \exp \left[- \left(\frac{t_i - t_{\text{tof},i} - t_0}{\sqrt{2}\omega} \right)^2 \right] \exp \left[- \left(\frac{t_i - t_{\text{tof},i} - t_0}{\sqrt{2}\sigma} \right)^2 \right]}{\exp \left[- \left(\frac{t_i - t_{\text{tof},i} - t_0}{\sqrt{2}\omega} \right)^2 \right]}, \quad (5.1)$$

where ω is the resolution of the $t_i - t_{\text{tof},i}$ distribution and σ is the timing resolution of PMT. The parameter *Goodness* takes a value from 0 to 1, with 1 representing the best quality case. The parameter *DirKS* is defined to evaluate the uniformity of the hit PMTs from its direction. The definition is:

$$DirKS = \frac{\max \{ \angle_{\text{uniform}}(i) - \angle_{\text{data}}(i) \} - \min \{ \angle_{\text{uniform}}(i) - \angle_{\text{data}}(i) \}}{2\pi}, \quad (5.2)$$

where $\angle_{\text{uniform}}(i)$ is the azimuthal angle of the i -th hit PMT assuming that the PMT hits are uniformly distributed along the Cherenkov ring and $\angle_{\text{data}}(i)$ is that of the actual hit PMT. *DirKS* takes a value in the range 0 to 1, and 0 represents the best quality case. Using the two parameters, *Goodness* and *DirKS* above, the parameter *Ovaq* (One dimensional variable of Vertex and Angular reconstruction Quality) indicating the quality of event reconstruction, can be defined as follows:

$$Ovaq \equiv Goodness^2 - DirKS^2. \quad (5.3)$$

Here, *Ovaq* takes a value from -1 to 1 , and 1 represents the best quality case. According to the distribution of *Ovaq* on MC shown together with that of data in Figure 5.7, events whose *Ovaq* is less than 0.3 are regarded as mis-reconstructed and are rejected in this analysis.

- **Electron energy and the number of hit PMTs within 50 nsec window (N_{50}) cuts**
The energy distributions of decay electrons from stopping muons in both data and MC are shown in Figure 5.8. In the low energy region, γ -rays from radioactive sources, including Rn and μ^- nucleon captured by ^{16}O nuclei are contained as background events. The excited ^{16}N nuclei is also produced via the following process:



The maximum energy of de-excitation γ -rays from excited ^{16}N nuclei is 10.8 MeV. The small peak around 6 MeV in Figure 5.8 is due to the γ -rays produced by excited ^{16}N . To eliminate low energy events with the background contamination, $E_{\text{electron}} < 8$ MeV is applied for the rejection. As the same analogy, events with $N_{50} < 50$ (~ 8 MeV) are rejected in this analysis.

- **Distance cut**

The distribution of distance between the stopped position of stopping muons estimated by the track length from their entrance position in the ID tank using the Muboy fitter and vertex of the decay electrons by using BONSAI fitter peaks around 80 cm gradually decreases as the distance becomes larger as shown in Figure 5.9. Due to the uncertainty of the stopping point of muons and vertex resolution of decay electrons, the distance is widely spread apart from the actual value from 0 cm. Events in the long distance region are expected to be mis-reconstructed or background events. Hence, the appropriate cut for the distance was determined by examining the detecting efficiency as a function of distance cut. According to the result in Figure 5.10, the distance cut, with *distance* < 300 cm has the detecting efficiency of 98% and seems to be a suitable to select sufficient signal events for the data analysis.

- **Time difference cut**

The time difference is obtained by measuring the timing information between prompt muon events and delayed signal events, expected as the decay electrons. Prompt muon events fire the LE trigger due to its numerous hit PMTs and save the sub events between in the time region of $[-5, +35]$ μsec as explained in Section 2.5.2. Since the muon mean lifetime is about 2.197 μsec (in vacuum), the time window of LE trigger is wide enough to save signal from decay electrons. Decay electron candidates expected to exist in the time region $[-5, +35]$ μsec , are searched by performing sub-trigger search (offline) using the method like SLE trigger. The sub event with 1.3 μsec time window is stored when the number of hit PMTs within 200 nsec (N_{200}) is larger than 20 . Figure 5.11 shows a conceptual diagram of PMT hit timings from the prompt stopping muon and the decay electron. The two peaks occurring from the parent muon and its decay electron are distributed in less than 1.3 μsec . Since muon and decay electron are successive events, decay electron can occur before the mean lifetime of muon, 2.2 μsec from the arrival time of stopping muon. Figure 5.12 shows the signal of the muon decay event with a time difference between the muon and the decay electron less than 1.3 μsec . In Figure 5.12, the signal from a decay electron is apart from muon signal about 800 nsec. A decay

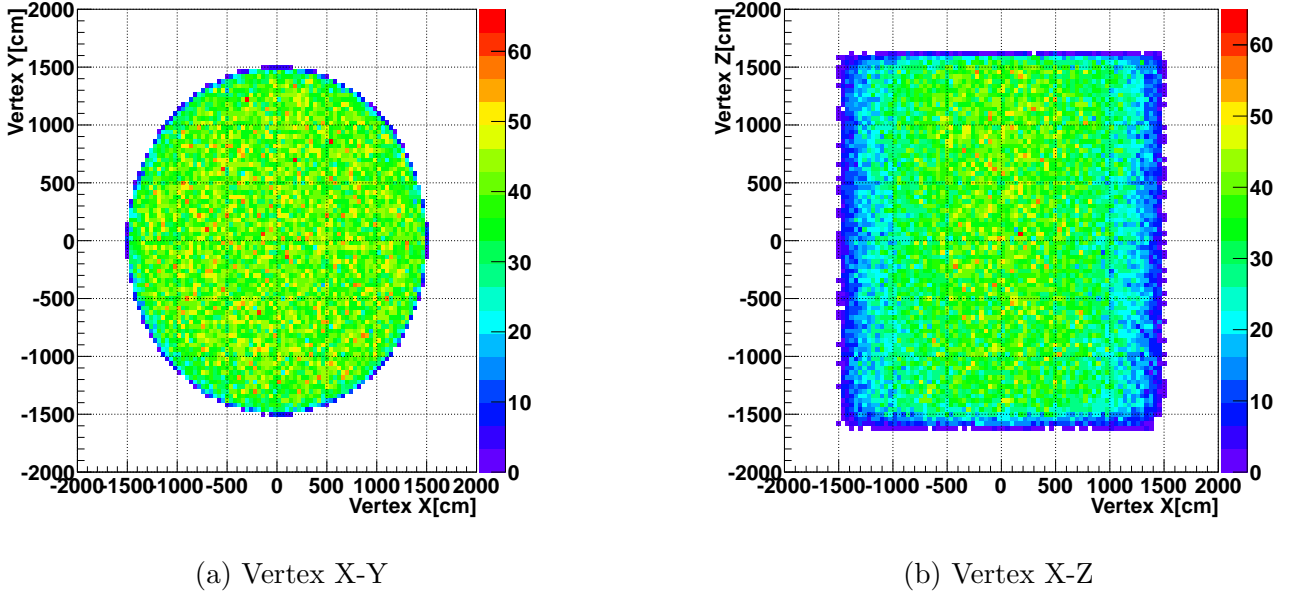


Figure 5.6: Vertex distribution of reconstructed decay electrons in the data. Muon reduction cuts, fiducial volume cut, and time difference cut for decay electrons are applied.

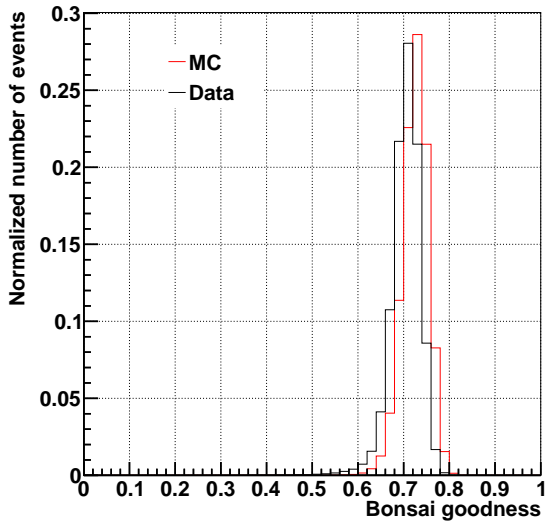
electron event with a shorter time difference can mis-identify hit PMTs from the muon longer tail hits as a decay electron. These contaminated hit PMTs originated from the parent muons are difficult to distinguish from that of an electron signal. A part of the signal tail of a parent muon can be integrated in the time window of sub event and the event reconstruction can be affected. However, as shown in Figure 5.12, the decay electrons with a longer time difference are distributed according to the Michel decay spectrum, in the shorter time region, and their events are mostly distributed below 20 MeV. Thus, to avoid including mis-reconstruction events, the sub events occurring between $1.3 \mu\text{sec} < t < 30 \mu\text{sec}$ from a prompt event are only selected.

5.3 Selected samples

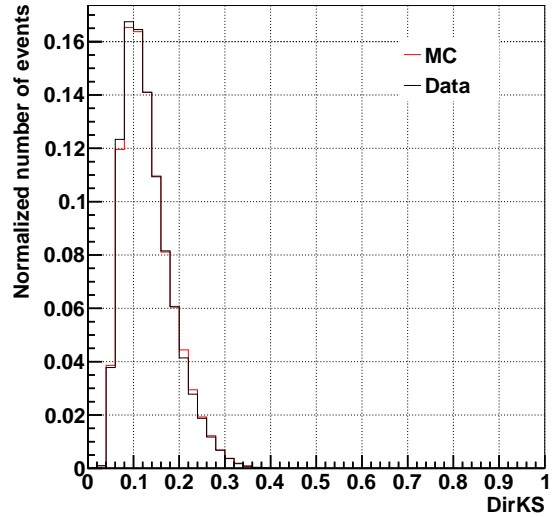
5.3.1 Stopping muon candidates

The distribution of selected muon samples in the control samples are evaluated by scanning the distribution after applying the selection cuts in the previous selection to confirm the data quality. Figure 5.13 shows the reconstructed 2D vertex distribution of stopping muons in X-Y and R-Z coordinates, where X and Y correspond to the horizontal plane ($R = \sqrt{X^2 + Y^2}$) and Z corresponds to the vertical direction, respectively. According to Figure 5.13, most muons enter from the top of the tank from south, with a relatively shorter slant depth². The corresponding angular distribution for stopping muons is given in Figure 5.14 and Figure 5.15. Muon angular distribution depends on the topography around Mount Ikenoyama and indicates that the intensity of stopping muons depends on muon travel length in the surrounding rocks. The GOF parameter, representing the reconstruction quality of muon event, as described in Section 3.1 is distributed as shown in Figure 5.16. Comparing the distribution of the goodness of stopping

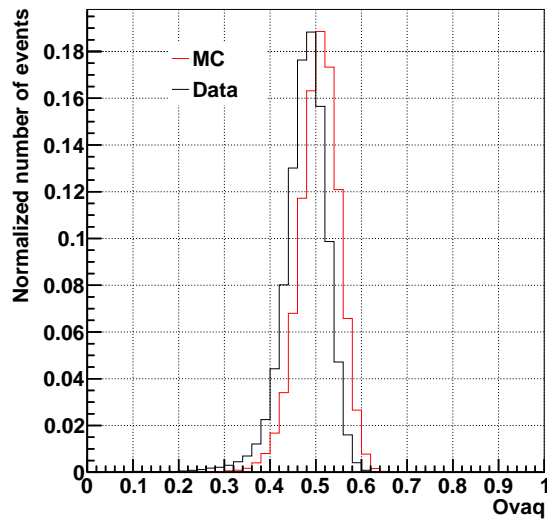
²The altitude of the mountain is about 1,000 m, however, the slant depth can be 650 m which depends on the incoming direction of the muon.



(a) Goodness



(b) DirKS



(c) Ovaq

Figure 5.7: Distributions of the quality of fitting parameters used for decay electrons in the data (black line) and MC (red line). Muon reduction cuts, fiducial volume cut, and time difference cut are applied.

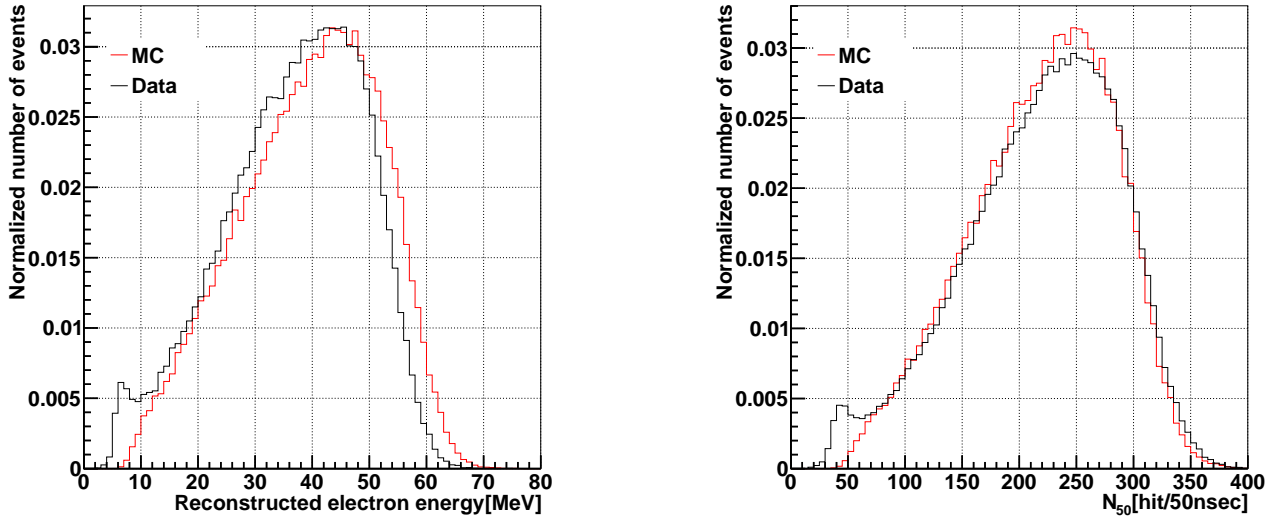


Figure 5.8: Distributions of reconstructed energy (left) and N_{50} (right) of decay electrons in the data (black line) and MC (red line). Muon reduction cuts, fiducial volume cut, and time difference cut are applied.

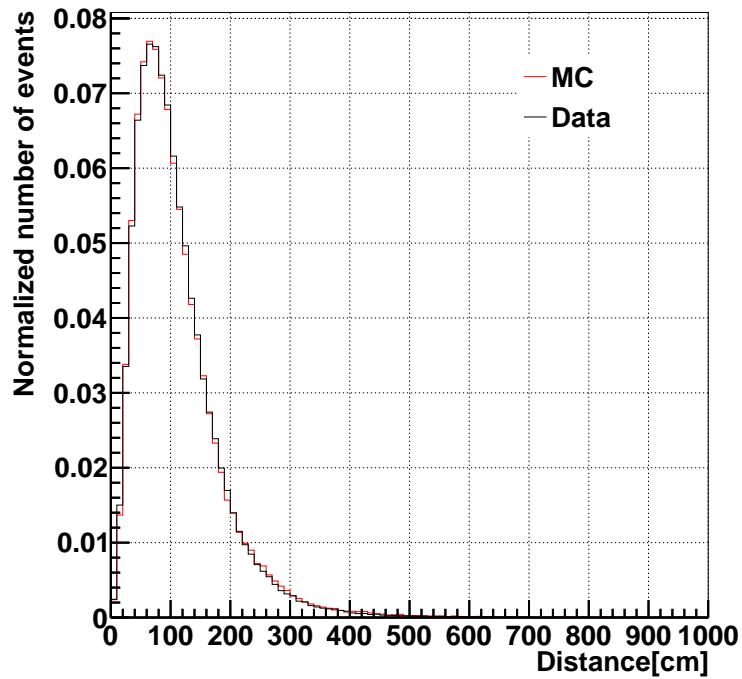


Figure 5.9: Distribution of distance between reconstructed stopped position of stopping muon and vertex of decay electrons in data (black line) and MC (red line). Muon and decay electron reduction cuts are applied.

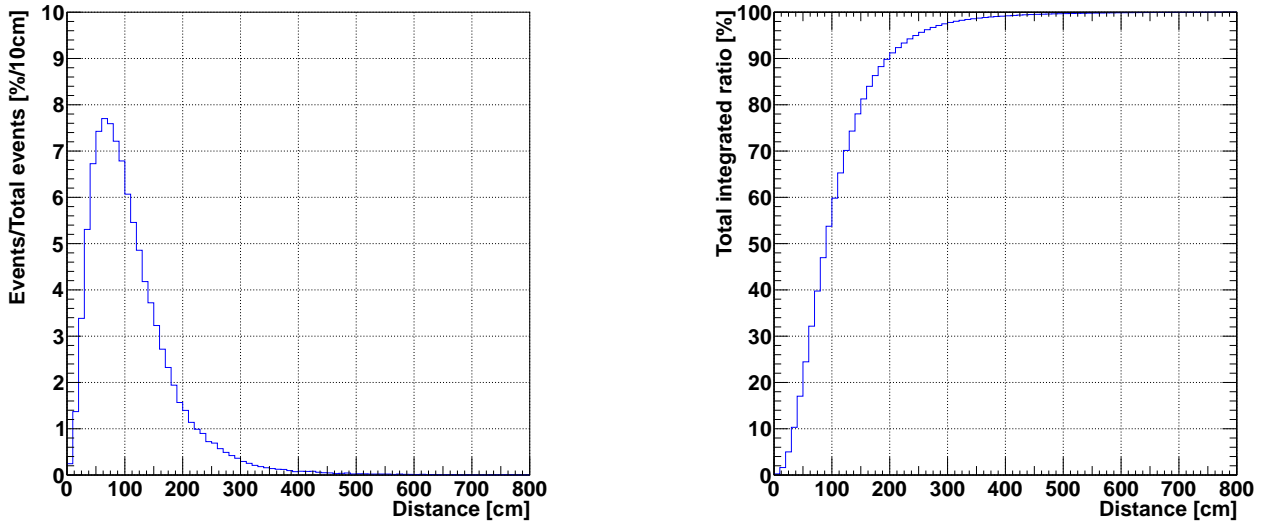


Figure 5.10: The fraction of muon events per 10 cm distance bin to the total events (left) and its detecting efficiency (right) as function of distance in MC. The reduction cuts described in above for both muons and decay electrons are applied.

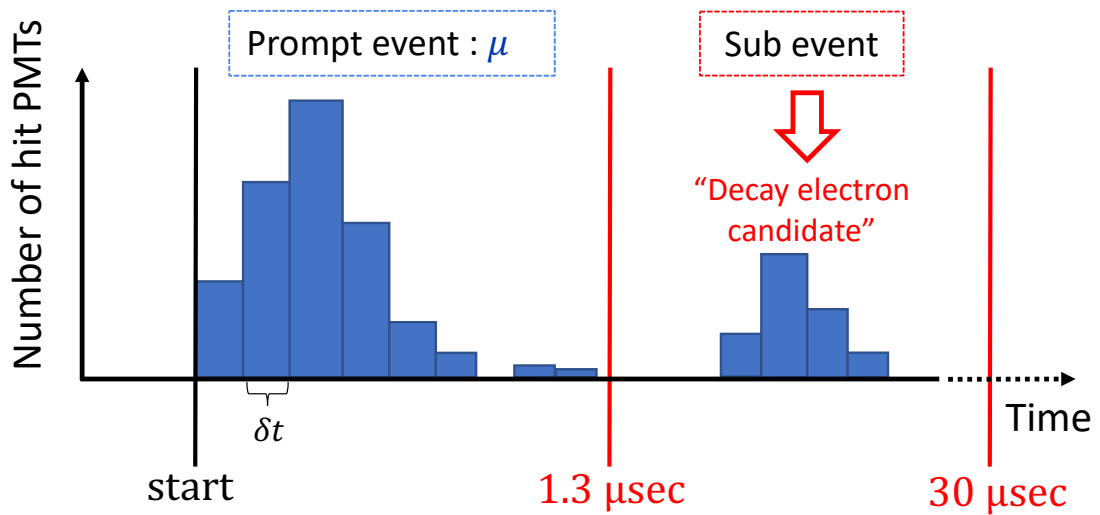


Figure 5.11: Schematic view of the prompt signal and delayed signal in the time window.

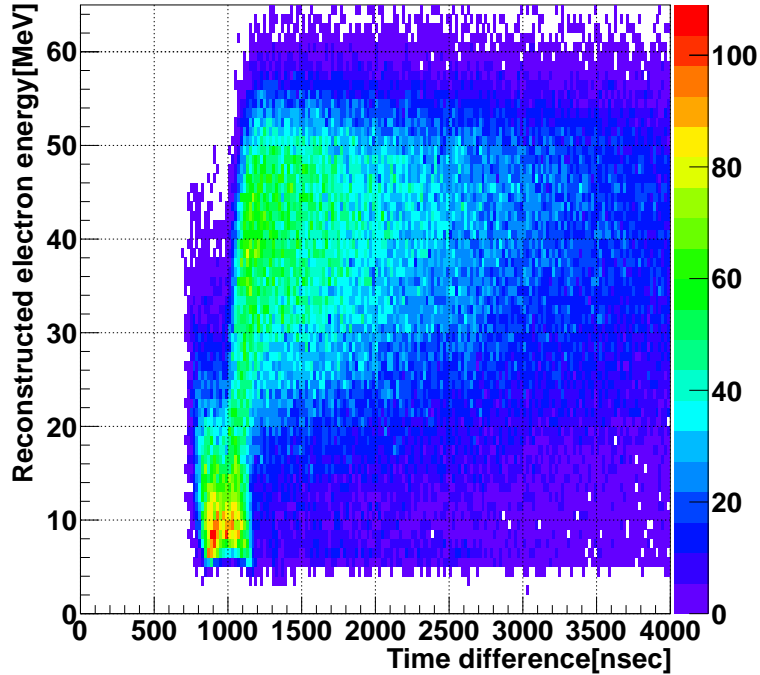
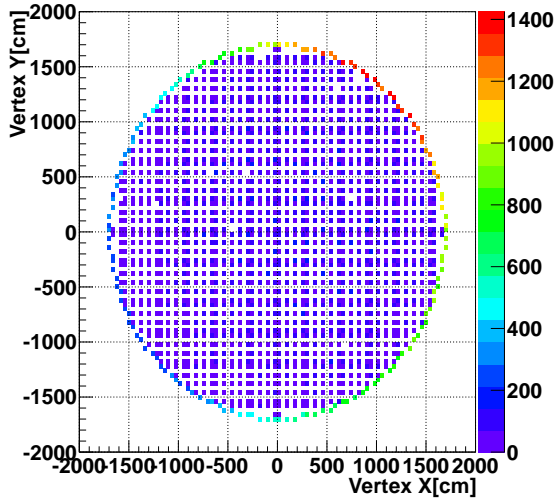


Figure 5.12: Distribution of decay electron energy and muon lifetime in the data after applying fiducial volume cut.

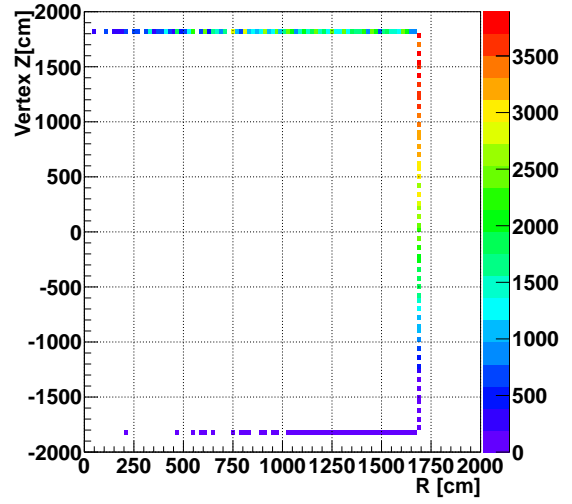
muons between data and MC, events peak at 0.6 and are in good agreement with each other. Figure 5.17 shows the distribution of muon track lengths in the ID tank for stopping muon events. Since the incidence direction of the muon events with the energy range from 100 MeV to 20 GeV has the a zenith angle dependence; muons with the small (large) energy are more likely to stop (travel) closer (further) to the enter position of the tank. The relationship between the track length and total deposit charge for a stopping muon is shown in Figure 5.18. The total deposit charge increases in proportion to its track length and found as approximately 25 p.e. per unit cm corresponding to the muon energy deposit per cm, ~ 2 MeV/cm obtained from Bethe-Bloch formula.

5.3.2 Decay electron candidates

The data quality of selected decay electron events after applying the selection cuts are examined by checking the distribution of reconstructed decay electron events for whether the bias exists in the data or not. The reconstructed vertex position of decay electrons in X, Y and Z coordinates are shown in Figure 5.19. The selected events distribute uniformly in the horizontal coordinate (X and Y), while, in the vertical coordinate (Z), events are rather distributed upper side ($Z > 0$) of the tank. This is because most stopping muon events arrive from the top of the tank and lose their energies while propagating in the water and finally decay before reaching the lower side ($Z < 0$) of the tank. The observed decay curve of the time difference is shown in Figure 5.20. The lifetime of selected muon decay samples can be measured by fitting the decay curve function Eq. (4.1) to the histogram. Applying the fitting function Eq. (4.1) to the histogram in the range of 1300 nsec to 8500 nsec, the τ is finally obtained as 2048.1 ± 6.5 nsec. The lifetime obtained from the selected samples is slightly shorter than that obtained from Figure 4.8 due to the contribution from the shorter lifetime of negative muons.



(a) X-Y



(b) R-Z

Figure 5.13: Enter position of stopping muon in the SK tank for X-Y (left) and R-Z (right) coordinates in the data.

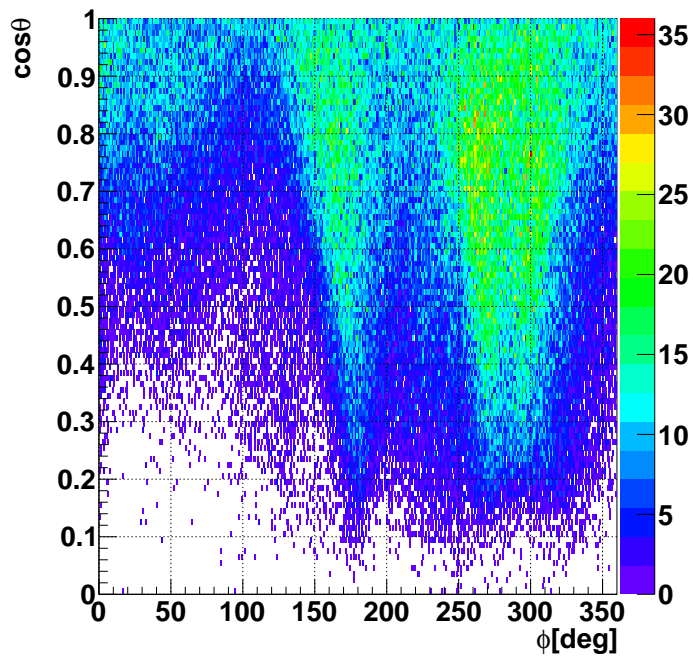


Figure 5.14: Intensity of stopping muons arriving at SK detector as a function of azimuthal and zenith angle in the data. $\phi = 0^\circ$ and $\phi = 90^\circ$ corresponds to east and north, respectively.

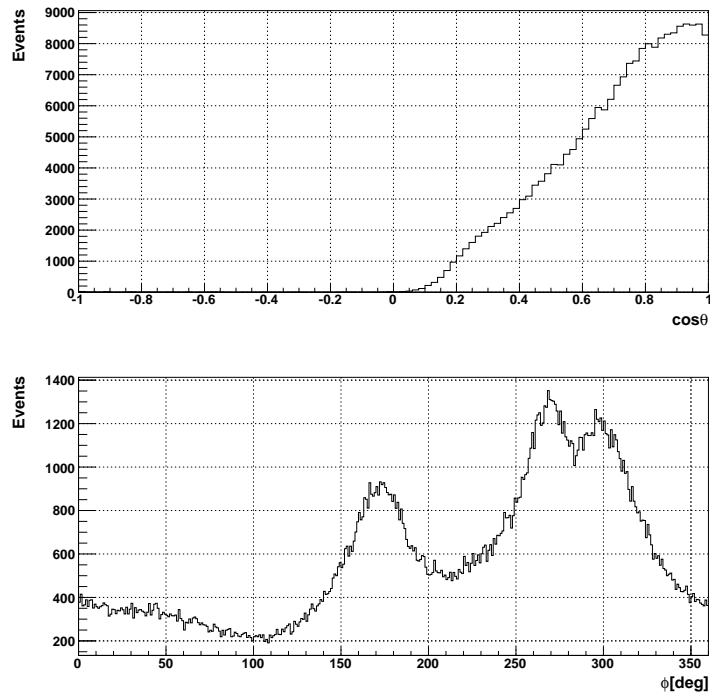


Figure 5.15: Azimuthal and zenith angle distribution of stopping muons in the data.

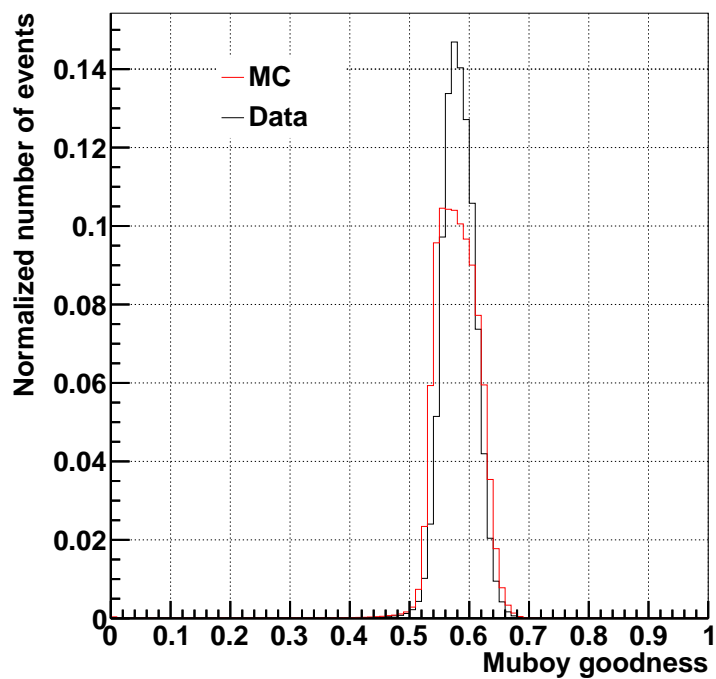


Figure 5.16: Distribution of Muboy goodness for stopping muon in the data (black line) and MC (red line). Almost all muon events are distributed around 0.6.

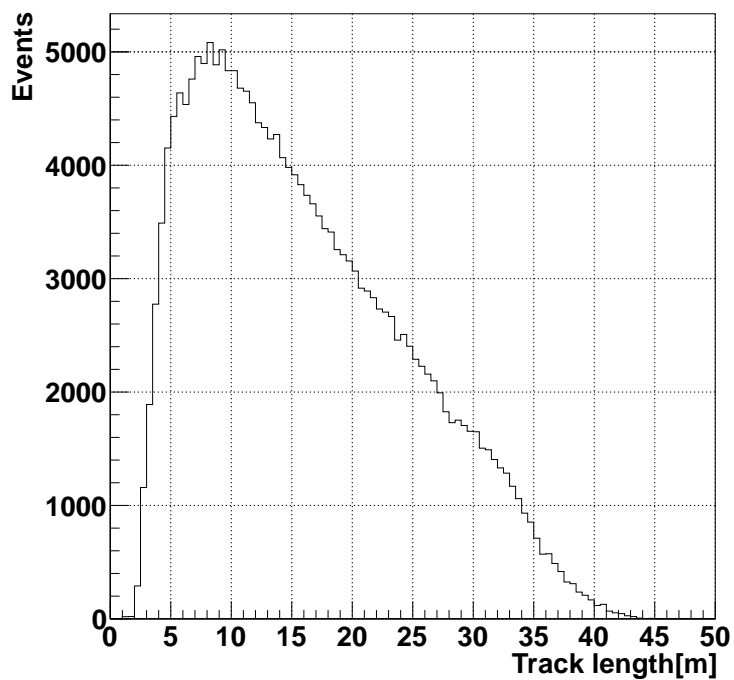


Figure 5.17: Distribution of track length for stopping muons in the data.

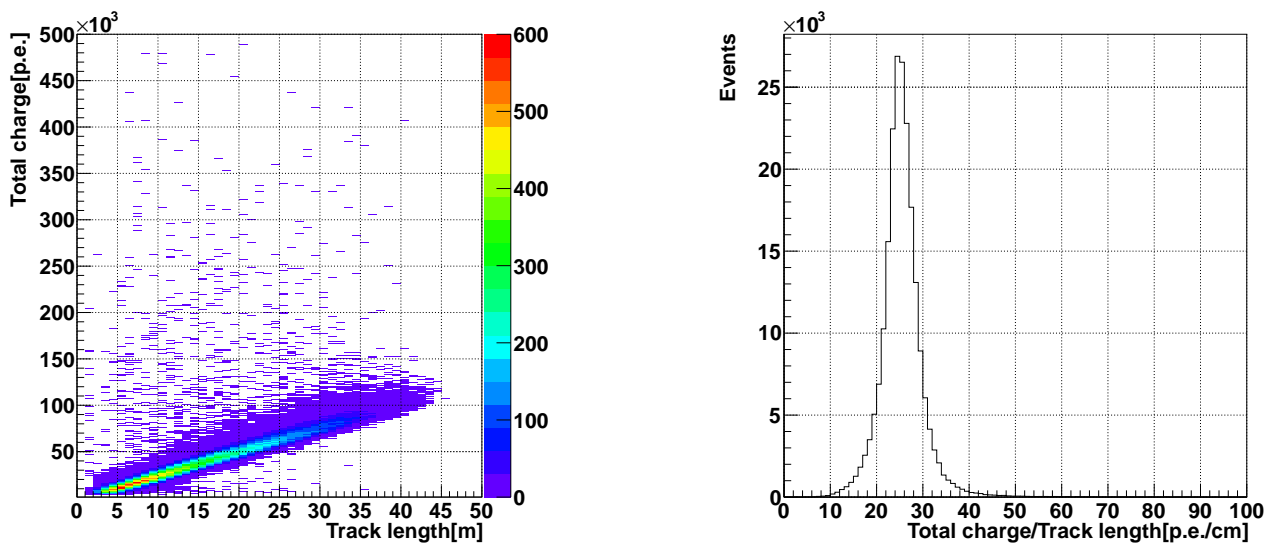
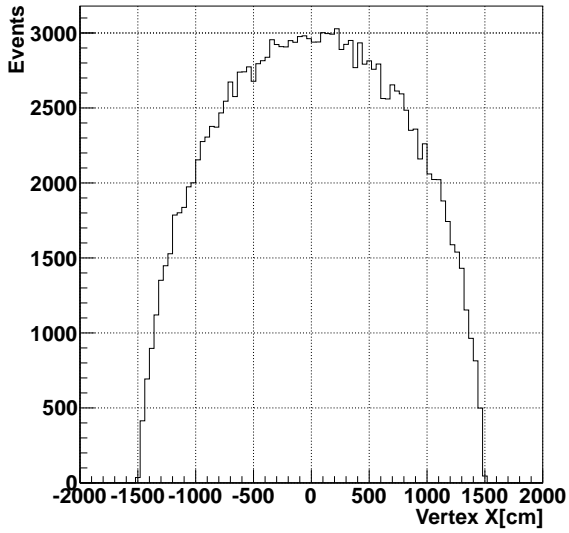
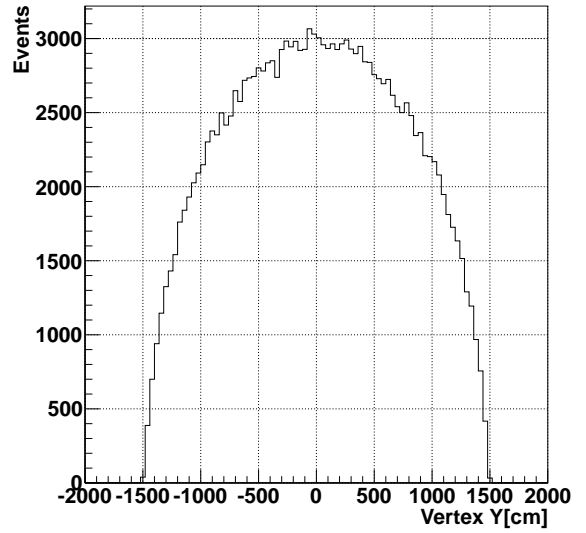


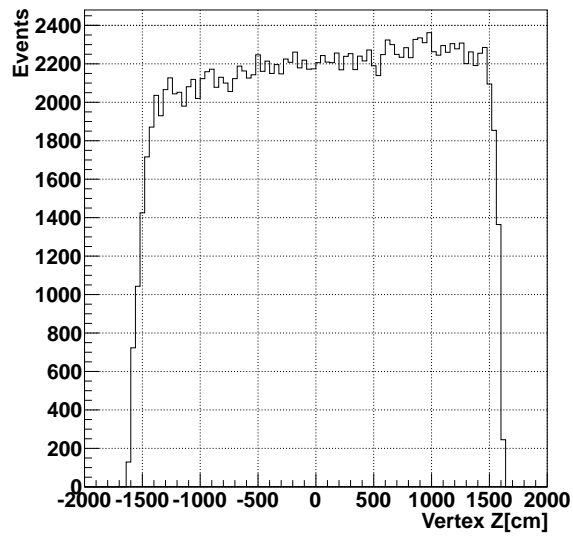
Figure 5.18: The relationship between track length and total deposit charge (left) and the distribution of total charge divided by track length (right) for stopping muons in the data. The constant of proportionality is approximately 25 p.e per unit cm.



(a) X coordinate



(b) Y coordinate



(c) Z coordinate

Figure 5.19: Vertex distribution of selected reconstructed decay electrons in the data.

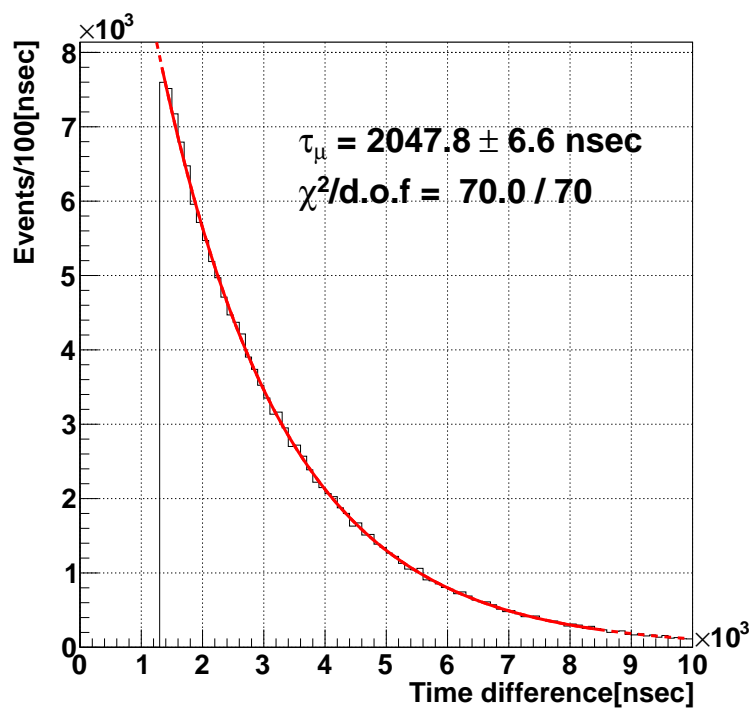


Figure 5.20: The decay curve of stopped muons observed in sample data. The fitting range is red solid line and the expected distribution after fitting the function is red dashed line.

Chapter 6

Results and discussion

6.1 Calculation of charge ratio

Positive muons are free from nuclear capture and their lifetimes are equal to τ_μ in vacuum, which corresponds to $\tau_\mu = 2.1969811 \pm 0.0000022 \mu\text{sec}$ [32]. However, a few negative muons are captured by the ^{16}O nuclei in the target, resulting in a shorter lifetime of negative muons than that in vacuum. When a negative muon is stopped in a medium, it replaces the innermost electron of the nucleus and forms a muonic atom as shown Figure 6.1.

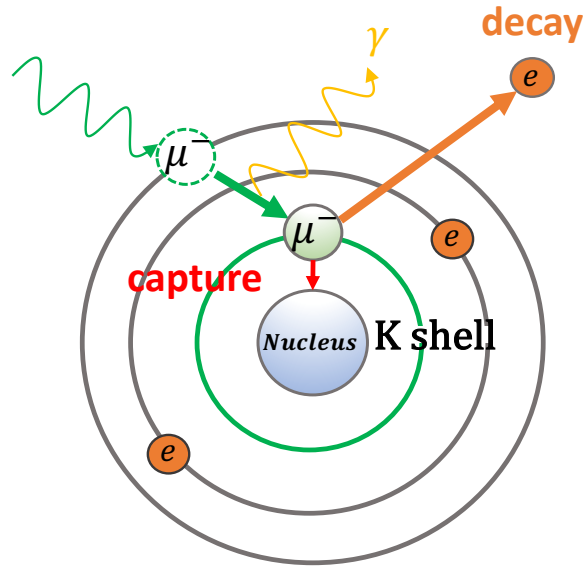


Figure 6.1: Schematic of the muonic atom. A negative muon takes an atomic orbit (K shell) and creates an excited nucleus. The negative muon follows either process, free muon decay in orbit or nuclear muon capture.

In the ground state, a negative muon follows one of two competing processes; free muon decay ($\mu^- \rightarrow e^- + \bar{\nu}_e + \nu_\mu$) or nuclear muon capture ($\mu^- + (A, Z) \rightarrow \nu_\mu + (A, Z - 1)$). The lifetime of the negative muon can be expressed as two components:

$$\tau_{\mu^-}^{-1} = \Lambda_d + \Lambda_c, \quad (6.1)$$

where Λ_d is the free decay rate, and Λ_c is the capture rate of the negative muon by a nucleus, respectively. Here, the nuclear capture rate is given as,

$$\Lambda_c = \Lambda_1 Z^4, \quad (6.2)$$

where Λ_1 is the nuclear capture rate in the hydrogen and Z is the charge of the nucleus (corresponds to the proton number). Consequently, the lifetime of the negative muon depends on the Z number and it becomes shorter in heavier nuclei ($Z \leq 100$) [34]. Measurements of the lifetimes of negative muons have been performed in various media in the previous studies [35]. The mean lifetime of negative muons in pure water is obtained as $\tau_{\mu^-} = 1.7954 \pm 0.0020 \mu\text{sec}$ [35]. The lifetime difference between the positive and negative muons allows the estimation of the ratio of the muons by measuring the time of the muon decay. In general, the number of decayed particles in time difference dt can be expressed as:

$$dN(t) = -N\lambda dt, \quad (6.3)$$

where $N(t)$ is the number of particles at a time t , λ ($= 1/\tau$) is the probability that a particle decay per unit time, and τ is the mean lifetime. The decay function of particle is given as follows by taking the integral of Eq. (6.3):

$$\begin{aligned} \int_{N_0}^N \frac{dN}{N} &= -\lambda \int_0^t dt, \\ N(t) &= N_0 \exp(-\lambda t). \end{aligned} \quad (6.4)$$

The number of decayed particles in an unit time is:

$$-\frac{dN(t)}{dt} = \frac{N_0}{\tau} \exp\left(-\frac{t}{\tau}\right), \quad (6.5)$$

which corresponds to the observed decay electron events from parent muons. Furthermore, considering the binning width Δt of the histogram, the expected events between t to $t + \Delta t$ are:

$$\begin{aligned} N(t \sim (t + \Delta t)) &= \int_t^{t+\Delta t} \left(-\frac{dN(t)}{dt}\right) dt \\ &= N_0 \left\{ 1 - \exp\left(-\frac{\Delta t}{\tau}\right) \right\} \exp\left(-\frac{t}{\tau}\right). \end{aligned} \quad (6.6)$$

Here, N_0 represents the number of particles at $t = 0$. Muons measured by the detector, consist of two components, τ_{μ^+} and τ_{μ^-} , therefore, the lifetime spectrum is fitted by the sum of two exponential functions:

$$\begin{aligned} N(t \sim (t + \Delta t)) &= N_+ \left\{ 1 - \exp\left(-\frac{\Delta t}{\tau_{\mu^+}}\right) \right\} \exp\left(-\frac{t}{\tau_{\mu^+}}\right) \\ &+ N_- \left\{ 1 - \exp\left(-\frac{\Delta t}{\tau_{\mu^-}}\right) \right\} \exp\left(-\frac{t}{\tau_{\mu^-}}\right), \end{aligned} \quad (6.7)$$

where Δt is set to be $0.1 \mu\text{sec}$ in this study, and N_+ , N_- are the total number of detected positive muons and negative muons, respectively. The number of observed negative muon events seemingly decreases by the factor of nuclear capture in the water, and this effect must

be considered. Since the water can be assumed as ^{16}O , the nuclear capture fraction for negative muons in water is $\Lambda_c = 0.184 \pm 0.001$ [35]. Considering nuclear capture effects on negative muons, the charge ratio $R(\mu^+/\mu^-)$ can be expressed by:

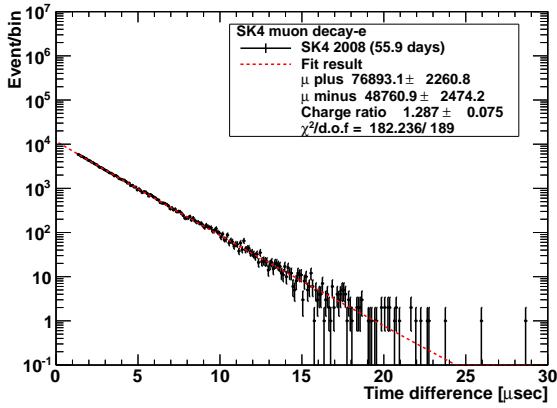
$$R(\mu^+/\mu^-) = \frac{N_+}{N_-/(1 - \Lambda_c)}. \quad (6.8)$$

6.2 Results

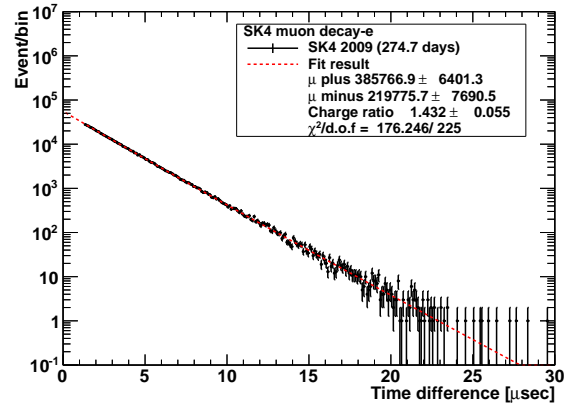
Finally, using the final samples of muons and decay electrons collected in SK-IV, the charge ratio of cosmic-ray muons was measured. Due to the small residual magnetic field in the water tank [16], the SK can not distinguish the charge of the cosmic-ray muons in principle. However, using the analysis method described in previous section, the number of positive and negative muons were obtained from the decay curve. The decay curve of stopping muons obtained from the time interval between the parent muon and delayed electron events are shown in Figure 6.2. From the fitting of the decay curve of $\mu - e$ decay events observed in the data taking period in SK-IV from 2008 to 2018, N_+ and N_- were obtained for each year, respectively. The results of N_+ , N_- and the charge ratio $R(\mu^+/\mu^-)$ calculated from Eq. (6.8) are listed in Table 6.1 with $\chi^2/d.o.f$. The fitting results of $\chi^2/d.o.f$ are also shown in Figure 6.3 along with N_+ and N_- per day. The goodness of the fitting results for each data period are distributed between 0.6 to 1.0 and no biases can be found from these results. The event rates of decay electrons per day are stable at around 1,400 events/day for the positive muon and 800 events/day for the negative muon. The yearly variation of the charge ratio in the data period of SK-IV is shown in Figure 6.4. The combined result of the charge ratio in SK-IV is obtained by taking the mean weighted value of eleven data points of the charge ratio and found to be 1.42 ± 0.02 (statistical uncertainty only). The yearly charge ratios are distributed within 10% of the mean value. The combined data points are plotted in Figure 6.4 together with the previous measurement at Kamiokande-II [10]. The total charge ratio in the SK-IV phase is consistent within the error of that in Kamiokande-II.

6.3 Discussion

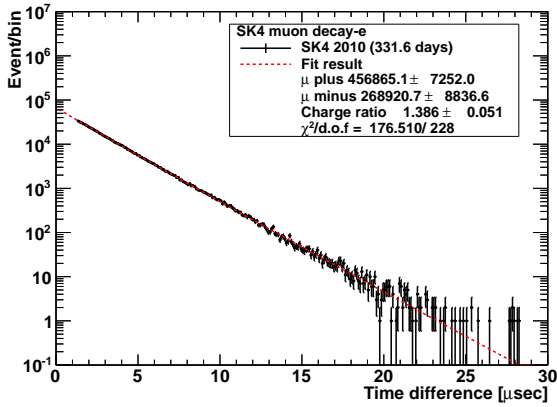
Comparing the muon charge ratio obtained in this analysis to other experimental results, the charge ratio becomes higher at around 1 TeV than those measured below 500 GeV. As explained in Chapter 1, the increase in the charge ratio in the TeV region is due to the contribution from kaon decay to muon flux. In this energy region, the possibility of kaon decay to μ^+ becomes larger than that of pion decay. Models of the muon production from secondaries in the atmosphere provide a qualitative interpretation of the enhancement of the charge ratio in the TeV region. One of the simplified models called the πK model gives the numerical values by considering several assumptions. This model only considers the contribution from both particles; pion and kaon decay and ignores the contribution from the charm particle whose effect becomes important above 10 TeV. Furthermore, the energy dependence of the charge ratio is expressed in the form of $E_\mu \cos \theta$. However, π/K production ratio is assumed to be energy independent [36]. In this model, the muon charge ratio is parameterized as a function of f_{π^+} and f_{K^+} as defined in Section 1.4 as the fraction parameter of all positive muons from π^+ and K^+ decay, respectively. The investigation of the fraction of secondaries has been performed with several underground experiments for the numerical evaluation and reported both fraction parameters as $f_{\pi^+} = 0.55$ and $f_{K^+} = 0.67$ [1], [9], [37]. The result obtained from the SK-IV data



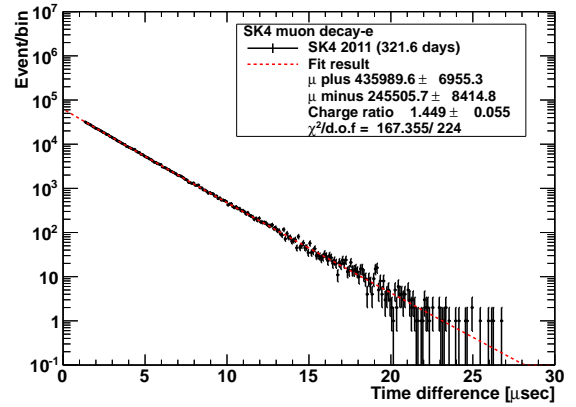
(a) Decay curve of stopped muons in 2008



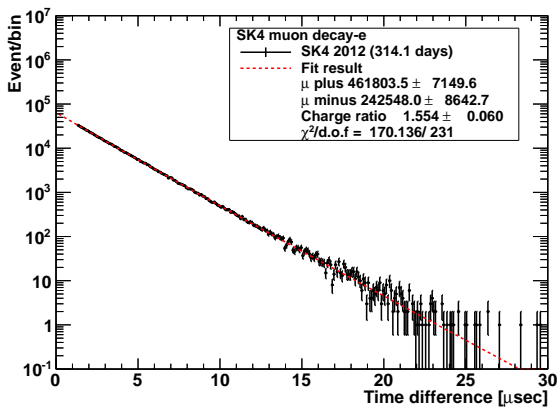
(b) Decay curve of stopped muons in 2009



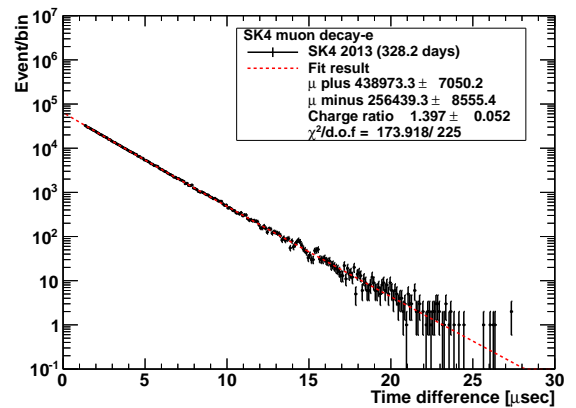
(c) Decay curve of stopped muons in 2010



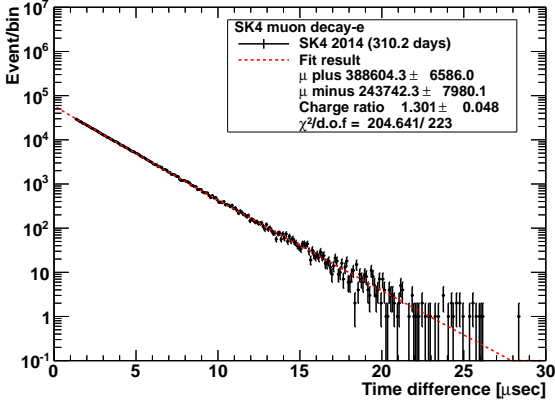
(d) Decay curve of stopped muons in 2011



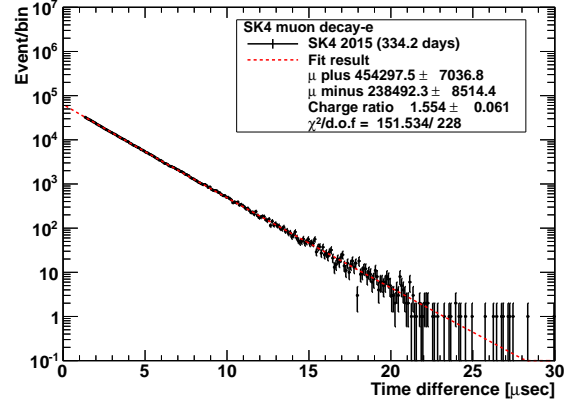
(e) Decay curve of stopped muons in 2012



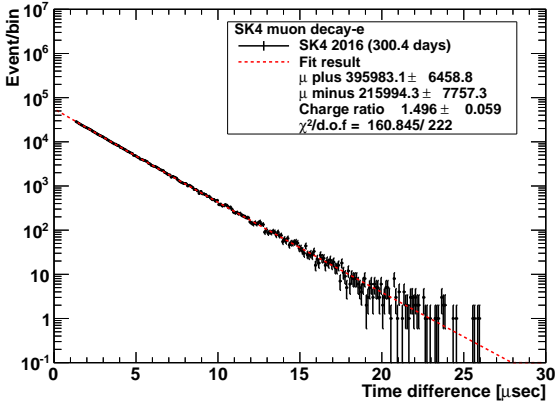
(f) Decay curve of stopped muons in 2013



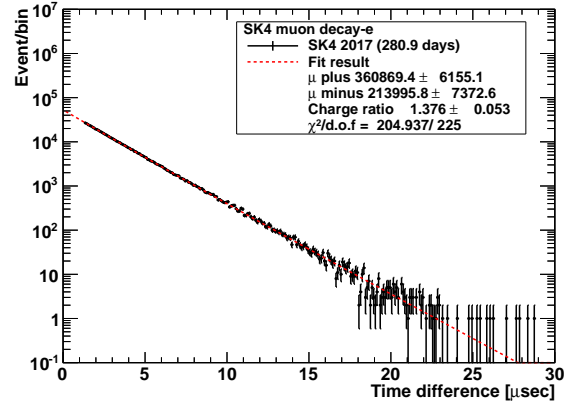
(g) Decay curve of stopped muons in 2014



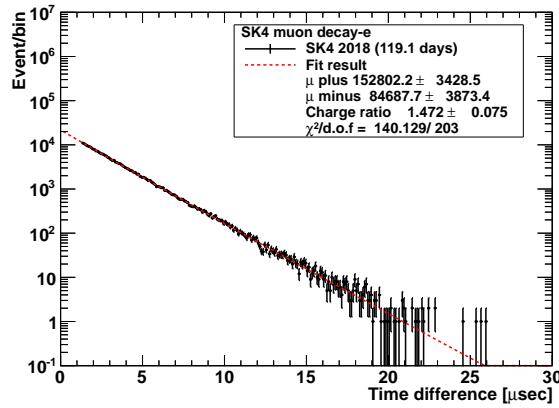
(h) Decay curve of stopped muons in 2015



(i) Decay curve of stopped muons in 2016



(j) Decay curve of stopped muons in 2017



(k) Decay curve of stopped muons in 2018

Figure 6.2: The decay curve of stopped muons observed each year from 2008 to 2018. The solid red line was obtained by fitting a function Eq. (6.5). The effective live time and fitting results (number of positive and negative muons with the charge ratio, $\chi^2/d.o.f$) are listed in the legend.

Table 6.1: The results of N_+ , N_- and the charge ratio $R(\mu^+/\mu^-)$. In this study, only statistical uncertainty is considered.

Data (Live time)	N_+	N_-	$R(\mu^+/\mu^-)$	$\chi^2/d.o.f$
2008 (55.9 days)	76893.1 ± 2260.8	48760.9 ± 2474.2	1.287 ± 0.075	182.236/189
2009 (274.7 days)	385766.9 ± 6401.3	219775.7 ± 7690.5	1.432 ± 0.055	176.246/225
2010 (331.6 days)	456865.1 ± 7252.0	268920.7 ± 8836.6	1.386 ± 0.051	176.510/228
2011 (321.6 days)	435989.6 ± 6955.3	245505.7 ± 8414.8	1.449 ± 0.055	167.355/224
2012 (314.1 days)	461803.5 ± 7149.6	242548.0 ± 8642.7	1.554 ± 0.060	170.136/231
2013 (328.2 days)	438973.3 ± 7050.2	256439.3 ± 8555.4	1.397 ± 0.052	173.918/225
2014 (310.2 days)	388604.3 ± 6586.0	243742.3 ± 7980.1	1.301 ± 0.048	204.641/223
2015 (334.2 days)	454297.5 ± 7036.8	238492.3 ± 8514.4	1.554 ± 0.061	151.534/228
2016 (300.4 days)	395983.1 ± 6458.8	215994.3 ± 7757.3	1.496 ± 0.059	160.845/222
2017 (280.9 days)	360869.4 ± 6155.1	213995.8 ± 7372.6	1.376 ± 0.053	204.937/225
2018 (119.1 days)	152802.2 ± 3428.5	84687.7 ± 3873.4	1.472 ± 0.075	140.129/203

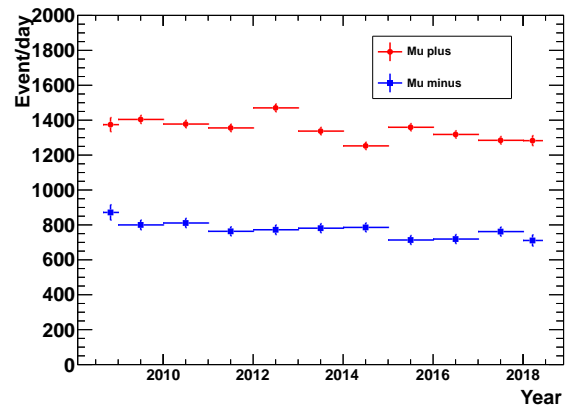
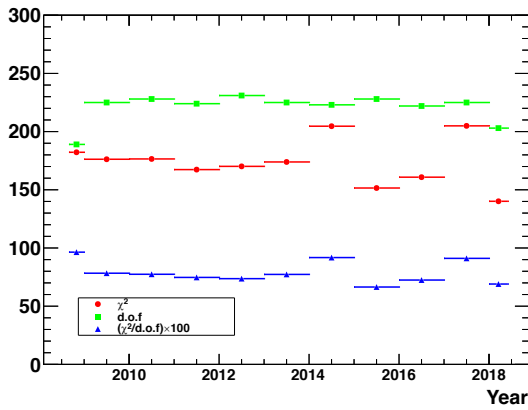


Figure 6.3: Fitting results of decay curve with χ^2 (red) probability, $d.o.f$ (green), $(\chi^2/d.o.f) \times 100$ (blue) (left) and the event rate of decay electron [event/day] (right) obtained from positive (red) and negative (blue) stopped muons in SK-IV period.

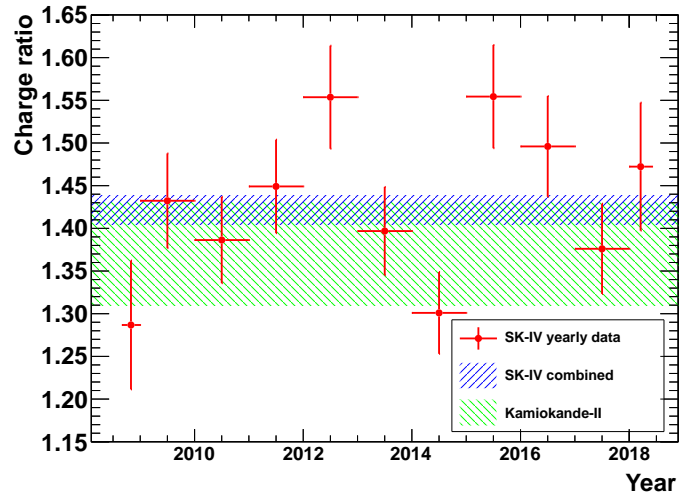


Figure 6.4: Yearly time variation of the charge ratio of 1.3 TeV cosmic-ray muons from 2008 to 2018 together with the result from the Kamiokande-II. The blue band area shows the average of muon charge ratio in SK-IV period and green band is the result from Kamiokande-II [10].

indicate that the effect of kaon products on the muon charge ratio becomes significant in a few TeV energy region and in good agreement with the miscellaneous underground experimental data.

Chapter 7

Summary

The muon charge ratio provides the information of hadronic interaction in the atmosphere and allows the precise calculation of atmospheric neutrino flux for further precise measurements of the neutrino oscillation parameters.

In this thesis, the charge ratio of positive to negative cosmic-ray muons at the energy of 1.3 TeV was measured through the analysis of the decay curve of stopping muons in the SK detector at the depth of 2,700 m.w.e. The analysis was performed using the data collected from 2008 to 2018 in the SK-IV period using large statistics, with approximately 2,970 days of live time. The data sampling of stopping muons and decay electrons was optimized by evaluating the selection criteria and comparing the distribution of the simulated data. The yearly variation of the charge ratio in the SK-IV period was calculated and the combined result of the charge ratio were obtained by taking the mean weighted value of each data. In conclusion, the charge ratio was determined as 1.42 ± 0.02 (statistical uncertainty only) with the result consistent with past underground measurements in a similar energy region. The result suggests a slight increase in a few TeV regions by comparing with other underground experiments in a diverse energy range. The increase in the charge ratio can be sufficiently interpreted by the effect of kaon production and is compatible with a simplified πK model.

Bibliography

- [1] V. Khachatryan, A. Sirunyan, A. Tumasyan, *et al.*, “Measurement of the charge ratio of atmospheric muons with the CMS detector,” *Physics Letters B*, vol. 692, no. 2, pp. 83–104, 2010, ISSN: 0370-2693. DOI: <https://doi.org/10.1016/j.physletb.2010.07.033>. [Online]. Available: <https://www.sciencedirect.com/science/article/pii/S0370269310008725>.
- [2] N. Agafonova, A. Anokhina, S. Aoki, *et al.*, “Measurement of the atmospheric muon charge ratio with the OPERA detector,” *The European Physical Journal C*, vol. 67, no. 1, pp. 25–37, 2010. DOI: [10.1140/epjc/s10052-010-1284-8](https://doi.org/10.1140/epjc/s10052-010-1284-8). [Online]. Available: <https://doi.org/10.1140/epjc/s10052-010-1284-8>.
- [3] T. Hebbeker and C. Timmermans, “A compilation of high energy atmospheric muon data at sea level,” *Astroparticle Physics*, vol. 18, no. 1, pp. 107–127, 2002, ISSN: 0927-6505. DOI: [https://doi.org/10.1016/S0927-6505\(01\)00180-3](https://doi.org/10.1016/S0927-6505(01)00180-3). [Online]. Available: <https://www.sciencedirect.com/science/article/pii/S0927650501001803>.
- [4] N. Mauri, “Experimental results on the atmospheric muon charge ratio,” in *European Physical Journal Web of Conferences*, ser. European Physical Journal Web of Conferences, vol. 121, Jul. 2016, 03007, p. 03 007. DOI: [10.1051/epjconf/201612103007](https://doi.org/10.1051/epjconf/201612103007).
- [5] T. K. Gaisser, R. Engel, and E. Resconi, *Cosmic Rays and Particle Physics*. 2016.
- [6] W. R. Frazer, C. H. Poon, D. Silverman, and H. J. Yesian, “Limiting fragmentation and the charge ratio of cosmic-ray muons,” *Phys. Rev. D*, vol. 5, pp. 1653–1657, 7 Apr. 1972. DOI: [10.1103/PhysRevD.5.1653](https://doi.org/10.1103/PhysRevD.5.1653). [Online]. Available: <https://link.aps.org/doi/10.1103/PhysRevD.5.1653>.
- [7] P. Achard, O. Adriani, M. Aguilar-Benitez, *et al.*, “Measurement of the atmospheric muon spectrum from 20 to 3000 gev,” *Physics Letters B*, vol. 598, no. 1, pp. 15–32, 2004, ISSN: 0370-2693. DOI: <https://doi.org/10.1016/j.physletb.2004.08.003>. [Online]. Available: <https://www.sciencedirect.com/science/article/pii/S0370269304011438>.
- [8] G. K. Ashley, J. W. Keuffel, and M. O. Larson, “Charge ratio of ultra-high-energy cosmic-ray muons,” *Phys. Rev. D*, vol. 12, pp. 20–35, 1 Jul. 1975. DOI: [10.1103/PhysRevD.12.20](https://doi.org/10.1103/PhysRevD.12.20). [Online]. Available: <https://link.aps.org/doi/10.1103/PhysRevD.12.20>.
- [9] P. Adamson, C. Andreopoulos, K. E. Arms, *et al.*, “Measurement of the atmospheric muon charge ratio at tev energies with the MINOS detector,” *Phys. Rev. D*, vol. 76, p. 052 003, 5 Sep. 2007. DOI: [10.1103/PhysRevD.76.052003](https://doi.org/10.1103/PhysRevD.76.052003). [Online]. Available: <https://link.aps.org/doi/10.1103/PhysRevD.76.052003>.
- [10] M. Yamada, K. Miyano, H. Miyata, *et al.*, “Measurements of the charge ratio and polarization of 1.2-tev/c cosmic-ray muons with the Kamiokande II detector,” *Phys. Rev. D*, vol. 44, pp. 617–621, 3 Aug. 1991. DOI: [10.1103/PhysRevD.44.617](https://doi.org/10.1103/PhysRevD.44.617). [Online]. Available: <https://link.aps.org/doi/10.1103/PhysRevD.44.617>.

- [11] S. Fukuda, Y. Fukuda, T. Hayakawa, *et al.*, “The Super-Kamiokande detector,” *Nuclear Instruments and Methods in Physics Research Section A: Accelerators, Spectrometers, Detectors and Associated Equipment*, vol. 501, no. 2, pp. 418–462, 2003, ISSN: 0168-9002. DOI: [https://doi.org/10.1016/S0168-9002\(03\)00425-X](https://doi.org/10.1016/S0168-9002(03)00425-X). [Online]. Available: <https://www.sciencedirect.com/science/article/pii/S016890020300425X>.
- [12] S. Yamada, K. Awai, Y. Hayato, *et al.*, “Commissioning of the new electronics and on-line system for the super-kamiokande experiment,” in *2009 16th IEEE-NPSS Real Time Conference*, 2009, pp. 201–205. DOI: [10.1109/RTC.2009.5321856](https://doi.org/10.1109/RTC.2009.5321856).
- [13] K. Abe, C. Bronner, Y. Hayato, *et al.*, “First gadolinium loading to super-kamiokande,” *Nuclear Instruments and Methods in Physics Research Section A: Accelerators, Spectrometers, Detectors and Associated Equipment*, vol. 1027, p. 166 248, 2022, ISSN: 0168-9002. DOI: <https://doi.org/10.1016/j.nima.2021.166248>. [Online]. Available: <https://www.sciencedirect.com/science/article/pii/S0168900221010883>.
- [14] Hamamatsu Photonics K.K., *PHOTOMULTIPLIER TUBES -Basics and Applications-*, Fourth edition. Hamamatsu Photonics K.K. Electron Tube Divison, Apr. 2017.
- [15] Y. Nakano, “ ^8B solar neutrino spectrum measurement using Super-Kamiokande IV,” Ph.D. dissertation, University of Tokyo, 2016.
- [16] K. Abe *et al.*, “Calibration of the Super-Kamiokande Detector,” *Nucl. Instrum. Meth. A*, vol. 737, pp. 253–272, 2014. DOI: [10.1016/j.nima.2013.11.081](https://doi.org/10.1016/j.nima.2013.11.081). arXiv: [1307.0162](https://arxiv.org/abs/1307.0162) [physics.ins-det].
- [17] Y. Nakano, T. Hokama, M. Matsubara, *et al.*, “Measurement of the radon concentration in purified water in the super-kamiokande iv detector,” *Nuclear Instruments and Methods in Physics Research Section A: Accelerators, Spectrometers, Detectors and Associated Equipment*, vol. 977, p. 164 297, 2020, ISSN: 0168-9002. DOI: <https://doi.org/10.1016/j.nima.2020.164297>. [Online]. Available: <https://www.sciencedirect.com/science/article/pii/S0168900220306938>.
- [18] Y. Nakano, H. Sekiya, S. Tasaka, *et al.*, “Measurement of radon concentration in super-kamiokande’s buffer gas,” *Nuclear Instruments and Methods in Physics Research Section A: Accelerators, Spectrometers, Detectors and Associated Equipment*, vol. 867, pp. 108–114, 2017, ISSN: 0168-9002. DOI: <https://doi.org/10.1016/j.nima.2017.04.037>. [Online]. Available: <https://www.sciencedirect.com/science/article/pii/S0168900217305004>.
- [19] H. Nishino, K. Awai, Y. Hayato, *et al.*, “High-speed charge-to-time converter ASIC for the Super-Kamiokande detector,” *Nuclear Instruments and Methods in Physics Research Section A: Accelerators, Spectrometers, Detectors and Associated Equipment*, vol. 610, no. 3, pp. 710–717, 2009, ISSN: 0168-9002. DOI: <https://doi.org/10.1016/j.nima.2009.09.026>. [Online]. Available: <https://www.sciencedirect.com/science/article/pii/S0168900209017495>.
- [20] Z. Conner, “A study of solar neutrinos using the Super-Kamiokande detector,” Ph.D. dissertation, University of Maryland, 1997.
- [21] S. Desai, “High energy neutrino astrophysics with Super-Kamiokande,” Ph.D. dissertation, Boston University, 2004.
- [22] M. Smy, Ed., *Proc. of the 30th ICRC*, vol. 5, 1279, 2007.
- [23] Y. Ashida, “Measurement of neutrino and antineutrino neutral-current quasielastic-like interactions and applications to supernova relic neutrino searches,” Ph.D. dissertation, Kyoto University, 2020.

- [24] M. Shinoki, M.S. thesis, Tokyo University of Science, 2021.
- [25] R. Brun, F. Bruyant, F. Carminati, *et al.*, “GEANT Detector Description and Simulation Tool,” Oct. 1994. DOI: [10.17181/CERN.MUHF.DMJ1](https://doi.org/10.17181/CERN.MUHF.DMJ1).
- [26] A. Tang, G. Horton-Smith, V. A. Kudryavtsev, and A. Tonazzo, “Muon simulations for super-kamiokande, kamland, and chooz,” *Phys. Rev. D*, vol. 74, p. 053007, 5 Sep. 2006. DOI: [10.1103/PhysRevD.74.053007](https://doi.org/10.1103/PhysRevD.74.053007). [Online]. Available: <https://link.aps.org/doi/10.1103/PhysRevD.74.053007>.
- [27] S. Abe, S. Enomoto, K. Furuno, *et al.*, “Production of radioactive isotopes through cosmic muon spallation in kamland,” *Phys. Rev. C*, vol. 81, p. 025807, 2 Feb. 2010. DOI: [10.1103/PhysRevC.81.025807](https://doi.org/10.1103/PhysRevC.81.025807). [Online]. Available: <https://link.aps.org/doi/10.1103/PhysRevC.81.025807>.
- [28] P. Antonioli, C. Ghetti, E. Korolkova, V. Kudryavtsev, and G. Sartorelli, “A three-dimensional code for muon propagation through the rock: Music,” *Astroparticle Physics*, vol. 7, no. 4, pp. 357–368, 1997, ISSN: 0927-6505. DOI: [https://doi.org/10.1016/S0927-6505\(97\)00035-2](https://doi.org/10.1016/S0927-6505(97)00035-2). [Online]. Available: <https://www.sciencedirect.com/science/article/pii/S0927650597000352>.
- [29] Geographical Survey Institute of Japan, Digital Map 50 m Grid (Elevation), 1997.
- [30] A. Coffani, “FLUKA simulation for spallation background,” Super-Kamiokande Collaboration Meeting, Nov. 2019.
- [31] T. Shiozawa and Y. Nakano, “Seasonal modulation of cosmic muon flux,” Super-Kamiokande Collaboration Meeting, Nov. 2019.
- [32] P. D. Group, P. A. Zyla, R. M. Barnett, *et al.*, “Review of Particle Physics,” *Progress of Theoretical and Experimental Physics*, vol. 2020, no. 8, Aug. 2020, 083C01, ISSN: 2050-3911. DOI: [10.1093/ptep/ptaa104](https://doi.org/10.1093/ptep/ptaa104). eprint: <https://academic.oup.com/ptep/article-pdf/2020/8/083C01/34673722/ptaa104.pdf>. [Online]. Available: <https://doi.org/10.1093/ptep/ptaa104>.
- [33] Y. Fukuda, K. Ishihara, Y. Itow, *et al.*, “Neutrino-induced upward stopping muons in super-kamiokande,” *Physics Letters B*, vol. 467, no. 3, pp. 185–193, 1999, ISSN: 0370-2693. DOI: [https://doi.org/10.1016/S0370-2693\(99\)01188-0](https://doi.org/10.1016/S0370-2693(99)01188-0). [Online]. Available: <https://www.sciencedirect.com/science/article/pii/S0370269399011880>.
- [34] K. Nagamine, *Introductory Muon Science*. Cambridge University Press, 2003. DOI: [10.1017/CBO9780511470776](https://doi.org/10.1017/CBO9780511470776).
- [35] T. Suzuki, D. F. Measday, and J. P. Roalsvig, “Total nuclear capture rates for negative muons,” *Phys. Rev. C*, vol. 35, pp. 2212–2224, 6 Jun. 1987. DOI: [10.1103/PhysRevC.35.2212](https://doi.org/10.1103/PhysRevC.35.2212). [Online]. Available: <https://link.aps.org/doi/10.1103/PhysRevC.35.2212>.
- [36] P. Schreiner, J. Reichenbacher, and M. Goodman, “Interpretation of the underground muon charge ratio,” *Astroparticle Physics*, vol. 32, no. 1, pp. 61–71, 2009, ISSN: 0927-6505. DOI: <https://doi.org/10.1016/j.astropartphys.2009.06.002>. [Online]. Available: <https://www.sciencedirect.com/science/article/pii/S0927650509000875>.
- [37] T. K. Gaisser, “Spectrum of cosmic-ray nucleons, kaon production, and the atmospheric muon charge ratio,” *Astroparticle Physics*, vol. 35, no. 12, pp. 801–806, 2012, ISSN: 0927-6505. DOI: <https://doi.org/10.1016/j.astropartphys.2012.02.010>. [Online]. Available: <https://www.sciencedirect.com/science/article/pii/S0927650512000497>.